Development of simulations and proportional chamber detectors to measure open charm and charmonium particles in antiproton-proton annihilation

Inaugural-Dissertation
zur Erlangung des Doktorgrades der Naturwissenschaften
der Justus Liebig Universität Giessen
Fachbereich 07 (Mathematik und Informatik, Physik, Geographie)

vorgelegt von

ANDREY SOKOLOV

aus Novosibirsk (Russland)

II. Physikalisches Institut
der Justus Liebig Universität Giessen

July 2005

Dekan:	Prof. Dr. V. Metag
I. Berichterstatter:	Prof. PhD. J. Ritman
II. Berichterstatter:	Prof. Dr. Dr. W. Cassing
Tag der mündlichen Prüfung:	?????

Contents

Chapter 1

Introduction

Although Quantum Chromo Dynamics (QCD) is generally accepted to be the correct underlying theory of the strong interaction, our knowledge of its behavior at large distances is still rather primitive. We expect to learn a lot from spectroscopy experiments, which has been a prime tool for physics in the last century, both in the dynamics governing the interaction of fundamental particles and in the existence of new forms of matter. The latter could consist of gluonic degrees of freedom like glueballs and hybrids, previously undiscovered charmonium states, the extension of the nuclear chart with the strangeness dimension or particles produced inside nuclear matter. Until we can predict, confirm and explain those physical states of the theory we can hardly claim that we understand the strong interaction. Such an understanding might have further reaching implications in particle physics. In strong-interaction studies based on QCD we have the ideal laboratory to test our understanding of theory against experimental results.

The $\overline{\mathsf{P}}$ANDA collaboration proposes to build a state-of-the-art general-purpose detector for strong interaction studies at the high-energy storage ring HESR at the international FAIR facility. The detector is designed to take advantage of the extraordinary physics potential which becomes available utilizing high intensity, phase space cooled antiproton beams.

This dissertation describes the results of the work devoted the simulation and the designing of the tracking system for the $\overline{\mathsf{P}}$ANDA detector, together with the study of the physics performance of the whole system.

In this chapter, the main aspects of the $\overline{\mathsf{P}}$ANDA physics program are presented.

1.1 Physics Motivation

The strong force governs the microscopic structure of matter. It dominates the interaction between the nucleons, i.e. the protons and neutrons within the atomic nucleus, and it is the key force that determines the interaction between the quarks within the nucleon and within other hadrons (strongly interacting particles). Achieving a fully quantitative understanding of matter at this level is one of the most challenging and fascinating areas of modern physics. During the last two decades hadronic physics has moved from phe-

nomenological to fundamental understanding. The theory of Quantum Chromodynamics (QCD) is regarded as the basic theory of the strong interaction. While being elegant and deceptively simple, the theory generates a most remarkable richness and complexity of phenomena. The possible forms of matter range from the spectrum of strongly interacting hadrons and nuclear species to compact stars of extreme density and to the quark-gluon plasma, a state of matter in the early universe and, possibly, in the interior of very heavy stars.

The fundamental building blocks of QCD are the quarks which interact with each other by exchanging particles, the gluons. QCD is simple and well understood at short-distance scales, much shorter than the size of a nucleon ($< 10^{-15}$ m). In this regime, the basic quark-gluon interaction is sufficiently weak. Here, perturbation theory can be applied, a calculation technique of high predictive power yielding accurate results when the coupling strength is small. In fact, many processes at high energies can quantitatively be described by perturbative QCD within this approximation.

The perturbative approach fails when the distance among quarks becomes comparable to the size of the nucleon, the characteristic dimension of our microscopic world. Under these conditions, the force among the quarks becomes so strong that they cannot be further separated, in contrast to the electromagnetic and gravitational forces which fall off with increasing distance. This unusual behavior is related to the self-interaction of gluons: gluons do not only interact with quarks but also with each other, leading to the formation of gluonic flux tubes connecting the quarks. As a consequence, quarks have never been observed as free particles and are confined within hadrons, complex particles made of 3 quarks (baryons) or a quark-antiquark pair (mesons). Baryons and mesons are the relevant degrees of freedom in our environment. An important consequence of the gluon self-interaction and – if found – a strong proof of our understanding of hadronic matter is the predicted existence of hadronic systems consisting only of gluons (glueballs) or bound systems of quark-antiquark pairs and gluons (hybrids).

In the evolution of the universe, some microseconds after the big bang, a coalescence of quarks to hadrons occurred associated with the generation of mass. The elementary light quarks, the up and down quarks, that make up the nucleon have very small masses amounting to only about 1% percent of the total mass of the nucleon. Most of the nucleon mass, and of the visible universe stems from the QCD interaction. The generation of mass is associated with the confinement of quarks and the spontaneous breaking of chiral symmetry, one of the fundamental symmetries of QCD in the limit of massless quarks. On the other hand, the heavy quark limit involves different, heavy quark symmetries and the correspondent spectroscopy is characterized by the almost static behavior of the very massive bottom quark, which is almost five times heavier than the nucleon. The top quark is too short lived to form any bound state. The masses of strange (s) and charmed (c) quarks, $m_s \sim 0.1 \times m_N$ and $m_c \sim 1.4 \times m_N$, are intermediate between the chiral and heavy quark limits. That makes the physics of strange and charmed quarks so interesting, since they interpolate between the limiting scales of QCD. In particular, the very important domain of charmed quarks with its connection to gluon dynamics and the confinement problem is still not understood.

In that sense, the study of charmonium, a system consisting of a charm and anticharm

quark, is essential to the understanding of the strong nuclear force and the Standard Model.

The phenomena of the confinement of quarks, the existence of glueballs and hybrids, and the origin of the mass of strongly interacting, composite systems related to confinement and the breaking of chiral symmetry are long-standing puzzles and represent the intellectual challenge in our attempt to understand the nature of the strong interaction and of hadronic matter.

1.2 Research Program

Antiproton beams of unprecedented intensity and quality in the energy range of 1 GeV to 15 GeV, as provided by the new FAIR facility together with $\overline{\text{P}}$ANDA, will be an excellent tool to address the fundamental questions sketched above. Antiproton beams in this energy regime, stored in the High-Energy Storage Ring (HESR) for in-ring experiments, will provide access to the heavier strange and charm quarks and to copious production of gluons. As illustrated in Fig. 1.1, the physics program offers a broad range of investigations that extend from the study of Quantum Chromodynamics to the test of fundamental symmetries. The key components of the antiproton program are summarized as follows:

The determination of the interaction potential through precision spectroscopy has been a successful tool at all levels of the structural hierarchy of matter, as for example in atoms and molecules. The charm quark is sufficiently heavy to lend itself to non-relativistic perturbative treatment far more reliably than the light up, down, and strange quarks. Thus, an optimal testing ground for a quantitative understanding of confinement is provided by charmonium spectroscopy, i.e. the spectroscopy of mesons built of charmed quark-antiquark pairs ($c\bar{c}$). The proposed program, using resonant antiproton-proton annihilation, is a quantitative and qualitative extension of successful experiments performed recently at the antiproton accumulator at FNAL, USA. However, the studies (which ended in 2 000) were limited in scope by lower antiproton energies (< 9 GeV), lower luminosities ($\leq 2.5 \cdot 10^{31}\text{cm}^{-2}s^{-1}$) and a detector only capable of detecting electromagnetic reaction products. At FAIR, advanced antiproton cooling techniques will enable high energy resolution and a more versatile detector setup will be employed allowing for the first time a measurement of both electromagnetic and hadronic decays with high precision. The goal is to achieve comprehensive precision spectroscopy of the charmonium system for a detailed study, particularly of the confinement part of the QCD potential. This in turn will help to understand the key aspects of gluon dynamics which are being investigated and quantitatively predicted in the framework of Lattice QCD.

Recent experiments at LEAR/CERN have demonstrated that particles with gluonic degrees of freedom are produced copiously in proton-antiproton annihilation in the light quark sector. A central part of the antiproton program is the first search for gluonic excitations, glueball and hybrids, in the charmonium mass range where they are expected to be less mixed with the multitude of normal mesons. The unambiguous determination of the gluonic modes would establish an important missing link in the confinement problem of hadrons.

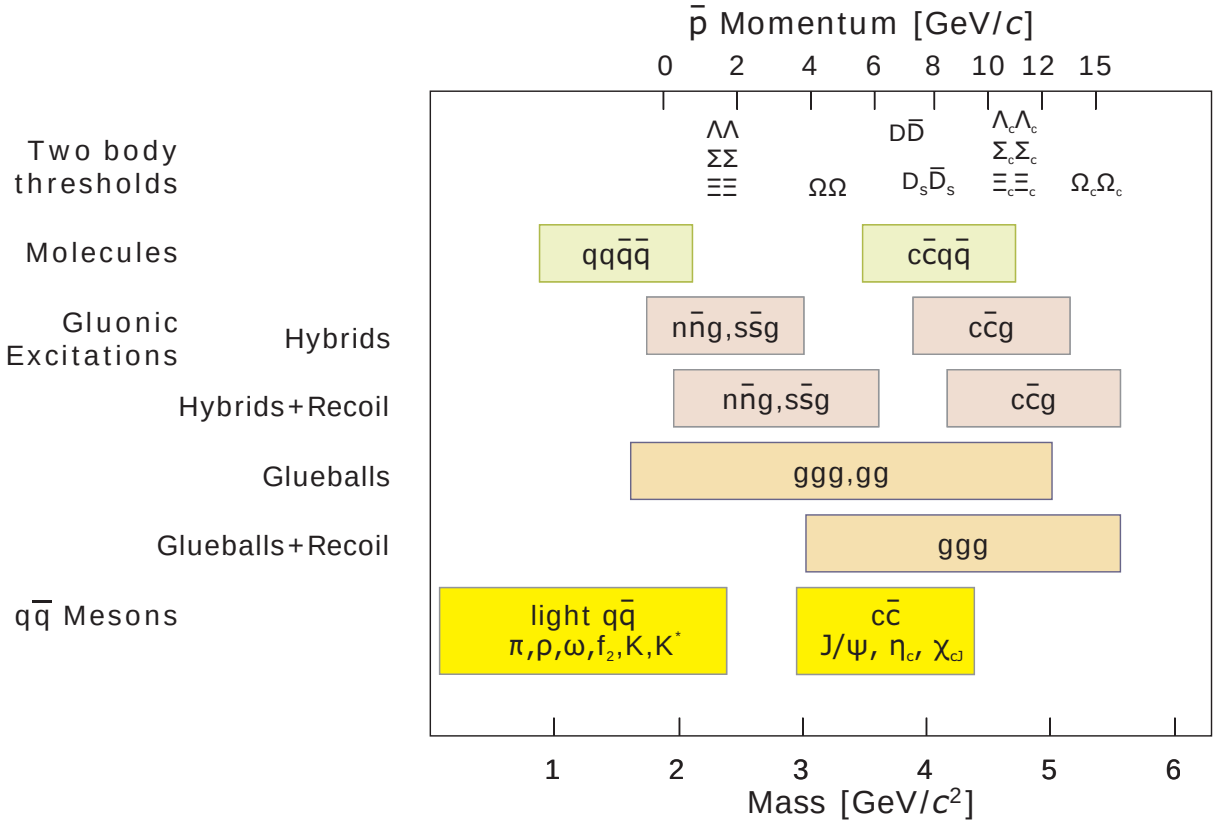

Figure 1.1: Mass range of hadrons accessible at the HESR with antiproton beams. The figure indicates the antiproton momenta required for charmonium spectroscopy, the search for charmed hybrids and glueballs, the production of D meson pairs and the production of Σ baryon pairs for hypernuclear studies. The energy range covered by the former Low Energy Antiproton Ring (LEAR) at CERN is indicated by the arrow.

GSI has an active ongoing program on the modification of the properties (masses, widths, *etc.*) of light mesons (pions and kaons) by the nuclear medium and the relation to the partial restoration of chiral symmetry. The proposed experimental program at the HESR will address the open problem of interactions and in-medium modifications of hadrons with charm quarks in nuclei. On the one hand, this is an extension of the present GSI research program. On the other hand, the program will provide the first insight into the gluonic charmonium-nucleon and charmonium-nucleus interaction. A quantitative knowledge of charmonium-nucleon cross sections is considered to be of crucial importance in the identification of the formation of the quark-gluon plasma in ultra-relativistic heavy-ion collisions.

A new and largely unexplored dimension in the chart of nuclides is introduced by replacing an up or down quark by a strange quark in a nucleon bound in a nucleus, leading to the formation of a hypernucleus. Here, the strangeness quantum number is introduced into the nucleus. Antiproton beams at the proposed facility will allow efficient production of hypernuclei with more than one strange hadron. The program opens new perspectives for nuclear structure studies. The nucleon with the strange quark (hyperon) is not restricted

in the population of nuclear states as neutrons and protons are. These exotic nuclei offer a variety of new and exciting perspectives in nuclear spectroscopy and for studying the forces among hyperons and nucleons.

One of the most important symmetries of physics is $\mathcal{CP}$ symmetry (charge conjugation $\mathcal{C}$ times spatial parity $\mathcal{P}$). $\mathcal{CP}$ symmetry implies that the laws of physics apply to a system after the combined action of exchanging particles by their antiparticles and by reflection of the system in a spatial mirror. However, if $\mathcal{CP}$ symmetry was perfectly obeyed, none of the matter in the universe, neither stars nor human beings, would exist since matter and antimatter would have annihilated each other. The observed dominance of matter in the universe may be attributed to $\mathcal{CP}$ violation, an effect directly observed in the decay of neutral kaons and, very recently, in B mesons. $\mathcal{CP}$ violation can be studied in the charm meson sector and in hyperon decays, with the HESR storage ring running at full luminosity. An observation of significant $\mathcal{CP}$ violation would indicate physics beyond the Standard Model.

Two of the research areas with antiprotons, the in-medium properties of charmed hadrons and the structure of atomic nuclei with one or more strange hadrons, are examples of the close intellectual connection between the physics with antiprotons and two other major thrusts of the current proposal, relativistic nucleus-nucleus collisions and nuclear structure physics with radioactive beams. They contribute in a synergetic way to the broader goal of a deeper understanding of the structure of hadronic matter in all its forms. Finally, the close connection between the various components of the present proposal is evident in the pursuit of symmetry tests and symmetry breaking effects, which are the key for our understanding of how the world is built from the fundamental building blocks.

Chapter 2

Physics Motivation

2.1 Overview

Experimentally, studies of hadron structure can be performed with different probes such as electron, pion, kaon, proton or antiproton beams, each of which have its specific advantages. As it already have been mentioned in previous chapter Sec. 1.2, particles with gluonic degrees of freedom as well as particle-antiparticle pairs are copiously produced in antiproton-proton annihilations, allowing spectroscopic studies with unprecedented statistics and precision. Therefore, antiprotons of 1–15 GeV/c will be an excellent tool to address the all mentioned problems.

Another important feature of the $\overline{\mathsf{P}}$ANDA detector is that for a specific antiproton momentum and target selection, different physics aspects can be studied simultaneously.

2.2 Charmonium

The fundamental understanding of strong interactions in terms of QCD was greatly stimulated by the discovery of the J/ψ in 1974. This and other systems of a charm and anti-charm quark (charmonium) turned out to be a powerful tool in the understanding of the strong interaction. They are the results of $c\overline{c}$ spectroscopy which help tuning potential models of mesons. On Fig. 2.1 the family of particles known as charmonium is shown.

This is the place where the gluon condensate, closely related to the charmonium masses, is determined. The gluon condensate together with the $q\overline{q}$ condensate represent the energy density of the QCD vacuum. The charmonium system offers unique advantages for understanding quarkonia since the low density of states and their narrowness reduces mixing among them while below the corresponding open-charm thresholds.

The best understanding has been achieved for the ψ states. These can be formed directly at electron-positron colliders. With an antiproton beam charmonium states of all quantum numbers could be formed directly and the precision of the mass and width measurement depends on the beam quality only. In this case, the detector resolution is less important and the detector response is optimized for an efficient background rejection. Important

data on the excited non-ψ states, the D-wave states of charmonium, will be extremely helpful to further develop theoretical understanding.

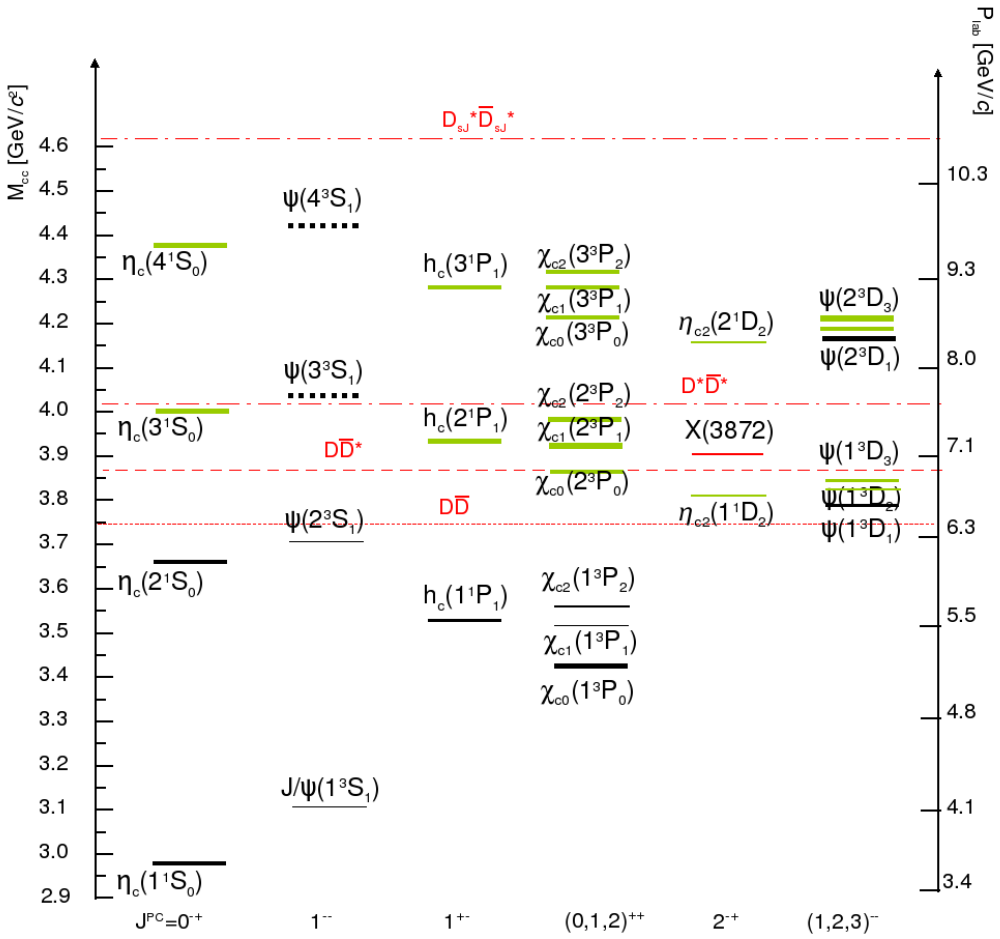

Figure 2.1: Charmonium spectrum

2.2.1 Narrow Charmonium

The comparison of the hadronic decays of the J/ψ and the ψ' [1] shows that radial excitations of charmonium are far from being simple recursions of the ground states. Therefore, it is a necessity to identify and study the first radial excitation of the charmonium ground state η_c'. It was discovered by the Belle-Experiment in hadronic B decays [2] and was confirmed by CLEO and BaBar [3, 4] in $\gamma\gamma$-collisions. Its properties are incompatible with earlier findings by Crystal Ball [5] and is only marginally consistent with most model calculations. The accuracy for the width ($\Gamma = (19 \pm 10)\,\mathrm{MeV}/c^2$) is only 50 %. In contrast to the limited statistics and the systematic limitations of e^+e^- machines, including the measurements at the B-factories, a $\overline{\mathrm{p}}\mathrm{p}$ scan will finally settle these questions, also for the ground state of charmonium, the η_c. Here, five precise measurements of the η_c properties were performed in the past two years which disagree strongly among each other [6, 7, 8].

The precision of the measurements will take advantage of the high yield of charmonium production in $\overline{\mathrm{p}}\mathrm{p}$ annihilations (e.g. BR($\overline{\mathrm{p}}\mathrm{p} \rightarrow \eta_c$)= $(1.2\pm0.4)\cdot10^{-3}$). By detecting hadronic final states ($KK\pi\pi$, $4K$, 4π, $K\overline{K}\pi$, $\eta\pi\pi$, ...) with branching fractions two orders of magnitude higher than in the $\gamma\gamma$ decay mode used so far, high-statistics samples can easily be collected.

The singlet-P resonance of charmonium, h_c, is of extreme importance in determining the spin dependent components of the $q\overline{q}$ confinement potential[9]. The h_c was first observed and positively identified by E760 in the process $\overline{\mathrm{p}}\mathrm{p} \rightarrow h_c \rightarrow J/\psi\pi^0$ [10]. The value of the mass measured by E760 was $M(h_c) = (3526.2\pm0.3)\,\mathrm{MeV}/c^2$ whereas, due to the limited statistics, only an upper value for the width at 1.1 MeV could be set. The h_c has subsequently been observed by the E835 collaboration in the process $\overline{\mathrm{p}}\mathrm{p} \rightarrow h_c \rightarrow \eta_c\gamma \rightarrow \gamma\gamma\gamma$ [11] and by the CLEO collaboration in the decay mode $h_c \rightarrow \eta_c\gamma$, with the η_c decaying to hadrons [12]. The mass values of E835 and CLEO agree with each other and with the E760 result. It should be pointed out that due to the narrow width ($\leq$1 MeV/c^2) and expected low yields, only a $\overline{\mathrm{p}}\mathrm{p}$ formation experiment like $\overline{\mathrm{P}}$ANDA will be able to measure the h_c width and to carry out a systematic study of its decay modes. The proposed experiment could provide a substantial improvement of the determination of this state and is an important part of the charmonium program.

Many other aspects are worth measuring, like the radiative de-excitation of the χ_{cJ} states (^3P_J). The decays are dominated by the dipole term E1. Higher multipoles arise in the relativistic treatment of the interaction between the electromagnetic field and the quarkonium system, and can be studied by measuring the angular distributions of both χ_{c1} and χ_{c2}. A discrepancy with theory has been observed by the Fermilab experiments E760 and E835 [13, 14] at the 2.5 σ level. Further high-statistics measurements are needed to increase the significance of the result.

2.2.2 Charmonium above Open Charm Threshold

	Mass [MeV/c^2]		Width [MeV/c^2]	
	predicted	measured	predicted	measured
$\psi(1D)$		3770	43	23.6±2.7
$\psi(3S)$		4040	74	52±10
$\psi(2D)$		4159	74	78±20
$\psi(4S)$		4415	78	43±14
$\eta_c(3S)$	$\approx$4070		67	
$\chi_{c0}(2P)$	$\approx$3870		29	
$\psi_3(1D)$	$\approx$3800		0.6	
$\chi_{c4}(1F)$	$\approx$4100		9.0	
$h_{c3}(1F)$	$\approx$4030		64	

Table 2.1: Predictions for narrow charmonia ($\Gamma < 70\,\mathrm{MeV}/c^2$) above the open charm threshold from potential and $^3P_0$ models. Details can be found in [15]. Measured values are taken from PDG [16].

Above the $D\overline{D}$ breakup threshold at $3.73\,\mathrm{GeV}/c^2$ the charmonium spectrum is poorly known since e^+e^- experiments have only measured $R = \sigma(e^+e^- \rightarrow hadrons)/\sigma(e^+e^- \rightarrow \mu^+\mu^-)$ in large energy steps. Here, rather washed-out structures were observed. The latest, much more accurate measurements by BES [17] do not confirm the sharp states reported by [18]. It is an open question whether the higher vector states at 4040, 4160, and $4415\,\mathrm{MeV}/c^2$ are realistic.

Several theories exist explaining the relative narrowness of the $\psi(4040)$ state. It can be a $\mathrm{D^*\overline{D^*}}$ molecule [19], [20]. According other idea [21] the $\psi(4040)$ and $\psi(4160)$ are strong mixtures of ground state hybrid charmonium at $\sim 4.1\mathrm{GeV}/c^2$ and $\psi(3S)$ of conventional charmonium. Both theories predict different decay patterns for both states.

It is of critical importance to investigate this mass region in small energy steps. E760/E835 were not able to study any physics above the $D\overline{D}$ threshold because of their detector limitation.

Yet, this is the region in which narrow ${}^1D_2$, ${}^3D_2$ states (which are narrow because they cannot decay to $D\overline{D}$) and the first radial excitation of the h_c and the χ_{cJ} are expected to exist. First evidence for such a state comes from the Belle collaboration which in 2003 reported the discovery of a new, narrow resonance in the decay mode $J/\psi\pi^+\pi^-$ with a mass of $3872.0\,\mathrm{MeV}/c^2$ [22]. This new state, called X(3872), has subsequently been observed by CDF [23], DØ [24] and BaBar [25]. The mass measurements by the four experiments are in very good agreement but the mass value does not fit in the current "funnel-shape" potential model, which predicts the splittings of the χ_{cJ} states very well. Therefore alternative interpretations are needed. Some authors [26, 27] suggest 1^3D_3, 1^3D_2 and 2^1P_1 as possible assignments for this state. Another explanations can be either charmonium hybrid state [28] or a $D^0\overline{D^{*0}}$ molecule [29, 30]. A precision measurement of masses, widths, decay modes and branching ratios of all 2^1P, 1^1D and 1^3D states is mandatory in order to distinguish between various models.

Apart from the unexpected discovery of the $X(3872)$ there are numerous other narrow charmonium states expected above the open charm threshold. The narrowness usually arises from forbidden decay channels and/or nodes in the wave functions inhibiting the day. A list of narrow charmonium is provided in Table 2.1. The calculation is based on a potential ansatz with Coulomb, linear confinement, smeared hyperfine and spin-orbit terms

$$\begin{aligned} V_0^{(cc)}(r) &= -\frac{4}{3}\frac{\alpha_s}{r} + br + \frac{32\pi}{9m^2}\alpha_s\delta_\sigma(r)\overrightarrow{S_c}\cdot\overrightarrow{S_{\overline{c}}} \\ &+ \frac{1}{m_c^2}\left[\frac{2\alpha_s}{r^3} + \frac{b}{2r}\right]\overrightarrow{L}\cdot\overrightarrow{S} \\ &+ \frac{4\alpha_s}{m^2r^3}T \end{aligned} \tag{2.1}$$

where $\delta_\sigma(r) = (\sigma/\sqrt{\pi})^3 \exp -\sigma^2r^2$. The values for parameters (α_s, b, m_c σ)= $(0.5461, 0.1425\mathrm{GeV}^2, 1.4794\mathrm{GeV}, 1.0946\mathrm{GeV})$ have been determined by the fitting known resonances [15]. The ${}^3P_0$ model has been used to calculate partial decay widths for all open charm decays. In addition to the topics discussed above, exclusive charmonium decays represent a crucial testing ground for QCD predictions. Hadron helicity non-conserving

processes, $\mathcal{G}$-parity violating decays, radiative ψ' decays and hadronic χ_{cJ} decays are of particular interest.

2.3 Gluonic Excitations

The QCD spectrum is richer than that of the naive quark model because the gluons, mediating the strong force between quarks, can act as principal components of entirely new types of hadrons. These "gluonic hadrons" fall into two categories: glueballs and hybrids. Glueballs are predominantly excited states of glue while hybrids are resonances consisting largely of a quark, an antiquark, and excited glue. The additional degrees of freedom carried by gluons allow glueballs and hybrids to have spin-exotic quantum numbers J^{PC} that are forbidden for normal mesons and other fermion-antifermion systems. Exotic quantum numbers (e.g. $J^{PC} = 0^{--}$, 0^{+-}, 1^{-+}, 2^{+-}) provide the best opportunity to distinguish between gluonic hadrons and $q\overline{q}$ states. However, even non-exotic glueballs and hybrids can be identified by measuring an overpopulation of the experimental meson spectrum and by comparing properties, like masses, quantum numbers, and decay channels, with predictions from models or Lattice Quantum Chromodynamics (LQCD). The properties of glueballs and hybrids are determined by the long-distance features of QCD and their study will yield fundamental insight into the structure of the QCD vacuum.

The most promising results for gluonic hadrons have come from antiproton annihilation experiments. Two particles, first seen in πN scattering [31, 32] with exotic $J^{PC} = 1^{-+}$ quantum numbers, $\pi_1(1400)$ [33] and $\pi_1(1600)$ [34] are clearly seen in $\overline{\mathrm{p}}\mathrm{p}$ annihilation at rest.

In the search for glueballs, a narrow state at $1500\,\mathrm{MeV}/c^2$, discovered in antiproton annihilations by Crystal Barrel [35, 36, 37, 38, 39], is considered the best candidate for the glueball ground state ($J^{PC} = 0^{++}$). However, the mixing with nearby conventional scalar $q\overline{q}$ states makes the unique interpretation as a glueball difficult.

2.3.1 Hybrid Charmonium

The search for glueballs and hybrids has mainly been restricted to the mass region below $2.2\,\mathrm{GeV}/c^2$. Experimentally, it would be very rewarding to go to higher masses because of the unavoidable problems due to the high density of normal $q\overline{q}$ mesons below $2.5\,\mathrm{GeV}/c^2$. Here, the light quark states form a structure-less continuum and heavy quark states are far fewer in number and can easily be resolved. This is particularly true for the charmonium region. Exotic charmonia are expected to exist in the 3–5 GeV/c^2 mass region where they could be resolved and identified unambiguously.

Predictions for hybrids come mainly from calculations based on the bag model, flux tube model, and constituent gluon model and, recently, with increasing precision, from LQCD [40, 41]. For hybrids, the theoretical results qualitatively agree, lending support to the premise that the predicted properties are realistic. Charmonium hybrids can be expected since the effect of an extra gluonic degree of freedom in meson-like systems is evident in

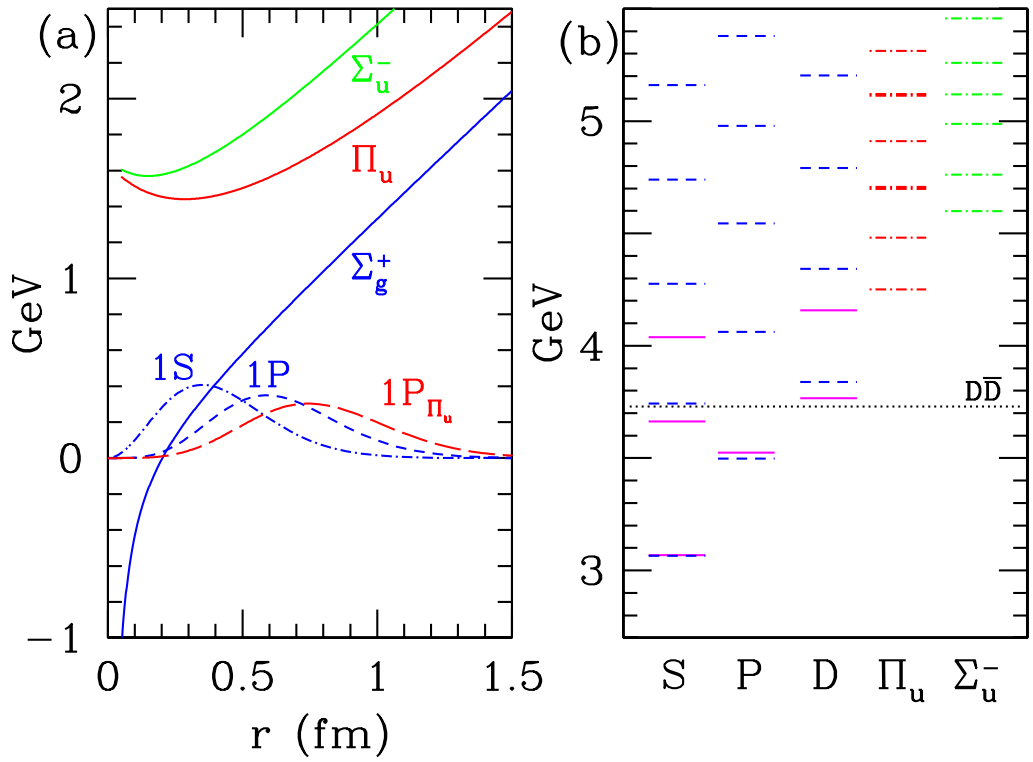

Figure 2.2: (a) Heavy quarkonium potentials and wave functions for different excitation levels from LQCD. Σ denotes normal one gluon exchange while the excited Π potentials are the lowest lying hybrid potentials. In that case, the attraction is not mediated by a single gluon but a string of gluons which carry angular momentum. (b) shows the charmonium spectrum from LQCD. The conventional charmonium states are on the right while the hybrids are found in column Π_u and Σ_u^-. See [28] for details.

the confining potentials for the $c\bar{c}g$ system (e.g. as derived from LQCD calculations in the Born-Oppenheimer approximation [41]).

The discussions have only been centered around the lowest-lying charmonium hybrids. Four of these states ($J^{PC} = 1^{--}, 0^{-+}, 1^{-+}, 2^{-+}$) correspond to a $c\bar{c}$ pair with $J^{PC} = 0^{-+}$ or 1^{--}, coupled to a gluon in the lightest mode with $J^{PC} = 1^{--}$. The other four states ($J^{PC} = 1^{++}, 0^{+-}, 1^{+-}, 2^{+-}$) with the gluon mode $J^{PC} = 1^{-+}$ are probably heavier. Three of the eight charmonium hybrids have spin-exotic quantum numbers ($J^{PC} = 0^{+-}$, 1^{-+}, 2^{+-}). Thus, mixing effects with nearby $c\bar{c}$ states are excluded and experimental identification is particularly simple. Compared to light hybrid candidates with reported widths of 200 to 400 MeV/c^2 [31, 32, 33, 34], charmonium hybrids are likely to be narrower since open-charm decays are forbidden or suppressed below the $D\overline{D}_J^* + c.c.$ (often referred to as DD^{**}) threshold. From experiments at LEAR we know that production rates of such $q\bar{q}$ states are similar to those of states with exotic quantum numbers. Thus, we estimate that the cross sections for the formation and production of charmonium hybrids will be similar to those of normal charmonium states which is in the order of 120 pb ($\bar{p}p \rightarrow J/\psi\pi^0$ [42]), in agreement with theoretical predictions [43].

Formation experiments would generate non-exotic charmonium hybrids with high cross sections while production experiments would yield a charmonium hybrid together with another particle, such as a π or an η. In $\overline{\mathrm{p}}\mathrm{p}$ annihilation, production experiments are the only way to obtain charmonium hybrids with exotic quantum numbers. It is envisaged that the first step of exploring charmonium hybrids would consist of production measurements at the highest antiproton energy available ($E_{\overline{\mathrm{p}}} = 15\,\mathrm{GeV}$, $\sqrt{s} = 5.46\,\mathrm{GeV}/c^2$) and studying all possible production channels available to cover exotic and non-exotic states. The next step would consist of formation measurements by scanning the antiproton energy in small steps in the regions where promising hints of hybrids have been observed in the production measurements, thus having a second check on the static properties like the J^{PC} assignment as well as mass and width.

2.3.2 Glueballs

LQCD calculations make rather detailed predictions for the glueball mass spectrum in the quenched approximation disregarding light quark loops [44]. For example, the calculated width of approximately $100\,\mathrm{MeV}/c^2$ [45] for the ground-state glueball matches the experimental results. LQCD predicts the presence of about 15 glueballs, some with exotic quantum numbers in the mass range accessible to the HESR.

Glueballs with exotic quantum numbers are called oddballs which cannot mix with normal mesons. As a consequence, they are predicted to be rather narrow and easy to identify experimentally [46]. It is conceivable that comparing oddball properties with those of non-exotic glueballs will reveal deep insight into the presently unknown glueball structure since the spin structure of an oddball is different [46]. The lightest oddball, with $J^{PC} = 2^{+-}$ and a predicted mass of $4.3\,\mathrm{GeV}/c^2$, would be well within the range of the proposed experimental program. Like charmonium hybrids, glueballs can either be formed directly in the $\overline{\mathrm{p}}\mathrm{p}$-annihilation process, or produced together with another particle. In both cases, the glueball decay into final states like $\phi\phi$ or $\phi\eta$ would be the most favorable reaction below $3.6\,\mathrm{GeV}/c^2$ while $J/\psi\eta$ and $J/\psi\phi$ are the first choice for the more massive states.

The indication for a tensor state around $2.2\,\mathrm{GeV}/c^2$ was found in the experiment of Jetset collaboration at LEAR [47]. The acquired statistics was not sufficient for the complementary reactions to be determined. The $\overline{\mathrm{P}}$ANDA collaboration plans to measure the $\overline{\mathrm{p}}\mathrm{p} \rightarrow \phi\phi$ channel with statistics of two orders of magnitude higher than in the previous experiments. Moreover, other reactions of two vector particle production, such as $\overline{\mathrm{p}}\mathrm{p} \rightarrow \omega\omega, K^*\overline{K^*}, \rho\rho$ will be measured. However, the best candidate for the pseudo-scalar glueball ($\eta_L(1440)$), studied comprehensively at LEAR by the Obelix collaboration [48]–[49], is not widely accepted to be a glueball signal because the calculations of LQCD predict its mass above $2\,\mathrm{GeV}/c^2$. Therefore, new data on many glueball states are needed to make a profound test of different model predictions.

$\overline{\mathrm{p}}\mathrm{p}$-annihilations present a unique possibility to search for heavier glueballs since alternative methods have severe limitations. The study of glueballs is a key to understanding long-distance QCD.

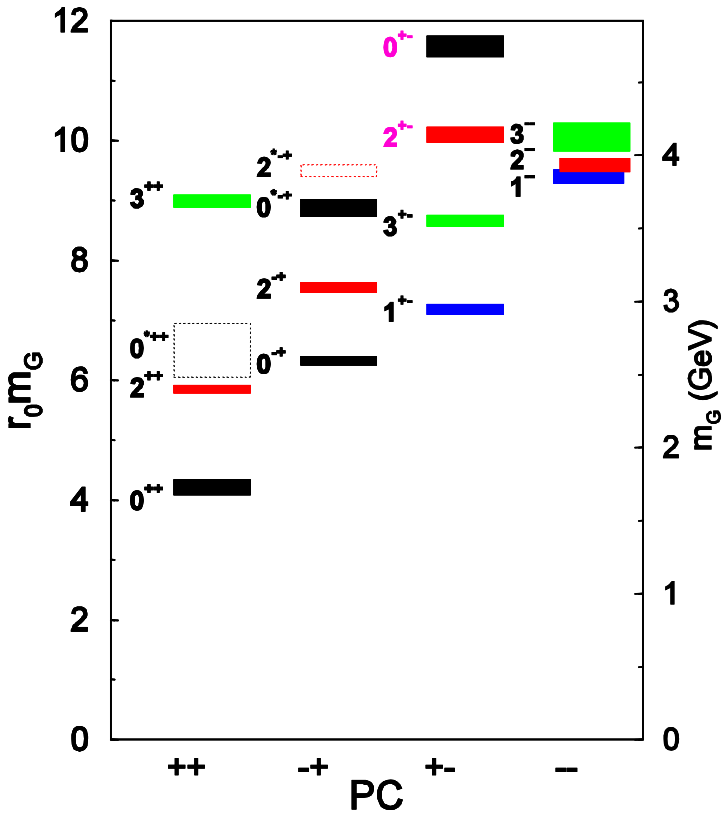

Figure 2.3: Glueball prediction from LQCD calculations. See [50, 44] for details.

2.3.3 Other Exotics

Other exotics like tetra- and pentaquark systems (up to $\approx 2.7\,\mathrm{GeV}/c^2$) are accessible in this energy range. Charmed pentaquarks would require an antiproton beam of at least $20\,\mathrm{GeV}/c$ and have consequently not been considered. Tetra-quark production can be investigated by Drell–Yan-like tagged events where one $q\overline{q}$ pair of the initial $\mathrm{p\overline{p}}$ system creates a lepton pair while the remaining four (anti)quarks form a bound state. The pentaquark production could be studied near threshold (e.g. $\overline{\mathrm{p}}\mathrm{p} \rightarrow \Theta^+\Theta^-$) where low partial waves dominate.

2.4 Charm in Nuclei

The investigation of medium modifications of hadrons embedded in hadronic matter is expected to further our understanding of the origin of hadron masses in the context of spontaneous chiral symmetry breaking in QCD and their modification due to chiral dynamics and partial restoration of chiral symmetry in a hadronic environment. The studies have been focused on the light quark sector due to the limitations in available energy. The in-medium potential of pions has been deduced from spectroscopic information obtained in the study of deeply bound pionic states [51, 52, 53]. Studies of K^+ production in

proton-nucleus collisions [54, 55] and of K^+ and K^- production in heavy-ion collisions [56, 57, 58, 59, 60] are consistent with repulsive and attractive mass shifts of these particles, respectively, in nuclear matter. The study of medium modifications of the light vector mesons (ρ, ω, ϕ), for which substantial changes of spectral functions in the medium are predicted to occur already at normal nuclear matter density [61], is the main research goal of the Hades and CBELSA/TAPS [62] experiments.

The high-intensity $\overline{\mathrm{p}}$ beam up of to 15 GeV/c will allow an extension of this program to the charm sector, both for hadrons with hidden and with open charm.

It should be noted that the availability of $\overline{\mathrm{p}}$ beams opens completely new opportunities to investigate the nuclear potential of strange hadrons. Apart from the formation of hypernuclei as discussed in Sec. 2.5, the production of slow K^- or $\overline{\Lambda}$ inside nuclei and the possible existence of nuclear bound states may be studied in $\overline{\mathrm{p}}$-nucleus collisions.

2.4.1 Charmonium Modification in Medium

The short-distance interaction of charmonium states, consisting of charm quarks only, with color singlet hadrons is governed by the exchange of two or more gluons. As the masses of charmonia are dominated by the large mass of the charm quark pair, only little sensitivity to changes in the quark condensate is expected for charmonium states. Consequently, the in-medium mass of these states would be affected primarily by a modification of the gluon condensate. Therefore, investigating the interaction of $c\overline{c}$ mesons with nucleons and nuclei is one way to explore fundamental aspects of gluon dynamics in QCD. However, recent calculations [63] indicate only small in-medium mass reductions of the order of 5–10 MeV/c^2 for the low lying charmonium states J/ψ and η_c. The situation may be different for excited charmonium states as this effect is expected to scale with the volume occupied by the $c\overline{c}$ pair. Large attractive mass shifts of 40 MeV/c^2 for χ_{cJ}, 100 MeV/c^2 for ψ', and 140 MeV/c^2 for $\psi(3770)$ were recently predicted by modelling a QCD 2^{nd} order Stark-effect [64, 65, 66]. An experimental verification of the in-medium mass shifts will give access to the strength of the gluon condensate inside nuclei.

2.4.2 Charmonium Absorption

Experimental information on charm propagation in nuclear matter is scarce and theoretical predictions are highly model dependent. In order to form a basis for a better understanding of the properties of charmed hadrons in nuclear matter, first studies within this research program should concentrate on the measurement of J/ψ and D meson production cross sections in $\overline{\mathrm{p}}$ annihilation on a series of nuclear targets. The comparison of the resonant J/ψ yield obtained from $\overline{\mathrm{p}}$ annihilation on protons and different nuclear targets allows to reliably deduce the J/ψ nucleon dissociation cross section [67]. This is particularly important for the understanding of J/ψ suppression in ultra-relativistic heavy-ion collisions, interpreted as a signal for a transition to a quark-gluon phase.

In particular, an exclusive measurement of the final states populated in $\overline{\mathrm{p}}$d collisions would allow to determine the coupling between different channels with charmed hadrons and to study the interaction of charmed hadrons with nucleons and mesons in the final state.

For example, the reaction $\overline{\mathrm{p}}\mathrm{d} \rightarrow J/\psi\gamma\mathrm{n}$ [68] provides the possibility to measure the elastic $J/\psi + N$ cross section down to low relative momenta.

2.4.3 Mass Shift of Charmed Mesons in Nuclei

Compared with *ccbar* system, for D mesons the situation is different. Built of a heavy c quark and a light antiquark, the D meson is the QCD analogue to the hydrogen atom. Hence, D mesons provide the unique opportunity to study the in-medium dynamics of a system with a single light quark. Recent theoretical work agrees in the prediction of a mass splitting for D mesons in nuclear matter but disagrees in the predicted size of the splitting ($50\,\mathrm{MeV}/c^2$ in Ref. [69, 70], $160\,\mathrm{MeV}/c^2$ in Ref. [71]) and in the sign of the D^- mass shift (attractive in Ref. [69, 70], repulsive in Ref. [71]). A smaller in-medium mass shift but a broad D meson spectral distribution is obtained in Ref. [72].

The experimental access to medium modifications of charmed hadrons is difficult. Whereas the in-medium mass of charmonia can be reconstructed from their decay into di-leptons or photons, different signals have been proposed for the detection of the in-medium mass shifts of D mesons. A reduction of the $D\overline{D}$ threshold can lead to an increased D and $\overline{D}$ production in $\overline{\mathrm{p}}$ annihilation on nuclei, in particular at sub-threshold energies [71]. D and $\overline{D}$ mesons can be identified via their hadronic decays with $\overline{K}$ and K mesons in the final state (See. Sec. **??**). Cross sections of typically 1 nb near threshold lead to about 100 events registered per day at a luminosity of $10^{31}\,\mathrm{cm}^{-2}\mathrm{s}^{-1}$ which would allow a substantial D meson physics program.

Moreover, a lowering of the $D\overline{D}$ threshold in the nuclear medium could open this decay channel or increase its partial width for the decay of the excited charmonium states lying close to the free $D\overline{D}$ mass ($\psi(3770)$, ψ', χ_{c2}) [70, 73], provided the reduction of the in-medium masses of the charmonium states is sufficiently large. Recent model calculations [64] indicate that a dropping of the $D\overline{D}$ threshold in the nuclear medium by $\sim 50\,\mathrm{MeV}/c^2$ could be seen in a suppression of low-mass di-leptons from the decay of the $\psi(3770)$.

Measuring the the ratio of $D/Dbar$ as a function of the target mass A will allow to set constrains on the D-meson absorption in the nuclear medium [74].

An observable modification of the excited charmonium spectral distribution due to the $D\overline{D}$ decay is not expected if the states exhibit substantial attractive in-medium mass shifts [65, 66] of similar size as the $D\overline{D}$ threshold. However, according to Refs. [65, 66] the mass shifts of the charmonium states may be deduced from their in-medium decay which is enhanced relative to the decay in the vacuum due to the collisional width along the path inside the nucleus.

2.5 Hypernuclei, Hyperatoms, and Di-baryons

Replacing an up or a down quark with a strange quark in a nucleon, which is bound in a nucleus, leads to the formation of a hypernucleus. A new quantum number, strangeness, is

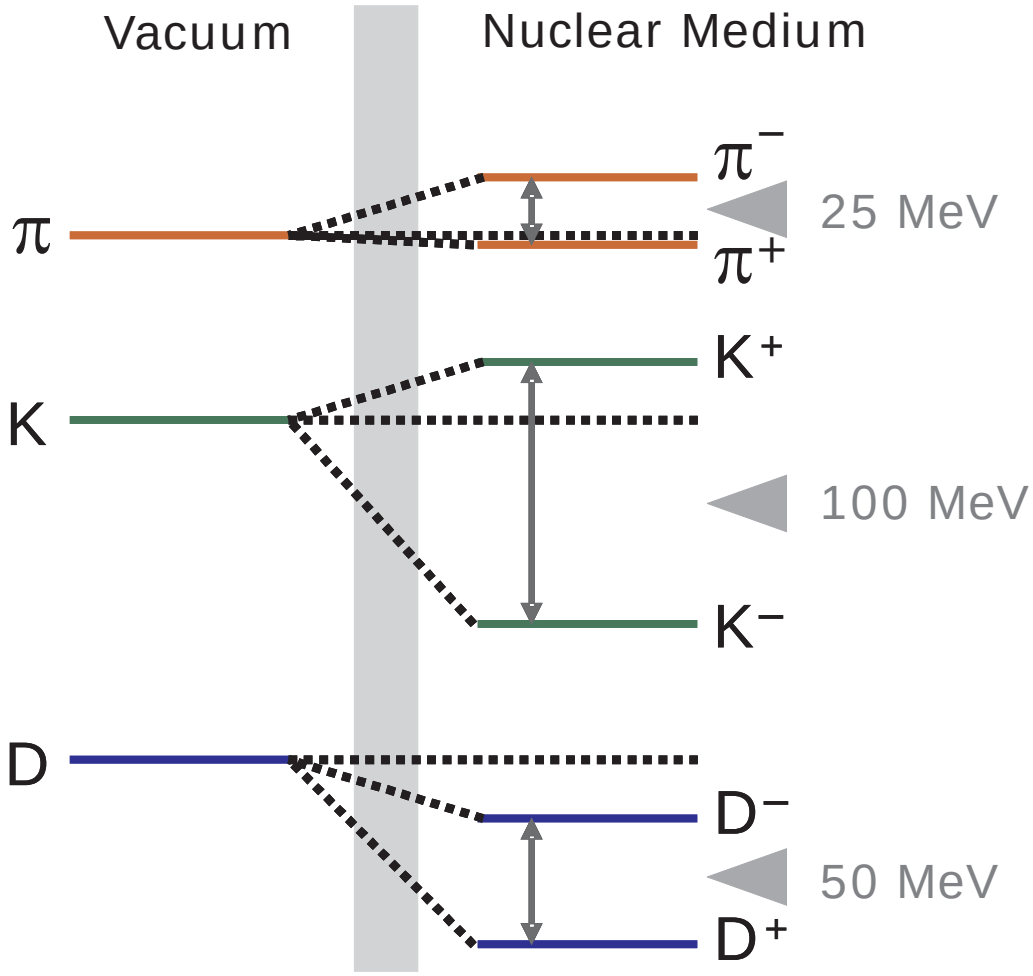

Figure 2.4: Shift of π, K and D mesons in the nuclear medium.

introduced into the nucleus, adding a third axis to the nuclear chart. Due to experimental limitations the third dimension has only scarcely been explored in the past.

Single and double Λ-hypernuclei were discovered 50 [75] and 40 years ago [76], respectively. However, only 6 double Λ-hypernuclei are presently known, in spite of a considerable experimental effort during the last 10 years. Thanks to the use of $\overline{\mathrm{p}}$ beams and the skillful combination of experimental techniques, copious production at $\overline{\mathrm{P}}$ANDA is expected, with even higher numbers than at (planned) dedicated facilities. A new chapter of strange nuclear physics will be opened whose first result will be the determination of the ΛΛ strong interaction strength, not feasible with direct scattering experiments.

The hyperon – usually a Λ particle – is not restricted by the Pauli principle in populating all possible nuclear states, in contrast to neutrons and protons. The description of hyperons occupying the allowed single-particle states is without the complications encountered in ordinary nuclei, like pairing interactions. The strength of the Λ-N strong interaction may be extracted with a description of the pure single-particle states by well known wave functions. Furthermore, the decomposition into the different spin-dependent contributions may be analyzed. For these contributions, significantly different predictions exist from meson exchange current and quark models. At the same time, the Λ-N weak

interaction can be studied where the Pauli principle acts in the opposite way: the decay of the Λ into $N\pi$ is suppressed, since all nucleon states in the nucleus are occupied. In contrast, the process $\Lambda N \rightarrow NN$ is allowed, opening a unique window for four-baryon, strangeness non-conserving interaction.

The possible existence of an $S = -2$ six-quark ($uuddss$) H-di-baryon [77, 78] represents another challenging topic of $\Lambda\Lambda$ hypernuclear physics. The experimental search for this lightest strangelet has been inconclusive. Moreover, even a strongly bound H-particle cannot be excluded [79]. In fact, the short time scale in a coalescence process, of the order of 10^{-23} s, may prevent the transition from a $\Lambda\Lambda$ state to an H-particle in free space. Here, double Λ-hypernuclei may serve as a catalyst for the H-particle. The long lifetime, of the order of 10^{-10} s, of two Λ hyperons bound together in a nucleus may help to overcome a possible repulsive interaction at short distances. It might be possible to observe its traces since the mass of the H-particle might drop inside a nucleus [80] and due to hyperon mixing [81, 82]. Thus, high resolution spectroscopy of $S = -2$ hypernuclei can give important information on this fascinating object.

Finally, hyperatoms created during the capture process of the hyperon will supply new information on fundamental properties of hyperons. Intrinsic properties of hadrons reflect the properties of the mutual interaction between the individual constituents inside the complex particles. The Ω hyperon (sss) is particularly interesting because of its long lifetime of 82 ps and the spin quantum number of 3/2. It is the only elementary baryon with a non-vanishing spectroscopic quadrupole moment, $Q_s \propto 3J_z^2 - J(J+1)$. As a consequence, the quadrupole moment can principally be measured directly without taking recourse to theoretical models [83] by the hyperfine splitting in Ω^- atoms. It is expected that the Ω^- quadrupole moment is mainly determined by the one-gluon exchange contribution to the quark-quark interaction [84]. However, predictions of the Ω quadrupole moment in various models range from 0 to about $3 \cdot 10^{-2}\,\mathrm{e} \cdot \mathrm{fm}^2$ [85]. The measurement will not only provide first information on the shape of a baryon but also represents a unique benchmark for our understanding of the quark-quark interaction. Like in the deuteron, where the long-range tensor potential is tested by the quadrupole moment, the tensor component of the quark-quark interaction determines the quadrupole deformation of the Ω hyperon. In addition, the simplicity of the Ω baryon with 3 identical and rather heavy quarks makes it an ideal test case for theoretical studies on the lattice. The $\overline{\mathrm{p}}\mathrm{p} \rightarrow \Omega\overline{\Omega}$ reaction makes it possible to produce a large number of Ω^- atoms and to observe x-ray transition from the exotic atoms. However, a precise measurement of the hyperfine splitting caused by the quadrupole moment of the Ω^- will require additional effort [86].

2.6 Further Options

2.6.1 Open charm physics

HESR running with full luminosity (limited by the production rate of $2{\cdot}10^7\,\overline{\mathrm{p}}$/s) at momenta larger than 6.4 GeV/c would produce large numbers of D meson pairs. Such an installation can be considered as a hadronic factory for tagged open charm, with about 100/ s charmed pairs around $\psi(4040)$. Despite the small ratio ($5{\cdot}10^{-6}$) of charm produc-

tion to total cross section, the background conditions are expected to be favorable because the hadrons are produced at threshold without phase space for additional hadrons in the same process. The high yield [87] and the well defined production kinematics of D meson pairs allows to investigate e.g. D and D_s and their rich physics spectrum.

2.6.1.1 Open Charm Spectroscopy

The B-Factory experiments have discovered several resonances in the D ($c\overline{d}$, $c\overline{u}$ and c.c.) and D_s ($c\overline{s}$ and c.c.) sector where two are extremely narrow, ($D^*_{sJ}(2317)$ [88] and $D_{sJ}(2458)$ [89]-[90]). The measurements have triggered intense discussions since they appear at unexpected locations giving rise to speculations about their nature. The large mass shift (compared to theoretical predictions [91]) is discussed in terms of chiral aspects in heavy-light systems [92, 93]. The models would have strong implications on any system with a single light quark [94]. It is important to verify this finding and to settle this question albeit that there is some evidence for the scalar D-state [95, 96]. Threshold pair production can be employed for precision measurements of the mass and the width of narrow excited D and D_s states.

2.6.1.2 Rare Decays

The study of rare decays can open a window onto physics beyond the standard model since it probes symmetry violation. Lepton flavor number violating decays, e.g. $D^0 \rightarrow \mu e$ or $D^{\pm} \rightarrow \pi\mu e$, could be searched for. Flavor changing neutral currents like in the decay $D^0 \rightarrow \mu^+\mu^-$ can occur in the standard model through box graphs or weak penguin graphs with branching fractions smaller than 10^{-15}. However, the signatures of the decays are clean leaving hope for their observation, if processes exist that boost the decay branch.

2.6.1.3 $\mathcal{CP}$ Violation

$\mathcal{CP}$ violation [97] has been observed in neutral kaon and in neutral B meson decays [98, 99]. In the standard model, $\mathcal{CP}$ violation arises from a single phase entering the Cabbibo-Kobyashi-Maskawa (CKM) matrix. As a result, two elements of this matrix, i.e. V_{ub} and V_{td} have large phases. The elements have small magnitudes and involve the third generation and $\mathcal{CP}$ violation is small in the K^0 system. The violation is predicted to be even smaller in the D^0 system [100]. Thus, a deviation from the small standard model effect indicating "new physics" can be more easily distinguished in experiments in the D meson system.

Working with D mesons produced at the $D\overline{D}$ threshold has advantages arising from the strong correlation of the $D\overline{D}$ pair which is kept in the hadronization process. Formed near threshold, asymmetries are not expected in the production process and the observation of one D meson reveals the quantum numbers of the other one when produced in a charge symmetric environment (flavor tagging). Thus, flavor ($D\overline{D}$) mixing and $\mathcal{CP}$ violation can be searched for in analogy to methods in the B-system produced on the $\Upsilon(4S)$ [101].

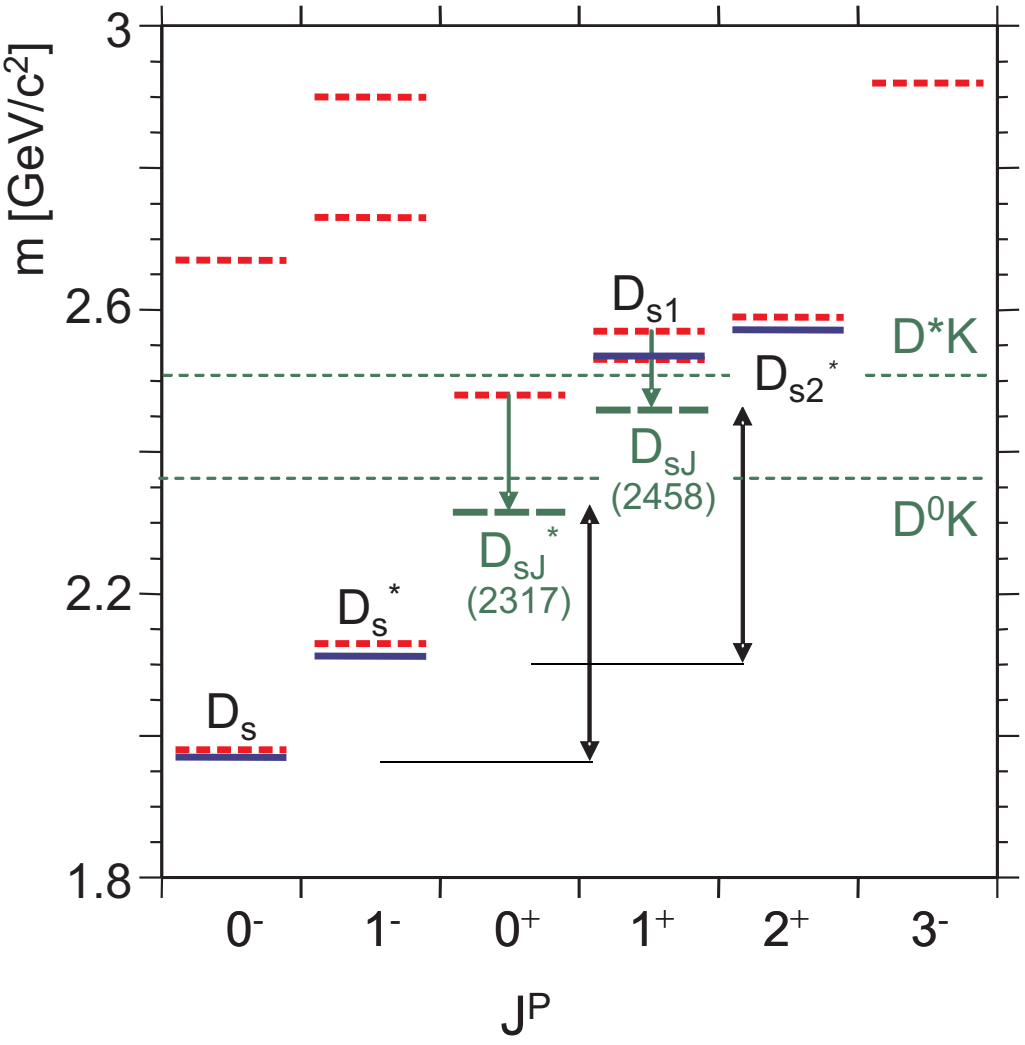

Figure 2.5: Spectrum of D_s mesons. The newly found $D^*_{sJ}(2317)$ and $D_{sJ}(2458)$ may fit into the $q\overline{q}$ spectrum but the masses are more than 140 MeV/c^2 lower than expected from potential models, thus showing strong chiral effects.

2.6.2 Crossed-channel Compton Scattering and Related Exclusive Processes

The theoretical framework of Generalized Parton Distributions (GPDs) [102, 103] has recently been developed [104, 105, 106]. The results caused excitement in the field of understanding the structure of the nucleon in terms of QCD. It has recently been shown that exclusive $\overline{\mathrm{p}}\mathrm{p}$ annihilation into two photons at large s and t can be described in terms of GPDs [107, 108, 21]. Using the handbag diagram (Fig. 2.6), the process separates into a soft part which is parametrized by GPDs and a hard part which describes the annihilation of a quasi-free $q\overline{q}$ pair into two photons. Estimates of the expected count rates based on a simple model predict a few thousand $\gamma\gamma$-events per month for a luminosity of $2 \cdot 10^{32}\,\mathrm{cm}^{-2}\mathrm{s}^{-1}$ at an energy of $\sqrt{s} = 3.2\,\mathrm{GeV}/c^2$ [109]. Other estimates, based on cross

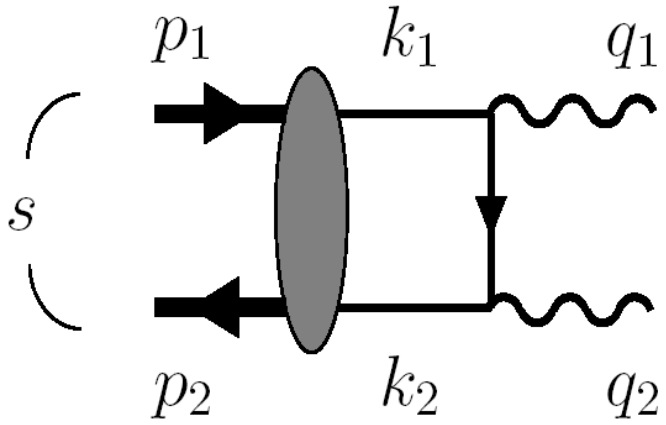

Figure 2.6: Using the handbag diagram, the $\overline{\mathrm{p}}\mathrm{p}$ annihilation into two photons can be separated into a soft part which is parametrized by GPDs and a hard part which is described by QCD.

section measurements of the inverse process $\gamma\gamma \rightarrow \overline{\mathrm{p}}\mathrm{p}$, predict count rates up to a factor 50 [110, 111] above the estimate of [109] but still are consistent with the handbag ansatz. The experiment E760 at Fermilab has measured the process $\overline{\mathrm{p}}\mathrm{p} \rightarrow \gamma\gamma$ at various angles. However, the measured count rates were dominated by background from processes like $\overline{\mathrm{p}}\mathrm{p} \rightarrow \pi^0\pi^0$ [112].

2.6.3 Transverse Quark Distributions and Drell–Yan Processes

At leading twist and under the assumption of collinear factorization, the quark structure of hadrons is described by three distribution functions:

- the unpolarized function $f_1(x)$ representing up to a gauge link the probability of finding a quark with a fraction x of the light cone $p^+ \equiv p_z + p^0$ momentum of the parent hadron, regardless of its spin orientation
- the longitudinal polarization distribution $g_1(x)$ that measures the net helicity of a quark in a longitudinally polarized hadron
- the transversity $h_1(x)$ which is the distribution of transversely polarized quarks in a transversely polarized hadron

The distributions $f_1(x)$, $g_1(x)$ and $h_1(x)$ would contain all information on the internal dynamics of the nucleon if quarks were perfectly collinear and massless. However, the quark transverse momentum is not always negligible. In particular, it is essential in understanding the semi-inclusive DIS, the transverse momentum distribution of Drell-Yan lepton pairs, low Q^2 and low $x_{Bjorken}$ physics. A number of additional distribution functions arrize, if the quark transverse momentum is not put to zero. In particular, two T-odd functions, the distribution functions of an unpolarized quark inside a transversely

polarized parent hadron, $f_{1T}^{\perp}(x, \boldsymbol{k}_{\perp}^2)$, and of a transversely polarized quark inside an unpolarized parent hadron, $h_1^{\perp}(x, \boldsymbol{k}_{\perp}^2)$, are needed to describe the nucleon structure. The latter function $h_1^{\perp}(x, \boldsymbol{k}_{\perp}^2)$ is also called transversity. The experimental information on $h_1(x)$ and

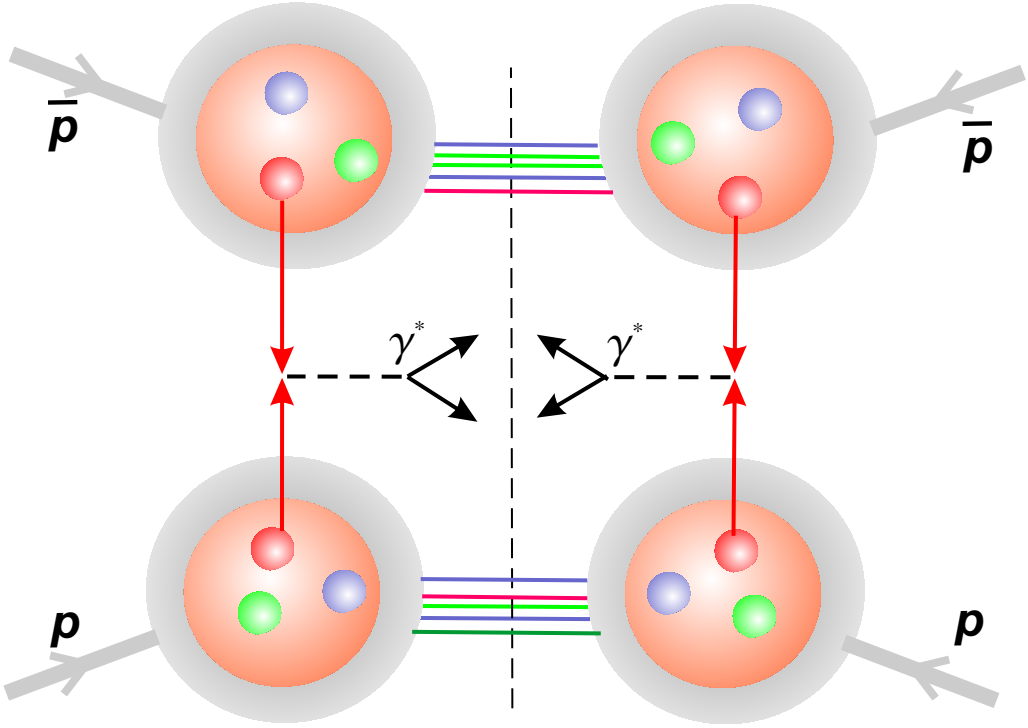

Figure 2.7: Drell–Yan dilepton production.

on $h_1^{\perp}(x)$ is very poor. The distributions, being chirally odd, are not observable in fully inclusive deep inelastic scattering (DIS), the reaction that provided the largest amount of the existing data on structure functions. Data on transversity are presently collected by COMPASS on semi-inclusive DIS and HERMES.

On the other hand, $h_1(x)$ can be extracted from the SIDIS measurements only by unfolding the data with fragmentation functions obtained from other experiments. The study of quark transversity via Drell–Yan lepton pair production in $\overline{\mathrm{p}}\mathrm{p}$ collisions is more direct. Fig. 2.7 shows k and k' as the four-momenta of the quark q and antiquark $\overline{q}$ annihilating into a virtual photon (with four-momentum q) that originates the lepton pair with invariant mass M. This represents the leading order of perturbative QCD constribution to the Drell-Yan lepton pair production process. The Drell–Yan cross section will depend on the cross-section of the elementary $q\overline{q} \rightarrow \gamma^*$ process. The transverse distributions of valence quarks appear unsuppressed by M^2 and the cross section does not contain unknown quantities besides the transversity themselves. This makes theoretical predictions and analysis more reliable compared to the other reactions.

Measurement of the angular distribution of dileptons, for unpolarized p and $\overline{\mathrm{p}}$ can shed light on this problem.

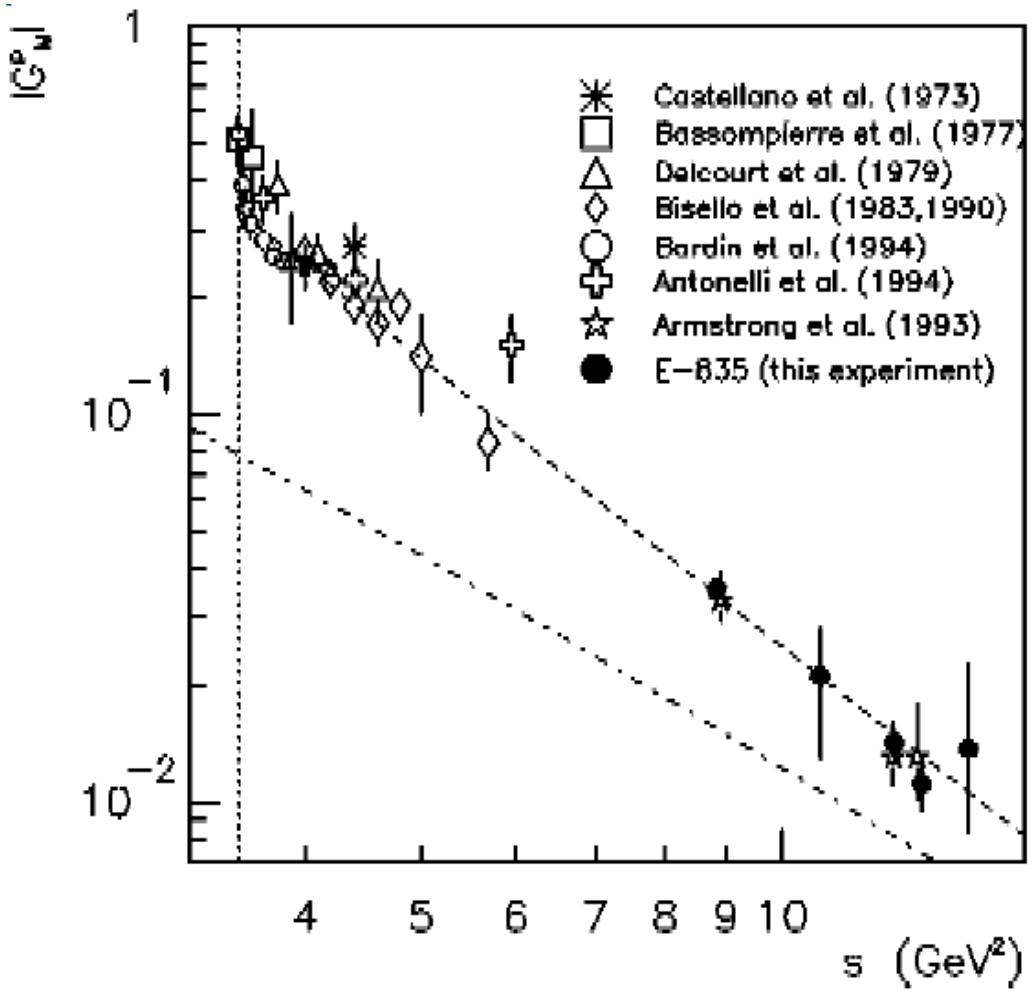

Figure 2.8: Electromagnetic form factor $|G_M|$ measurements for proton.

2.6.4 Electromagnetic Form Factors of the Proton in the Time-Like Region

The electromagnetic form factor of the proton in the time-like region can be extracted from the cross sections for the process $\overline{\mathrm{p}}\mathrm{p} \rightarrow e^+e^-$. First order QED predicts:

$$\begin{aligned} \frac{d\sigma}{d\cos\theta^*} &= \frac{\pi\alpha^2\hbar^2c^2}{2xs}\left[|G_M|^2(1+\cos^2\theta^*)\right. \\ &+ \left.\frac{4m_p^2}{s}|G_E|^2(1-\cos^2\theta^*)\right] \end{aligned} \tag{2.2}$$

with G_E and G_M the electric and magnetic form factors, respectively. Data at high Q^2 are crucial to test the Q^2 behavior and the space-like–time-like equality for corresponding Q^2.

The proton time-like form factors have been measured by several experiments in the low Q^2 region down to threshold. At high Q^2 the only measurements have been achieved by E760 and E835 at Fermilab [113, 114] up to $Q^2 \approx 15\,\mathrm{GeV}^2/c^2$ (see also Fig. 2.8). However,

due to limited statistics $|G_M|$ and $|G_E|$ have not been measured separately and could only be extracted using the assumption $|G_E| = |G_M|$.

In $\overline{\mathsf{P}}$ANDA, it will be possible to determine the form factors over the widest Q^2 range with a single experiment, from threshold to $20\,\mathrm{GeV}^2/c^4$ and above, depending on the beam time availability. Due to much improved statistics and angular coverage it will be possible to significantly improve the results of E760 and E835 and to measure $|G_M|$ and $|G_E|$ separately.

The real and imaginary parts of the time-like form factors could be determined with a polarized beam and/or target. A modulation of the azimuthal distribution will certainly help disentangling the electric and the magnetic parts and provide information on the relative phase, even if this will be most likely limited by the luminosity to moderate Q^2 values. Most of the anticipated measurements could be run together with other programs but not close to resonance peaks.

References

[1] K. Seth, in *Proceedings of "Heavy Flavours 8"*, 1999.

[2] S. K. Choi et al., Phys. Rev. Lett. **89**, 102001 (2002), hep-ex/0206002.

[3] D. M. Asner et al., Phys. Rev. Lett. **92**, 142001 (2004), hep-ex/0312058.

[4] B. Aubert et al., Phys. Rev. Lett. **92**, 142002 (2004), hep-ex/0311038.

[5] C. Edwards et al., Phys. Rev. Lett. **48**, 70 (1982).

[6] F. Fang et al., Phys. Rev. Lett. **90**, 071801 (2003).

[7] M. Andreotti et al., Phys. Lett. **B566**, 45 (2003).

[8] B. Mayer, private comm.

[9] K. Gollwitzer, PhD. diss (1993).

[10] T. Armstrong et al., Phys. Rev. Lett. **69**, 2337 (1992).

[11] C. Patrignani, talk presented at "BEACH04", Chicago, U.S.A., June 2004.

[12] A. Tomaradze, talk presented at "QWG04", Beijing, China, October 2004.

[13] T. Armstrong et al., Phys. Rev. **D48**, 3037 (1993).

[14] M. Ambrogiani et al., Phys. Rev. **D62**, 052002 (2000).

[15] T. Barnes, S. Godfrey, and E. Swanson, hep-ph/0505002 (2005).

[16] S. Eidelman et al., Phys. Lett. **B592**, 1+ (2004), http://pdg.lbl.gov.

[17] J. Bai et al., Phys. Rev. **D57**, 3854 (1998).

[18] L. Antoniazzi et al., Phys. Rev. **D50**, 4258 (1994).

[19] G. De Rujula, Georgi, ??? **-**, (1976).

[20] L. Okun, MV'77 **-**, (1977).

[21] F. Close and Zhao, Phys. Lett. **B553**, 211 (2003).

[22] S. K. Choi et al., Phys. Rev. Lett. **91**, 262001 (2003).

[23] D. Acosta et al., Phys. Rev. Lett. **93**, 072001 (2004).

[24] V. Abazov et al., Phys. Rev. Lett. **93**, 162002 (2004), hep-ex/0405004.

[25] B. Aubert et al., subm. to Phys. Rev. Lett. (2004), hep-ex/0406022.

[26] K. L. E. Eichten and C. Quigg, Phys. Rev. Lett. **89**, 162002 (2002).

[27] T. Barnes and S. Godfrey, Phys. Rev. D **69**, 054008 (2004).

[28] K. Juge, J. Kuti, and C. Morningstar, Phys. Rev. Lett. **90**, 161601 (2003).

[29] N. Tornqvist, Phys. Lett. B **590**, 209 (2004).

[30] M. Voloshin, Phys. Lett. B **579**, 316 (2004).

[31] D. Thompson et al., Phys. Rev. Lett. **79**, 1630 (1997).

[32] G. Adams et al., Phys. Rev. Lett. **81**, 5760 (1998).

[33] A. Abele et al., Phys. Lett. **B423**, 175 (1998).

[34] J. Reinnarth, Nucl. Phys. **A692**, 268c (2001).

[35] C. Amsler et al., Phys. Lett. **B342**, 433 (1995).

[36] C. Amsler et al., Phys. Lett. **B353**, 571 (1995).

[37] A. Abele et al., Phys. Lett. **B385**, 425 (1996).

[38] A. Abele et al., Eur. Phys. J. **C19**, 667 (2001).

[39] C. Amsler et al., Phys. Lett. **B340**, 259 (1994).

[40] P. Chen, X. Liao, and T. Manke, Nucl. Phys. Proc. Suppl. **94**, 342 (2001).

[41] C. Michael, in *Proceedings of "Heavy Flavours 8"*, 1999.

[42] R. Cester, in *Proceedings of the "Super LEAR Workshop"*, pages 91–103, Zürich, 1991.

[43] M. Gaillard, L. Maiani, and R. Petronzio, Phys. Lett. **B110**, 489 (1982).

[44] C. Morningstar and M. Peardon, Phys. Rev. **D60**, 34509 (1999).

[45] J. Sexton, A. Vaccarino, and D. Weingarten, Phys. Rev. Lett. **75**, 4563 (1995).

[46] P. Page, in *Proceedings of the "pbar2000 Workshop"*, edited by D. Kaplan and H. Rubin, pages 55–64, Chicago, 2001.

[47] R. Jones, in *Proceedings of the workshop "Gluonic excitations"*, Jefferson Lab, 2003, in print.

[48] A. Bertin et al., Phys. Lett. **B400**, 187 (1995).

[49] F. Nichitiu et al., Phys. Lett. **B545**, 261 (2002).

[50] C. Morningstar and M. Peardon, Phys. Rev. **D56**, 4043 (1997).

[51] H. Geissel et al., Phys. Rev. Lett. **88**, 122301 (2002).

[52] H. Geissel et al., Phys. Lett. **B549**, 64 (2002).

[53] H. Geissel et al., Phys. Rev. Lett. **92**, 072302 (2004).

[54] M. Nekipelov et al., Phys. Lett. **B540**, 207 (2002).

[55] Z. Rudy et al., Eur. Phys. J. **A15**, 303 (2002).

[56] Y. Shin et al., Phys. Rev. Lett. **81**, 1576 (1998).

[57] R. Barth et al., Phys. Rev. Lett. **78**, 4007 (1997).

[58] F. Laue et al., Phys. Rev. Lett. **82**, 1640 (1999).

[59] P. Crochet et al., Phys. Lett. **B486**, 6 (2000).

[60] K. Wisniewski et al., Eur. Phys. J. **A9**, 515 (2000).

[61] F. Klingl, N. Kaiser, and W. Weise, Nucl. Phys. **A624**, 527 (1997).

[62] D. T. et all, Phys. Rev. Lett. **94**, 192303 (2005).

[63] F. Klingl, S. Kim, S. Lee, P. Morath, and W. Weise, Phys. Rev. Lett. **82**, 3396 (1999).

[64] Y. Golubeva, E. Bratkovskaya, W. Cassing, and L. Kondratyuk, Eur. Phys. J. **A17**, 275 (2003).

[65] S. Lee and C. Ko, Phys. Rev. **C67**, 038202 (2003).

[66] S. Lee, Proceedings of Int. Workshop 'HADRON 2003', in *Hadron Spectroscopy*, edited by H. K. E. Klempt and H. Orth, Aschaffenburg, 2004.

[67] K. Seth, Proceedings of Int. Workshop 'Structure of Hadrons', Hirschegg, 2001.

[68] W. Cassing, Y. Golubeva, and L. Kondratyuk, Eur. Phys. J. **A7**, 279 (2000).

[69] W. Weise, Proceedings of Int. Workshop 'Structure of Hadrons', Hirschegg, 2001.

[70] A. Hayashigaki, Phys. Lett. **B487**, 96 (2000).

[71] A. Sibirtsev, K. Tsushima, and A. Thomas, Eur. Phys. J. **a6**, 351 (1999).

[72] L. Tolós, J. Schaffner-Bielich, and A. Mishra, hep-ph/0411256.

[73] B. Friman, S. Lee, and T. Song, Phys. Lett. **B548**, 153 (2002).

[74] W. C. Y. Golubeva and L. Kondratyuk, Eur. Phys. J. **A14**, 255 (2002).

[75] M. Danysz and J. Pniewski, Phil. Mag. **44**, 348 (1953).

[76] M. Danysz et al., Nucl. Phys. **49**, 121 (1963).

[77] R. L. Jaffe, Phys. Rev. Lett. **38**, 195 (1977).

[78] R. L. Jaffe, Phys. Rev. Lett. **38**, 617E (1977).

[79] G. R. Farrar and G. Zaharijas, hep-ph/0303047, 2003.

[80] T. Sakai et al., Prog. Theor. Phys. Suppl. **137**, 121 (2000).

[81] T. Yamada and C. Nakamoto, Phys. Rev. **C62**, 034319 (2000).

[82] I. N. Filikhin, A. Gal, and V. M. Suslov, nucl-th/0303028.

[83] R. M. Sternheimer and M. Goldhaber, Phys. Rev. **A8**, 2207 (1973).

[84] A. J. Buchmann, Z. Naturforschung **52**, 877 (1997).

[85] Y. Oh, Mod. Phys. Lett. **A10**, 1027 (1995).

[86] A. Buchmann and E. Henley, Phys. Rev. D **65**, 073017 (2002).

[87] Y. G. W. Cassing and L. Kondratyuk, Eur. Phys. J. **A7**, 279 (2000).

[88] B. Aubert et al., Phys. Rev. Lett. **90**, 242001 (2003).

[89] D. Besson et al., hep-ex/0305100.

[90] Y. Mikami et al., hep-ex/0307052.

[91] N. Isgur, R. Kokoski, and J. Paton, Phys. Rev. Lett. **54**, 869 (1985).

[92] M. Nowak, M. Rho, and I. Zahed, hep-ph/0307102.

[93] W. Bardeen, E. Eichten, and T. Hill, hep-ph/0305049.

[94] M. Nowak, hep-ph/0311154.

[95] K. Abe et al., hep-ex/0307021.

[96] J. M. Link et al., Phys. Lett. **B586**, 11 (2004), hep-ex/0312060.

[97] I. Bigi, Surveys High Energy Phys. **12**, 269 (1998).

[98] B. Aubert et al., Phys. Rev. Lett. **87**, 091801 (2001).

[99] K. Abe et al., Phys. Rev. Lett. **87**, 091802 (2001).

[100] G. Burdman, hep-ph/9407378.

[101] P. Harrison and H. Quinn, editors, *The Babar Physics Book*, SLAC, 1998, SLAC-R-504.

[102] K. Goeke, M. Polyakov, and M. Vanderhaeghen, Prog. Part. Nucl. Phys. **47**, 401 (2001).

[103] M. Diehl, (2003), hep-ph/0307382.

[104] D. Müller et al., Fortschr. Phys. **42**, 101 (1994).

[105] A. Radyushkin, Phys. Lett. **B380**, 417 (1996).

[106] X.-D. Ji, Phys. Rev. Lett. **78**, 610 (1997).

[107] A. Radyushkin, Phys. Rev. D **58**, 114008 (1998).

[108] M. Diehl, Eur. Phys. J. **C8**, 409 (1999).

[109] A. Freund, A. Radyushkin, A. Schäfer, and C. Weiss, Phys. Rev. Lett. **90**, 092001 (2003).

[110] M. Diehl, P. Kroll, and C. Vogt, Eur. Phys. J. **C26**, 567 (2002).

[111] C. Berger and W. Schweiger, Eur. Phys. J. **C28**, 249 (2003).

[112] T. Armstrong et al., Phys. Rev. **D56**, 2509 (1977).

[113] T. Armstrong et al., Phys. Rev. Lett. **70**, 1212 (1993).

[114] M. Ambrogiani et al., Phys. Rev. **D60**, 032002 (1999).

Chapter 3

Detector Overview

3.1 Introduction

The rich physics program, as described in Chap. 2, poses significant challenges on a detector. $\overline{\text{P}}$ANDA must be a universal and hermetic apparatus capable of detecting charged and neutral particles with nearly 4π solid angle coverage and high resolution.

The basic requirements are summarised for the individual detectors itself:

- Hidden-charm physics and the search for exotics require the concurrent detection of lepton pairs as well as good kaon identification and high efficiency for open-charm final states. In addition, the detection of low energy photons, either from radiative decays and/or background channels, is extremely important. Thus, muon detection capability and a highly-segmented low-threshold electromagnetic calorimeter are important for the tagging and precise reconstruction of hidden-charm and the reduction of background. Good vertex recognition and particle identification for charged kaons from very low energies up to a few GeV/c is mandatory to reconstruct light hadronic and open charm final states.

- The detector must withstand large radiation dosage from hadrons emitted from the spallation process when using nuclear targets. Spallation products are dominated by neutrons down to thermal energies.

- The specific demands for experiments with a secondary target require good detection of anti-hyperons and low momentum K^+ in the forward region. A compact high resolution solid state tracker for absorption and tracking of low momentum hyperons at large angles is needed. The geometry of the secondary target is determined by the short mean life time of the Ξ^- of only 0.164 ns. A high resolution and high-efficiency Ge-array for γ-ray detection is envisaged in order to measure radiative transitions.

- Open-charm spectroscopy and electromagnetic reactions have similar demands as are envisaged in the hidden-charm and exotics programs (see Sec. 2.2 and 2.3). It should be mentioned that the decay of a charmed hadron releases rather high p_t (up to 1.5 GeV/c) as compared to light and even strange meson decays. This leads to large opening angles of particles in the laboratory reference frame.

The requirements on the detector for the specific physical processes are summarized in the following section.

3.2 Detector Requirements

3.2.1 Charmonium Spectroscopy

An important advantage of using antiproton-proton annihilation for charmonium spectroscopy measurements is that charmonium states with any quantum number can be produced in both production and formation experiments. In both cases, the detection strategy is based on either a clean identification of the charged lepton pair or the multiple hadrons in the final state. As an example for typical momenta, the momentum vs. polar angle correlation of the final state muons emitted in a formation experiment of the $\psi(3686)$ is plotted in Fig. 3.1 a.

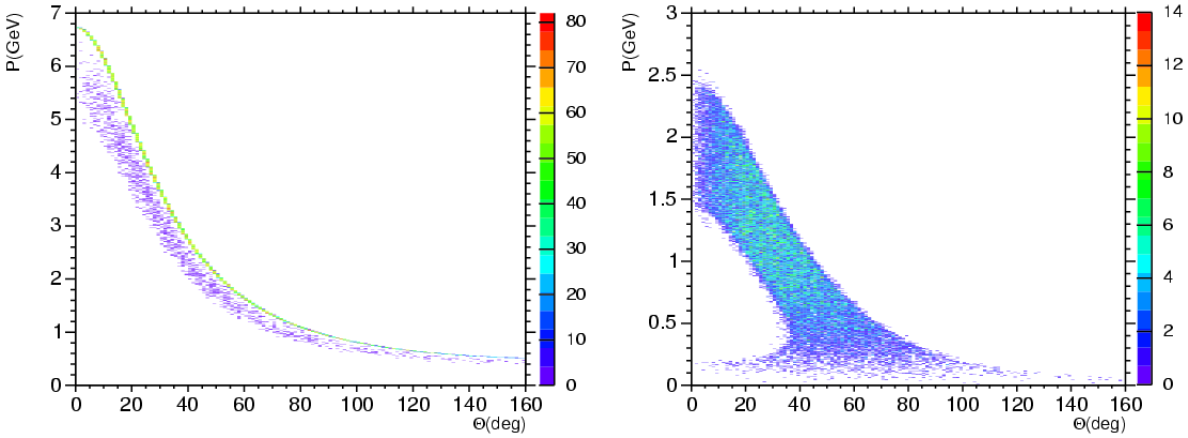

(a) distribution of muons (b) distribution of kaons

Figure 3.1: Momentum *vs.* polar angle distribution of a) muons from the formation reaction of the $\psi(3686)$ and b) kaons from the reaction $\overline{\mathrm{p}}\mathrm{p} \rightarrow \phi\phi$ at $\sqrt{s} = 3.6\,\mathrm{GeV}$.

In this figure, the sharp line corresponds to the dilepton decay of the ψ. In addition, a broader band results from the cascade $\psi' \rightarrow J/\psi X$ ($J/\psi \rightarrow \mu^+\mu^-$). The equivalent distribution for e^+ and e^- looks similar, except for additional contributions from Dalitz decays of decay hadrons. Muon identification is only possible up to laboratory polar angles Θ of about 60°. Beyond these angles, the muon momentum is too low for muon/hadron discrimination. The momentum versus polar angle distribution for decay hadrons is restricted below the lepton curve due to kinematic constraints. For example, the decay kaons extend up to $\Theta \approx 60°$ and have a maximum yield near $\Theta = 20°$ and $p = 1.5\,\mathrm{GeV}/c$.

3.2.2 Charmed Hybrids

The studies involve final state particles with a similar angle/momentum distribution as for the hadronic decay of charmonium states. For example, the polar angle versus particle momentum correlation is presented in Fig. 3.1 b for the reaction $\overline{\mathrm{p}}\mathrm{p} \rightarrow \phi\phi \rightarrow 4K$ at $\sqrt{s} = 3.6\,\mathrm{GeV}$. The distribution demonstrates the need for pion-kaon separation up to $\sim 3\,\mathrm{GeV}/c$ at forward angles. By exploiting the relationship between the ring radius and velocity, a radiator with index of refraction $n = 1.02$ is suitable at forward angles and a higher value of n is required for larger polar angles.

3.2.3 Open Charm Hadrons

Most processes of interest involving D mesons take place at small excess c.m. energies so that the D mesons themselves are mostly produced in the forward direction. The kinematics of the decay particles are therefore mostly determined by the D meson decay itself. The decay of a charmed hadron releases a rather high p_t (up to $1.5\,\mathrm{GeV}/c$) as compared to light and even strange meson decays. This leads again to large opening angles of the decay particles in the laboratory reference frame.

As an example the decay, $\mathrm{D}^*(2010)^{\pm} \rightarrow D^0\pi^{\pm} \rightarrow K^{\mp}\pi^{\pm}\pi^{\pm}$ was studied at $\sqrt{s} = 4.04\,\mathrm{GeV}$. $\mathrm{D}^*(2010)^{\pm}$-mesons have a very small decay phase space, because of that pions from this decay have a very small momentum and emitted to the cone with a opening angle smaller 30° (on the Fig. 3.2 a they are outlined by ellipse), whereas pions and kaons from D^0 decays can be emitted at much larger angles - 45° or even 60° for kaons while pions can be ejected even backward (see Fig. 3.2 a). Similar distributions are expected for other charmed hadrons, for instance $\mathrm{D}^{\pm}$ at $\sqrt{s} = 3.77\,\mathrm{GeV}$(see Fig. 3.2 b).

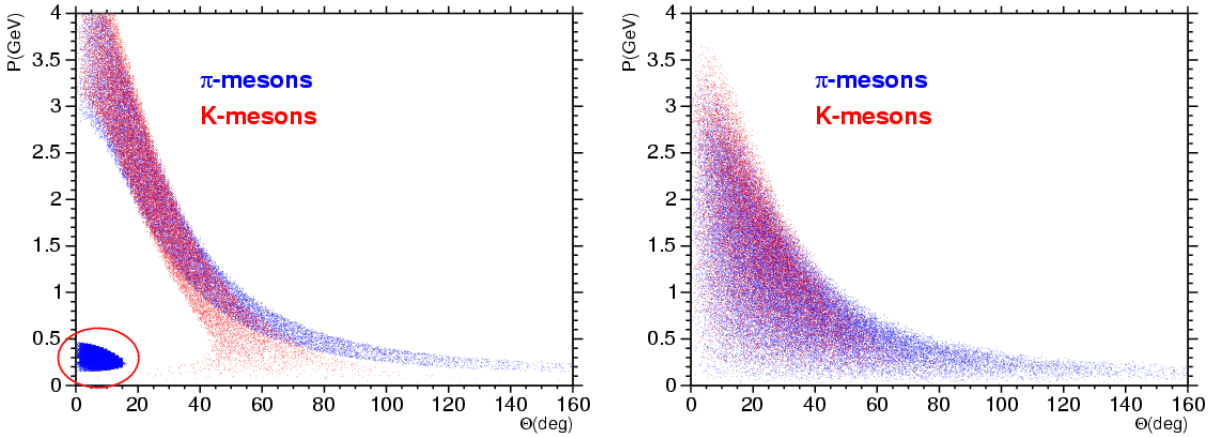

(a) distribution of muons (b) distribution of kaons

Figure 3.2: Momentum *vs.* polar angle distribution of kaons and pions from a) the reaction $\overline{\mathrm{p}}\mathrm{p} \rightarrow \psi(4040) \rightarrow D^{*+}D^{*-} \rightarrow D^0\pi^+D^0\pi^- \rightarrow K^-\pi^+\pi^+ + c.c.$ and b) the reaction $\overline{\mathrm{p}}\mathrm{p} \rightarrow \psi(3770) \rightarrow D^+D^- \rightarrow K^-\pi^+\pi^+ + c.c.$.

The unambiguous reconstruction of weakly decaying charmed hadrons necessitates the detection of a secondary vertex separated from the interaction point implying a track

impact parameter resolution of about 100 μm. A very good vertex detector is required which must be radiation hard along with low pileup from the high luminosity.

It will be very difficult, if not impossible, to obtain the high resolution at interaction rates of 10^7 /s already on the trigger level. For decays where a K_S^0 is produced as a decay particle, the decay can be selected on the first trigger level. In this way, more time is available for the analysis of the primary vertex on a higher trigger level. The selection of a specific decay channel by the trigger does not necessarily hinder the investigation of other decay modes because of the comparatively large probability of D meson pair production in $\overline{\mathrm{p}}\mathrm{p}$ annihilations at energies close to the threshold. A specific decay mode of one particle can be selected by the trigger without introducing a bias to the measurement of the other.

Good particle identification above particle momenta of 0.5 GeV/c is required at all angles. At momenta above 0.7–1.0 GeV/c π/K, the separation can be provided by Cherenkov counters. Analog readout of the silicon vertex or a time of flight detector could provide limited dE/dx information for particles below 0.7 GeV/c.

3.2.4 Charmed Hadrons in Nuclear Matter

Studies of the properties and interactions of hadrons with both hidden and open charm inside nuclei basically require the same detection capabilities as discussed related to the study of the charmonium spectrum and to searches for charmed hybrids or glueballs in the charm region. The final states involve either dilepton or photon detection in the case of hidden charm below the $D\overline{D}$ threshold or the identification of D mesons using the reconstruction of delayed vertices. However, a few peculiarities should be noted.

This part of the physics program involves nuclear targets which can be realized within the pellet or cluster jet target concept by using gases heavier than hydrogen, or by the implementation of solid wire or thin foil targets at the nominal interaction point, as discussed in Sec. **??**.

Due to the larger total $\overline{\mathrm{p}}$-nucleus cross section and to the increase of single and multiple scattering with increasing nuclear charge of the target, the maximum luminosity will have to be kept smaller in $\overline{\mathrm{p}}A$ collisions than in $\overline{\mathrm{p}}\mathrm{p}$ collisions. For instance, for $\overline{\mathrm{p}}\mathrm{Au}$ collisions, the increased interaction cross section has to be compensated by about a factor 25 reduced number density of target atoms per cm^2 in order to keep the interaction rate at a level of $2 \cdot 10^7$/s as defined by the $\overline{\mathrm{p}}$ production rate. However, the increased Coulomb scattering and, thus, shorter lifetime of the circulating $\overline{\mathrm{p}}$ beam, will further reduce the achievable luminosity. How large the further reduction by beam heating will be, depends on the details of the HESR parameters. Further careful studies of this aspect are needed.

In $\overline{\mathrm{p}}A$ collisions, it will generally not be possible to reconstruct the final state completely. This is a loss of kinematic constraints which are used in $\overline{\mathrm{p}}\mathrm{p}$ collisions to improve the mass resolution of reconstructed particles. In particular, it is not possible to use the precise information on the $\overline{\mathrm{p}}$ beam momentum, in order to determine the mass of a charmonium state in the formation reaction $\overline{\mathrm{p}}\mathrm{p} \rightarrow c\overline{c}$ if the target proton is bound in a nucleus and thus affected by the Fermi momentum. In this case, its mass must be determined by the detector, e.g. in $\mu^+\mu^-$ or $\gamma\gamma$ final states which puts more weight on the effort to achieve best possible values for the detector resolution. On the other hand, similar requirements

are posed by experimental studies of glueballs and charmed hybrids with exotic quantum numbers which are only observable in production reactions. A mass resolution of 1–2% is sufficient to distinguish between the established charmonium states, solely based on the information deduced from the detection system.

In $\overline{\mathrm{p}}A$ collisions, part of the final state particles of the $\overline{\mathrm{p}}N$ annihilation process - mostly pions - initiate an intra-nuclear cascade, which may produce secondary knock-on nucleons and thus may leave the residual nucleus in a highly excited state. The excited nucleus will further emit neutrons, protons and pions in a thermalization-like process, which can significantly increase expected radiation doses.

For specific $\overline{\mathrm{p}}$ momenta and target nuclei expected particle yields can only be estimated based on $\overline{\mathrm{p}}A$ event generators such as UrQMD [**?**, **?**] with an extension module for the nucleon evaporation. Details can be found in [**?**], in Computing chapter. An UrQMD simulation was carried out for $\overline{\mathrm{p}}$C, $\overline{\mathrm{p}}$Cu, and $\overline{\mathrm{p}}$Au collisions at 4.05 GeV/c $\overline{\mathrm{p}}$ momentum, corresponding to resonant J/ψ formation. The pion and nucleon multiplicities per collision are listed in Table 3.1. It shows that the pion multiplicity is expected to be almost independent of the size of the target nucleus whereas the predicted neutron and proton multiplicities, by far dominated by low energy evaporation processes, increase approximately according to $N^{0.9}$ for neutrons with the neutron number N, and according to $Z^{0.5}$ for protons with the proton number Z. Simulation shows that the neutron emitting source has essentially no forward boost and that the low energy neutron emission is almost isotropic. A similar emission pattern is predicted for the dominant low energy part of the emitted protons.

Target	N_n	N_p	N_π
^{12}C	2.3	2.6	6.6
^{63}Cu	9.3	7.0	6.4
^{197}Au	33.4	10.0	5.9

Table 3.1: Multiplicities per collision of neutrons N_n, protons N_p and pions N_π obtained in a UrQMD simulation of 10000 events for 4.05 GeV/c $\overline{\mathrm{p}}$ + ^{12}C, ^{63}Cu, and ^{197}Au. Particles from evaporation processes are included.

The yield of evaporation neutrons and protons in $\overline{\mathrm{p}}A$ collisions defines additional constraints on the required radiation hardness of detector components, depending on the achievable luminosity, and on the fraction of beam time spent on nuclear targets. This will be particularly relevant for the Micro Vertex Detector (MVD) but may also be of concern for other subdetectors, e.g. the Electromagnetic Calorimeter (EMC). A 1 year duration run of $\overline{\mathrm{p}}$Cu at maximum luminosity $L = 1.4 \cdot 10^{31}\,\mathrm{cm}^{-2}\mathrm{s}^{-1}$ (corresponding to 10^7/s interaction rate) and an overall duty cycle corresponding to a net 100 day run at maximum luminosity is considered in order to illustrate the expected order of magnitude in neutron irradiation. From the UrQMD simulation, a total number of $8 \cdot 10^{14}$ neutrons is expected for a 1 year run. Assuming isotropic emission, this corresponds to $3 \cdot 10^{13}$ neutrons per cm^2 at 1.5 cm distance from the interaction point (about the closest distance to the first MVD layer) and $2.5 \cdot 10^{10}$ neutrons per cm^2 at 50 cm distance (about the closest distance to the inner EMC surface). For heavier targets, like Au, the increase

of the neutron multiplicity per collision is expected to be compensated by the reduced maximum luminosity which is limited by the shorter $\overline{\mathrm{p}}$ lifetime due to the higher beam heating effect.

3.2.5 Production of multistrange systems

The simultaneous production and implementation of two Λ particles into a nucleus is not feasible. Because of that the conversion of a Ξ^- and a proton into two Λ particles will be used, which releases only $\tilde{2}8\,\mathrm{MeV}$ of excitation energy. Accordingly, there is a chance of typically a few percent that both Λ hyperons stick to the same nucleus [**?**, **?**, **?**]. Ξ^- hyperons produced in reactions with *stable* hadron beams typically have rather high momenta. Therefore, capture of the Ξ^- in the nucleus is rather unlikely. The capture of Ξ hyperons has to proceed in two (or even three) steps. Using energetic hadron beams, a Ξ^- (together with its associated strange particles) is produced in a primary target. In a second step, the Ξ^- is slowed down in a dense, solid material (e.g. a nuclear emulsion) and forms a Ξ^- atom [**?**]. After an atomic cascade, the hyperon is finally captured by a secondary target nucleus. It is mandatory to keep the primary momentum of the produced Ξ^- as low as possible in order to reach a high capture probability. If the momentum of the hyperon is too high its stopping time will exceed the lifetime and hence the Ξ^- will decay prior to the atomic capture with high probability.

Using the (K^+, K^-) double strangeness exchange reaction, Ξ^- hyperons are produced with typical momenta of $500\,\mathrm{MeV}/c$ [**?**, **?**]. Most ($\sim 80\,\%$) hyperons escape from the target nucleus. However, for a few percent of the reactions the Ξ is captured in the nucleus. The advantage of this production process is that the outgoing K^- can be used as a tag for the reaction. A drawback is the low kaon beam intensity because of the short kaon lifetime and hence the need for thick primary targets.

The $\overline{\Xi}^+$ was discovered in antiproton-proton interactions at $3\,\mathrm{GeV}/c$ [**?**, **?**]. Relatively low momentum Ξ^- can be produced in $\overline{\mathrm{p}} + \mathrm{p} \rightarrow \Xi^-\overline{\Xi}^+$ or $\overline{\mathrm{p}} + \mathrm{n} \rightarrow \Xi^-\overline{\Xi}^\circ$ reactions as will be outlined below. The advantage as compared to the kaon induced reaction is the fact that the antiproton is stable and can be retained in a storage ring. This allows a rather high luminosity even with very thin primary targets. The associated $\overline{\Xi}$ will undergo scattering or (in most cases) annihilation inside the residual nucleus. Strangeness is conserved in the strong interaction and the annihilation products contain at least two anti-kaons that can be used as a tag for the reaction (see Fig. 3.3).

Because of the two-step process, spectroscopic studies, based on the analysis of two-body reactions like in single hypernuclei reactions, cannot be performed Spectroscopic information on double hypernuclei can only be obtained via their decay. We can distinguish two different steps of the decay process:

1. γ-rays emitted via the sequential decay of an excited double hypernucleus will provide information on the level structure with rather high resolution.

2. Once the ground-state is reached, the weak decay of the hyperon(s) will initiate the emission of several particles. Here, the determination of the ground-state mass requires the knowledge of all masses of the various decay products and their kinetic

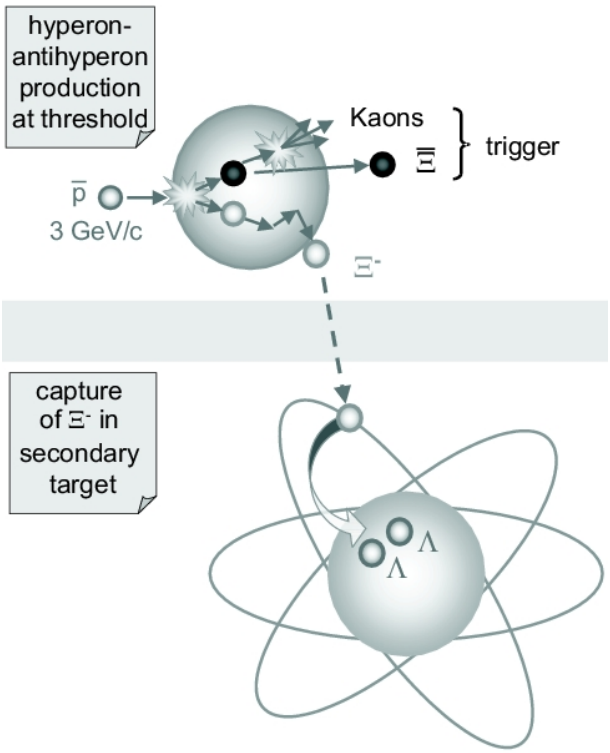

Figure 3.3: Double hypernucleus production. The antiproton beam enters from the left.

energies. Hence, unique identification of the final particles and precise determination of their kinetic energies is mandatory. Nuclear emulsions are the only technique which meets all requirements for these measurements of ground-state masses. However, it is impossible to detect neutrons or γ-rays from intermediate, particle-unstable fragments with this method. As a consequence, the determination of the ground-state mass of double hypernuclei is limited to light nuclei which decay exclusively into charged particles.

3. Finally, the kinetic energies of weak decay products are sensitive to the binding energies of the two Λ hyperons.

Because of the need for a fully electronic detection system, the spectroscopic information on double hypernuclei will be obtained via (i) and (iii) at $\overline{\mathsf{P}}$ANDA. High-efficiency Germanium arrays can be used for high resolution γ-ray spectroscopy. In combination with the high luminosity at HESR and with a novel solid-state micro-tracker, high resolution γ-ray spectroscopy of double hypernuclei and Ω atoms will become possible for the first time.

For the measurements of double hypernuclei and Ω atoms, the backward part of the calorimetric detector will be removed to place a nuclear target directly in front of the main tracking detectors. In order to minimize the background from associated particles, the production of hypernuclei and hyperatoms will use $\Xi\overline{\Xi}$ and $\Omega\overline{\Omega}$ pair production close to threshold in antiproton nucleus collisions. The trigger will be based on the detection

of high momentum anti-hyperons at small axial angles or – in most cases – of positive kaons produced by the anti-hyperons absorbed in the primary target. The $2K^+$ trigger will provide significantly higher count rates but requires the detection of kaons with a rather low momentum of a few hundred MeV/c. The second element of the experiment is the deceleration and subsequent absorption of the Ξ^- hyperons in a secondary active target. As a third element, an efficient Germanium γ-array is required. This array will be mounted at backward polar angles outside the super-conducting solenoid.

3.3 Detector structure

To achieve these goals, the detector is split up into two spectrometers. A target spectrometer (TS) surrounds the interaction region and a forward spectrometer (FS) with a second magnet provides angular coverage for the most-forward angles. The basic concept of the target spectrometer is a shell-like arrangement of various detector systems surrounding the interaction point inside the field of a large solenoid. The forward spectrometer will overcome also the gap in acceptance and resolution in the forward region of such a system. The use of a large-gap dipole magnet in combination with tracking detectors and calorimeters is likely to be an optimal solution. However, other concepts, like a toroid, are still under evaluation. Both parts, the target spectrometer (TS) and the forward spectrometer (FS), will allow the detection, identification, and energy/momentum reconstruction for both charged and neutral particles. The combination of two spectrometers takes into account the wide range of energies; and it still has sufficient flexibility, such that individual components can be exchanged or added for specific experiments, e.g. for the experiments with hypernuclei or for the special needs of $\mathcal{CP}$ violation studies.

Conceptual design of the detector is shown in several views in Fig. 3.4. The anti-proton beam will interact with the target at the cross point with the target mandrel, which is located inside the solenoid.[1] Particles emitted with laboratory polar angles larger than 10° are measured solely in the target spectrometer. Surrounding the interaction volume there will be a silicon micro-vertex detector (MVD) including a barrel of five layers around the interaction region and wheel part in forward. Starting from a radial distance of 15 cm from the beam line up to 42 cm a second tracking detector will be situated. It will either consist of 15 double layers of straw tubes (STT) or a time projection chamber (TPC). At a radial distance of 45 cm particle identification with a ring-imaging Cherenkov (RICH) counter realized by the detection of internally reflected Cherenkov light (DIRC) detector follows. The forward region will be covered by two sets of mini drift chambers (MDC) and another Cherenkov detector, either an aerogel RICH or a flat DIRC. The inner detectors are surrounded by an electromagnetic calorimeter (EMC) consisting of about 19 000 crystals that are read out with avalanche photo-diodes. All these detectors are contained within the coils of a solenoid providing a homogeneous magnetic field in that region. Outside of the return yoke scintillating bars for muon identification (MUO) will be mounted.

[1] A solid target for the studies on hypernuclei will be located together with a modified end cap on a more up-stream position.

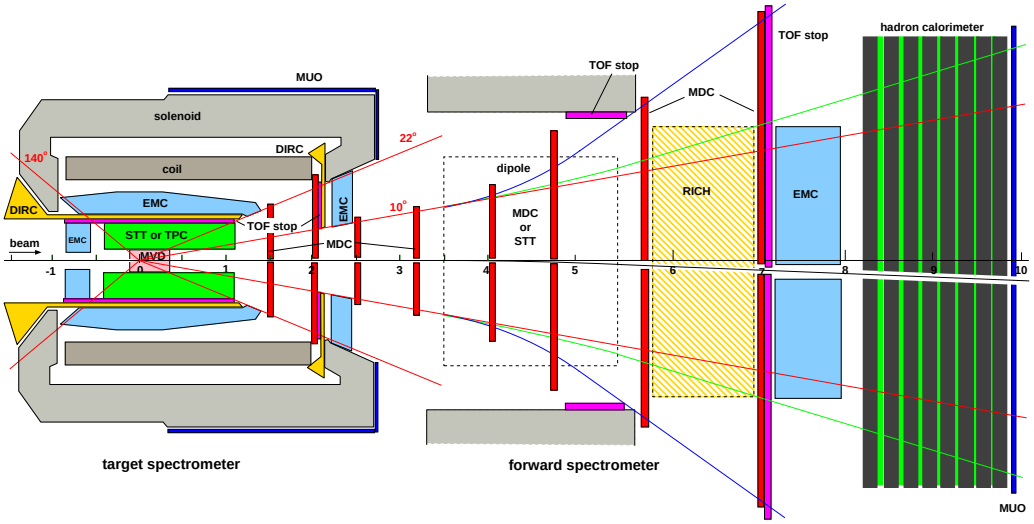

(a) top view: green and blue lines indicate outermost tracks of charged particles with factors 3 and 15 reduced momenta respectively (compared to the beam – black)

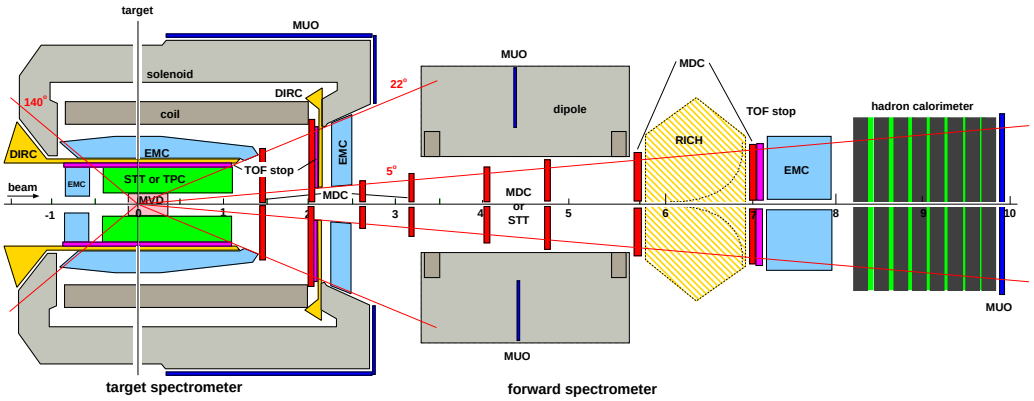

(b) side view: the HESR beam follows the scale axis

Figure 3.4: Sketches of the detector viewed from the top and the side in (a) and (b) respectively. The HESR beam enters the detector from the left; it interacts with the target a 0 m on the horizontal scale. The surrounding and forward covering detectors are indicated: micro-vertex detector (MVD – rosé), straw-tube tracker (STT) or time-projection chamber (TPC) (light green), time-of-flight stop counters (TOF stop – pink), Cherenkov detectors (DIRC and RICH – yellow), electro-magnetic calorimeter (EMC – light blue), mini-drift chambers (MDC – red), hadron calorimeter, and muon counters (MUO – dark blue)

Particles emitted with polar angles below 10° in the horizontal and 5° in vertical direction, are measured with the help of the forward-spectrometer (FS). The current design includes a 1 m gap dipole and tracking detectors to momentum analyse charged particles, i.e. mini drift chambers (MDC) and straw-tube trackers. Photons will be detected by a Shashlyk-type calorimeter consisting of lead-scintillator sandwiches (EMC). Other neutrals and

charged particles with momenta close to the beam momentum will be measured in the hadron calorimeter, and muon counters (MUO).

It is currently under investigation, weather an additional RICH detector, like at Hermes, and time-of-flight measurements will be required for event reconstruction. The latter would include fast start detectors close to the target, and time-of-flight stop counters (TOF stop) placed suitably inside the target and forward spectrometers.

Short description of the $\overline{\text{P}}$ANDA detector is given below, for more details please see [1].

3.3.1 Target Spectrometer

The target spectrometer (TS) contains the azimuthally symmetric system of detectors mostly contained inside the coils of the superconducting solenoid. Also attributed to this part are the muon counters on the outside of the magnet return joke, and the forward end cap which may be situated just behind the magnet (see Figs. 3.4 and 3D view of the inner part in Fig. 3.5). This part of $\overline{\text{P}}$ANDA will detect all particles, which are emitted with laboratory angles greater than 5° in vertical and 10° in horizontal directions. For the more forward directed particles tracking and possibly also a time-of-flight start signal will be obtained using the MVD and MDCs.

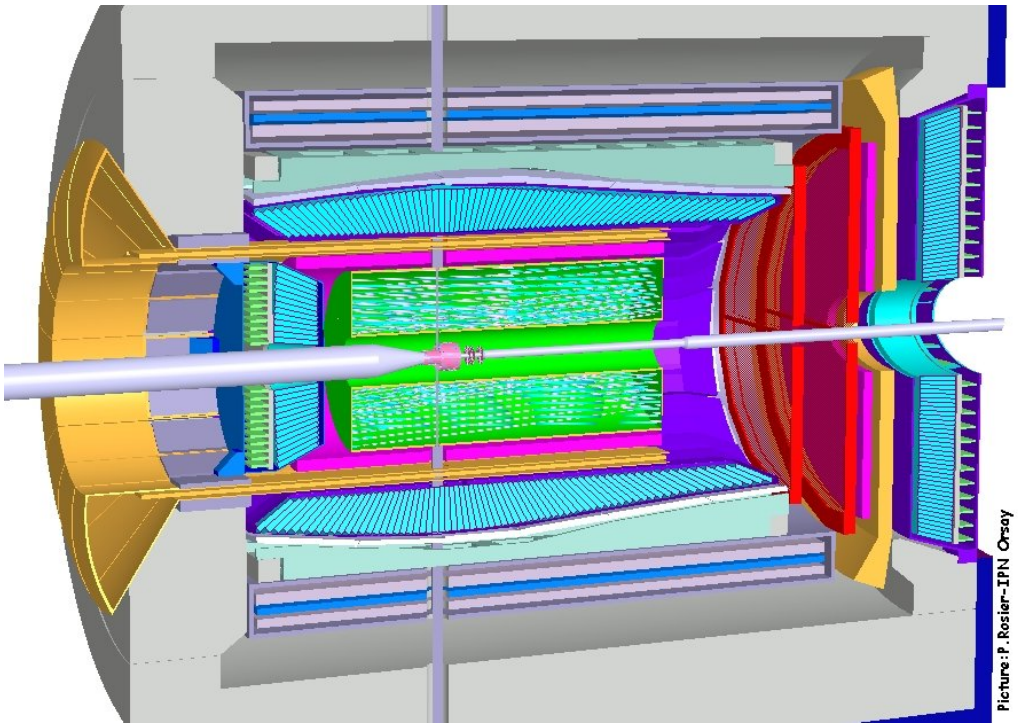

Figure 3.5: View of the detectors inside the target spectrometer

3.3.1.1 Target System

The compact design of the detector nested inside the solenoid leaves minimal space for a target inside the detector. Luminosity can be calculated as follow:

$$L = f_{rev}\frac{N}{A}\langle N_t\rangle_A, \tag{3.1}$$

where f_{rev} is beam revolution frequency, N is the number of antiprotons in the beam, N_t is density of the target material and A - atomic number of the target material. In order to reach the design luminosity of $2 \cdot 10^{32}/\mathrm{cm}^2\mathrm{s}$ and given a stored number of 10^{11} antiprotons in the HESR ring, a target thickness - $\langle N_t\rangle_A/A$ - of about $4{\cdot}10^{15}$ hydrogen atoms per cm^2 is required. These are the conditions which pose a challenge to the development of a suitable target.

Recent years have, however, seen substantial progress by the development of cluster-jet targets and pellet targets, which consist of a stream of frozen droplets [2]. These two options are currently under consideration for the $\overline{\mathrm{P}}$ANDA hydrogen target, but also heavier gases, like deuterium, nitrogen and argon, can be used without problems. Both approaches have their particular advantages and disadvantages, which are currently under an investigation. None of these studies could yet prove any target to be clearly superior. Thus the studies have to be continued leading to a decision on which target will be used in the final set-up. Nevertheless, the geometrical limitations which the target poses to the detectors can be specified for both solutions. Thus the design of the adjacent detectors can be based on these boundary conditions, especially the MVD design. It should be noted, that for the charmonium and the open charm physics, where a clear separation between the primary and secondary vertices is required, the pellet target is preferable.

The situation is somewhat different for a solid target to be used for hypernuclear studies in conjunction with a modified $\overline{\mathrm{P}}$ANDA end cap. This target will be mounted in front of the MVD and housed within the dedicated detector set-up for those experiments.

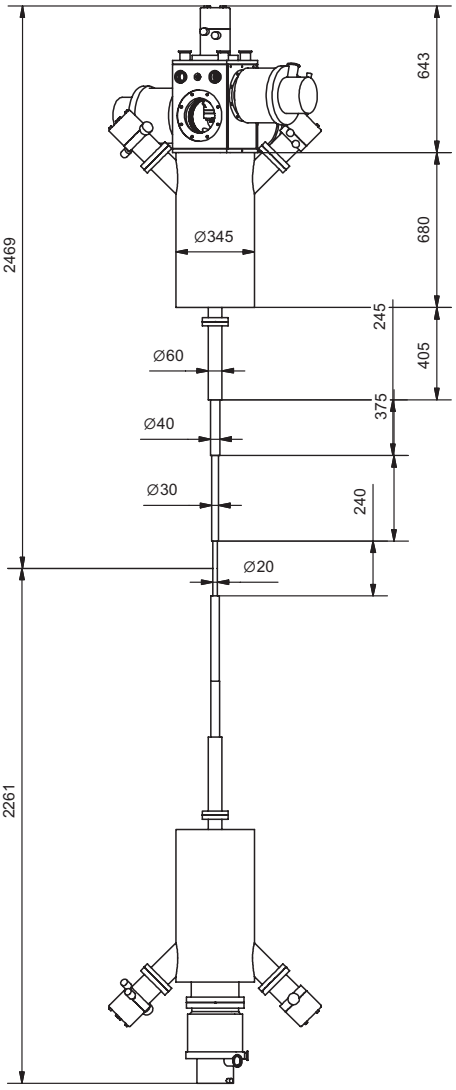

Figure 3.6: A technical drawing of the target vacuum system inside the $\overline{\mathrm{P}}$ANDA detector. The dimensions of the vacuum pipes meet the requirements for a cluster-jet target as well as a pellet target solution. In case only the cluster target solution, the diameter of the innermost part of the vacuum system can be narrowed down from 20 mm. to 6mm.

A Pellet Target (Fig. 3.6) consists of a stream of frozen hydrogen micro-spheres, called pellets, traversing the anti-proton beam perpendicularly. The design will be based on the pellet target placed inside the $4\,\pi$ WASA detector at the CELSIUS storage ring [2, 3, 4]. At the interaction point, typical parameters are a pellet rate of 10–15 kHz, a fall speed

$\gtrsim$ 60 m/s and a pellet size of 25 μm, which together imply a target thickness of a few 10^{15} atoms/cm^2. This corresponds well to the envisaged target thickness at $\overline{\mathsf{P}}$ANDA. However, due to the angular divergence of the pellets of $\sigma = 1.0$ mm, the area, which should be covered by the antiproton beam, has to be similar in size. Since a single pellet undergoes about 100 interactions during the time it traverses the beam, it will be no difficulty to determine the position of individual pellets with the necessary accuracy not only in transverse but also longitudinal direction. For $\overline{\mathsf{P}}$ANDA, the present pellet rate and train divergence at the WASA pellet target needs to be improved by factors of 2 or below. The ongoing further development of the target at a dedicated test area at TSL is expected to improve the present performance by those factors at least. In addition to the production of deuterium pellets, which is well established by now, the use of other gases as target material poses no problem.

Cluster-Jet Target is shown on Fig. 3.6. To fulfill the demand on target thickness with a cluster-jet target requires a density increase of one order of magnitude compared to what has presently been achieved. In addition, due to detector constraints, the distance between the cluster-jet nozzle and the target has to be increased compared to previous applications. The size of the target region will be given by the lateral spread of hydrogen clusters, which, when optimized, should stay less than 10 mm. The great advantage of cluster targets is the homogeneous density profile and the possibility to focus the antiproton beam at highest phase space density. Hence the interaction point is defined transversely but has to be reconstructed longitudinally in beam direction. The possibility to adjust the target density along with the gradual consumption of antiprotons for running at constant luminosity is an advantage while the badly defined interaction-point is a problem for any open-charm measurement. Internal cluster targets can run with other gases as well. So not only hydrogen but also nuclear targets will be provided by this target technique.

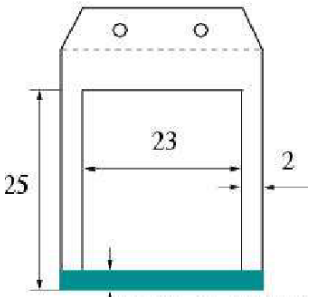

Figure 3.7: Mounting of the wire target on a fork structure, as done at COSY. Dimensions are in mm.

Thin fibre target (Fig. 3.7), mechanically integrated in the pellet or jet target arrangement, is considered as a target for studying of the in-medium modification of charmonium and open charm mesons. The fibre can be made from a polypropylene (CH_2), carbon or heavy metals, like gold.

Target for the hypernuclear physic is under consideration. Presumably it will be a separate target station beam upstreams, which comprise primary and secondary target and detectors.

3.3.1.2 Micro-Vertex Detector

The design of the micro-vertex detector (MVD, see Fig. 3.8) for the target spectrometer at HESR is optimized for the detection of secondary vertices and maximum acceptance close to the interaction point. It will also strongly improve the transverse momentum

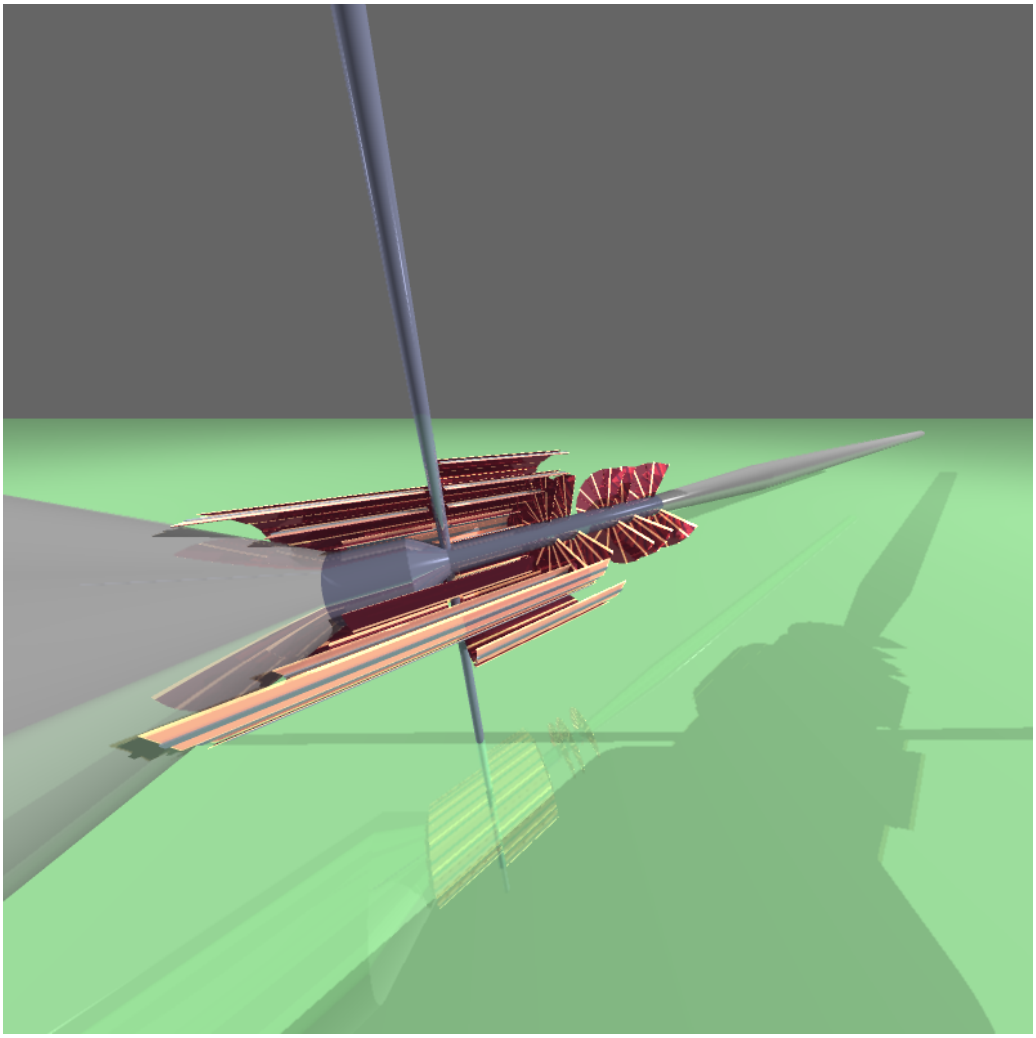

Figure 3.8: Artistic 3D-view of the MVD. One quarter of the detector is removed to show an internal structure.

resolution. In addition a layer of diamond or silicon detectors may provide a start signal for time of flight detectors.

The concept of the MVD is based on radiation hard silicon pixel detectors with fast individual pixel readout circuits and silicon strip detectors. The layout foresees a five layer barrel detector with an inner radius of $\gtrsim$1 cm and an outer radius of 6 cm. The three innermost layers will most likely consist of pixel detectors, while the outer 2 layers are now considered to consist of silicon strip detectors.

Five detector wheels arranged perpendicular to the beam will give best acceptance for the forward part of the particle spectrum. Here again at least the two last layers will be striped detectors, while the target nearest layers will consist of pixel detectors.

All detector wafers are 200 μm thick ($0.25\%\, X_0$). The readout via bump-bonded wafers with ASICs as it is used in ATLAS and CMS [5, 6] is foreseen as the default solution. It is highly parallelized and allows zero suppression as well as the transfer of analog information

at the same time. The readout wafer has a thickness of 300 μm (0.37% X_0). An alternative readout scheme is presently in development for future high energy experiments and has already been used in X-ray astronomy [7]. Active pixels contain the charged particle sensitive part on one side and implement each pixel's readout circuit on the other side of the same silicon wafer. The clear advantage is that only half of the material thickness has to be used for the same detection capability, which reduces multiple scattering and secondary interactions. Detailed description of the MVD is given in the Sec. **??**.

3.3.1.3 Outer Tracking Detectors

The charged-particle tracking devices must handle the high particle fluxes that are anticipated for luminosities of up to $2{\cdot}10^{32}\,\mathrm{cm}^{-2}\mathrm{s}^{-1}$. The momentum resolution $\delta p/p$ should typically be on the percent level and the detectors should have a good detection efficiency for secondary vertices which can also occur outside the inner vertex detector (e.g. K^0_S or Λ). This is achieved by the combination of the silicon vertex detectors close to the interaction point (MVD) with a two outer systems. One system is covering the large area and designed as a barrel around the MVD. This will be either a stack of straw tubes (STT) or a time-projection chamber (TPC). The small angles will be covered using two sets of cylindrical 8 (or 6) layer mini-drift chambers (MDC), similar to those developed for the Hades experiment at SIS18.

Straw Tube Tracker (STT) see Fig. 3.9 In total there are 15 double-layers[2] of straws at radial distances between 15 cm and 42 cm to the beam and their overall length is 150 cm. The first and last double-layers are arranged parallel to the beam axis, and the remaining 13 double layers are arranged at skew angles ranging from 4.5° to 9°. The skew angles cause the stereo layers to form a hyperboloidal shape and allow to determine the position of the particles along the beam direction to about 1 mm. In order to remove the left-right ambiguity the straws are assembled in double-layers which are packed into supports of Al-Be semi-rings. The straws have diameters ranging from 4 mm (innermost) to 8 mm (outermost). The tube wall will have a thickness of about 30 μm (aluminized mylar, or carbon loaded Kapton). As sense wires 20 μm thick gold plated tungsten wires are foreseen. The amount of material could be minimized by self-supporting tubes held by a light Al-Be mechanical frame. The gas mixture used will be Argon based with CO_2 as quencher. We foresee to have a gas gain not greater than 10^5 in order to guarantee long term operation. With these parameters, we expect a resolution in x and y coordinates of about 150 μm.

A Time Projection Chamber (TPC) [8] (Fig. 3.9) is a challenging but interesting alternative to a STT. It consists of one (or maybe two) large gas-filled cylindrical volume(s) surrounding the MVD like a barrel. An electric field along the cylinder axis separates positive gas ions from electrons created by ionizing particles traversing the gas volume. At the end cap avalanche amplification occurs typically in multi-wire proportional chambers,

[2] exact parameters of the STT is under investigation. For more information see Sec. 4.2

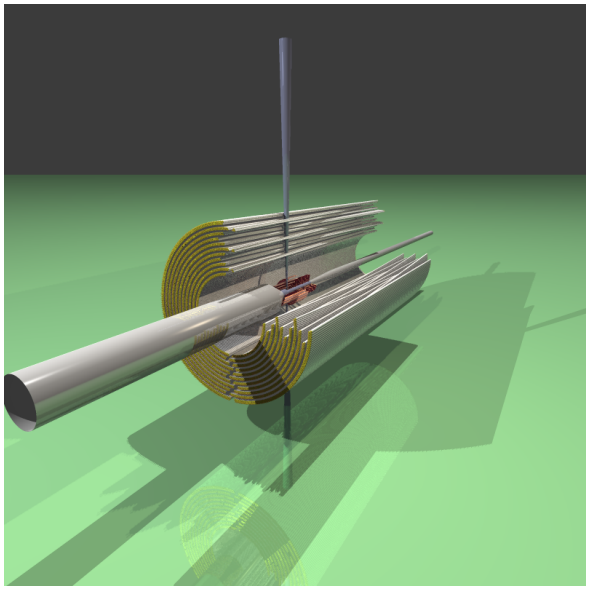

Figure 3.9: Artistic 3D-view of the STT. One quarter of the detector is removed to show an internal structure. The MVD is also shown inside of the STT.

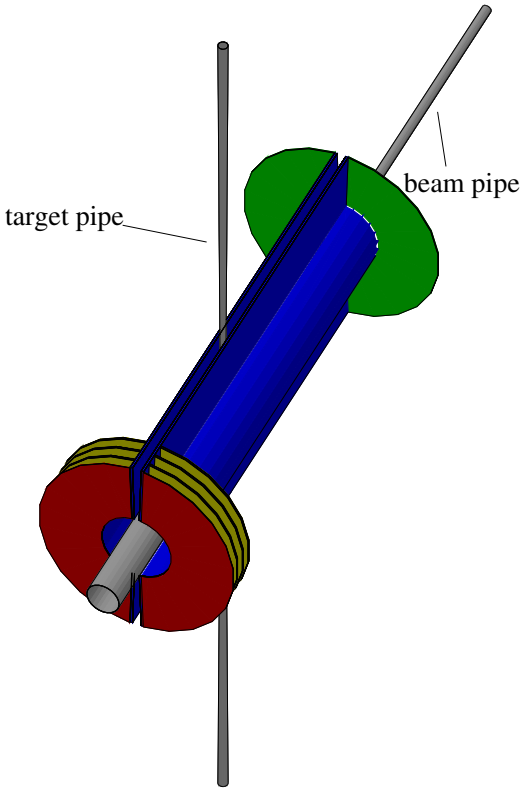

Figure 3.10: 3D view of the two halves of the TPC, together with the beam and target pipes. The outer shell of the TPC is removed to show an internal structure.

yielding information on two coordinates. The third coordinate of the track comes from a measurement of the drift time of each primary electron cluster.

In contrast to previous set-ups [9, 10] the TPC planned for $\overline{\mathsf{P}}$ANDA has to operate in continuous mode and with a granularity increased by an order of magnitude. A novel method to achieve gas amplification using the Gas Electron Multiplier (GEM) [11] recently invented at CERN, provides features which seem to make this kind of improvement feasible.

Multi-wire Drift Chambers (MDC, see Fig. 3.11) [1] Particles emitted at angles below 22° which are not covered fully by the Straw Tube Tracker will be tracked with two multi-wire drift chambers (MDC) placed 1.4 m and 2.0 m downstream of the target. The chambers have to stand a high counting rate of particles peaked at the most forward angles due to the relativistic boost of the reaction products as well as due to the small angle $\overline{\mathrm{p}}p$ elastic scattering. With the envisaged luminosity the expected particle flux in the first chamber in the vicinity of the 5 cm diameter beam pipe is about $3{\cdot}10^4\,\mathrm{cm}^{-2}\mathrm{s}^{-1}$. Besides, the chambers have to work in the 2 T magnetic field produced by the $\overline{\mathsf{P}}$ANDA-solenoid.

In order to fulfill these requirements quadratic drift cells with an area of $1\,\mathrm{cm}^2$ were chosen. Each chamber will contain several pairs of detection planes. The number of pairs

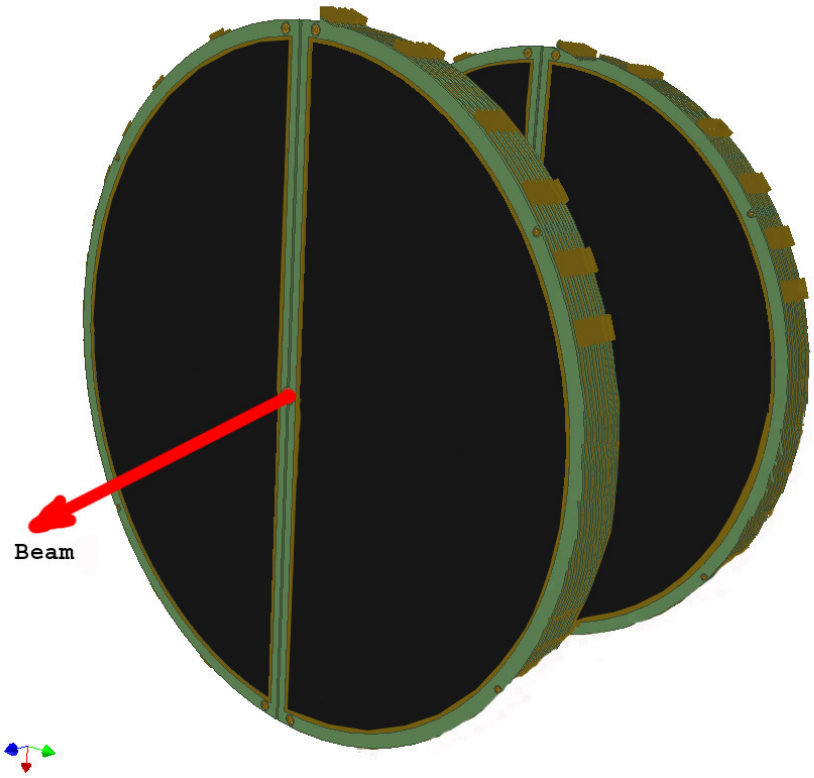

Figure 3.11: 3D-view of the MDCs.

and their orientation will depend on usage or not of insulating rings for mounting the most central wires coming at the position of the beam-pipe. The planes in each pair will be staggered by half of the cell width in order to resolve the "left-right" ambiguity. The wires will be mounted on frames of octagonal shape.

Possibility of using frames having a form of a closed semi-circle have also been explored. The detection planes would consist of pairs of such frames put together along the common diameter. These frames could be mounted and dismounted without necessity of removing the beam-pipe.

3.3.1.4 Particle Identification

Particle identification for hadrons and leptons over a large range of solid angle and momenta is an essential requirement for meeting the physics objectives at the HESR. There will be several dedicated systems which, in complement with the other detectors, will provide means to identify particles. A time-of-flight TOF system will include TOF start detectors in the MVD, a TOF barrel between STT/TPC and DIRC, a part in the forward end cap, and a large TOF stop wall in the forward spectrometer (FS). Detectors of Cherenkov Light will enlarge the capabilities of this system to the high momenta, where flight times are too short. Moreover, in certain ranges particle identification will be done by using energy losses in the detectors (MVD for slow charged particles, dE/dX informa-

tion from TPC, EMC for γ-rays and leptons). Of course, tracking in the magnetic field is a crucial ingredient, and in many cases only the combination of information from many detectors can provide a particle identification.

Time-of-Flight (TOF) Stop counters will provide a stop signal to measure the time a particle has used to travel a certain distance, i.e. its velocity. This relies on a fast start counter close to the interaction point and tracking detectors to define the flight path. In conjunction with the momentum, determined by tracking in the magnetic field, masses and hence particle identification can be defined. This is possible as long as the particles don't become too fast in comparison to the timing resolution achievable. Moreover, at the relativistic limit particles can't be identified by their speed in principle. Nevertheless, the system may be important to fill the gap between particles which can be identified *via* energy losses and the ones distinguishable with Cherenkov detectors.

The R&D is still going on and a project with the goal to produce low mass scintillation counters with high timing resolution has been started [12]. It is aimed for masses below $0.5\%X_0$ and timing resolutions of $\sigma \leq 200\,\text{ps}$. The detectors will cover angles between 22° and 140° using a barrel arrangement around the STT/TPC (about 48 cm radial distance). Another flat layer of detectors will cover the angles between 5/10° and 22° in the forward end cap. Simulations will still show, weather the should be located before or after the Cherenkov detectors.

Detectors of Cherenkov Light will be used at two different positions within the the target spectrometer. Charged particles in a medium with index of refraction n, propagating with velocity $\beta c < 1/n$, emit radiation at an angle $\Theta_C = \arccos(1/n\beta)$. Thus, the mass of the detected particle can be determined by combining the velocity information determined from Θ_C with momentum information from the tracking detectors. Due to the strong variation of the typical particle momentum with polar angle, the particle identification can be achieved using two systems of Cherenkov detectors in the target spectrometer.

At polar angles between 22° and 140°, particle identification will be performed by the detection of internally reflected Cherenkov (DIRC) light as realized in the BaBar detector [13]. It will consists of 1.7 cm thick quartz slabs ($n = 1.544$) surrounding the beam line at a radial distance of 48 cm. The main costs of the BaBar setup arise from the 11 000 photo-multiplier tubes, which allow timing information to be used to suppress the large background resulting from the electron beam environment. At $\overline{\text{P}}$ANDA, these costs could be reduced by employing by employing new optical readout schemes e.g. with APD arrays or by replacing one of the two space dimensions for the Cherenkov rings by the timing information (see [1] for details) in the previous detector shell.

Another Cherenkov detector will be located in the end cap of the TS between polar angles of 5° and 22°. It will either be a flat DIRC disk or a Aerogel Cherenkov Counter (RICH) and will provide particle identification and information for higher-level triggers. RICH detectors with a refractive index of $n = 1.02$ are especially suited for π-K separation. The optical transmission (re-scattering) of the radiator material limits the thickness of the blocks to about 4 cm. The measurement of the light cones by exploiting proximity

focusing at 10 cm from the exit of the radiator with multi-pad gas detectors allows a compact construction without mirrors and Photo-multiplier-tubes. With such a geometry photons from asymptotic particles are found on rings of 24±4 mm radius. The concept of an aerogel RICH is included in the LHCb detector, and the high quality aerogel is already being used by the Belle collaboration [14].

Muon Detection (MUO) in $\overline{\text{P}}$ANDA is a delicate task due to both the very low cross section of the interesting channels compared to muons from the decay of pions which are abundantly produced in $\overline{\text{p}}$p annihilation.

Behind the iron yoke of the TS, plastic scintillator counters for muon detection will be installed that cover the laboratory polar angular range from 80° down to the opening for the dipole. Coverage to larger polar angles is not needed since the muons will be stopped in the iron yoke. The momentum of those muons is determined by the TS-tracking. The TS-MUD system will consist of about 96 individual bars that are 10 cm wide, 1 cm thick and about 2 m long. In addition there is an equal number of bars perpendicular to the beam axis, at the front of the TS-solenoid. The bars are read out with photo-multipliers fed to ADCs and TDCs. This information can be used to determine the position for matching with the TS-tracking, and the time of flight, to suppress random coincidences. The energy information provides not only a redundant position information, but also a value of $\mathrm{d}E/\mathrm{d}x$ to permit further background suppression.

3.3.1.5 Electromagnetic Calorimeter

Expected high count rates and a geometrically compact design of the target spectrometer require a fast scintillator material with a short radiation length and Molière radius for the construction of the electromagnetic calorimeter (EMC). In recent years $PbWO_4$ has been proposed and confirmed as a high density inorganic scintillator with sufficient energy and time resolution for photon, electron and hadron detection even at intermediate energies [15, 16, 17]. For high energy physics $PbWO_4$ has been chosen by the CMS and ALICE collaborations at CERN [18, 19] and optimized for large scale production. Besides a short decay time of less than 10 ns good radiation hardness has been achieved [20]. Recent developments indicate a significant increase of light yield due to crystal perfection and appropriate doping to enable photon detection down to 10 MeV with sufficient resolution. Optional cooling down to -25°C can further increase the light yield by a factor 3–4 compared to room temperature operation. There is, however, R&D performed to verify that these parameters can in fact be reached. This is essential for the identification and reconstruction of events with multiple photons in the final state. Thus the use of BGO or other crystal materials is still considered and studies with these materials are performed in parallel. It is proposed to use crystals of approximately $20\,X_0$ in length achieving an energy resolution below 2 % at 1 GeV [15, 16, 17] at a tolerable energy loss due to longitudinal leakage of the shower. These crystals allow π-e discrimination of 10^3 for momenta above 0.5 GeV/c. Therefore, particle identification does not rely on an additional gas Cherenkov detector in favor of a very compact geometry. Tapered crystals with a front size of $2.2 \times 2.2\,\mathrm{cm}^2$ mounted with an inner radius of 50 cm will be used. This implies 11360 crystals for the barrel part of the calorimeter. The backward and forward end caps

will comprise additional 7680 modules. The readout of the crystals will be accomplished by large area avalanche photo diodes with optimized light collection, a tolerable nuclear counter effect and a fast timing information. In greater details construction of EMC is described in [1]

3.3.1.6 Solenoid Magnet

The target solenoid consists of a superconducting coil with an inner radius of 90 cm and a length of 2.8 m. The maximum magnetic field is 2 T. The field homogeneity is better than a few percent over the volume of the inner and outer tracker. In order to minimize the amount of material in front of the EMC, the latter is placed inside the magnetic coil. The bending power downstream of the target allows a reasonable momentum resolution even at the smallest polar angles (5°/10°) detected only in the solenoid. This minimum angle of the solenoid acceptance is small enough to allow the dipole magnet to maintain a 1 m gap height. The cryostat for the coils has two warm bores of 100 mm diameter one on top and the other on bottom of the target position to allow for insertion of internal targets.

3.3.1.7 Germanium Detectors

The hypernuclei study will make use of the modular structure of $\overline{\mathsf{P}}$ANDA. Removing the upstream part of the calorimeter will enable us to add a second nuclear target station and the required additional detectors for γ spectroscopy close to the entrance of $\overline{\mathsf{P}}$ANDA. The hypernuclear measurements will comprise three basic components:

Detection of anti-hyperons and low momentum K^+ in the forward region. While the anti-hyperons will be detected with the universal detector, the kaon detection requires a time of flight measurement because of the low momenta of the kaons.

A compact high resolution solid state tracker for absorption and tracking of low momentum hyperons at large angles. The geometry of this secondary target is determined by the short mean life of the Ξ^- of only 0.164 ns. This limits the required thickness of the active secondary target to about 25–30 mm. It will consist out of a compact sandwich structure of micro strip detectors (as used for the MVD) and absorbing material.

High resolution and highly efficient germanium-array for γ-ray detection. The large volume germanium-arrays presently under construction at GSI [21]. The main limitation will be the load due to neutral or charged particles traversing the germanium detectors. Therefore, currently readout schemes and tracking algorithms are under development, which will enable high resolution γ-spectroscopy in an environment of high particle flux .

3.3.2 Forward Spectrometer

The down-stream part of the detector is named forward spectrometer (FS), and is dedicated for the detection of all particles emitted under laboratory angles below 5° and 10° in vertical and horizontal direction respectively. In the current design charged particles will be analysed using a 2 Tm dipole magnet. Neutral and very fast particles will be detected in the forward calorimeters. It is shown as sketches in Figs. 3.4 and in a 3D view in Fig. 3.12.

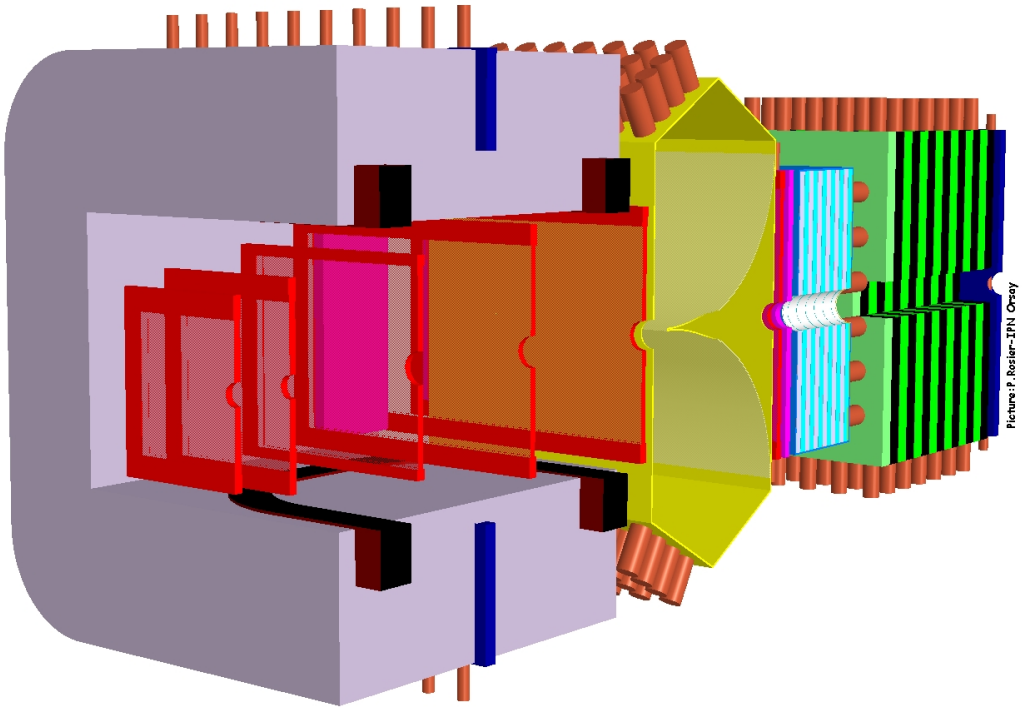

Figure 3.12: View of the forward spectrometer.

3.3.2.1 Dipole Magnet

A dipole magnet of window frame type with 1 m gap and more than 2 m aperture will be used for the momentum analysis of charged particles in the forward spectrometer (FS). In the current planning the magnet yoke will occupy the space between about 3.3 m and 5.8 m downstream of the target. Thus it covers the hole in angular acceptance of the TS to ±10° and ±5° in the horizontal and in the vertical direction respectively. The maximum bending power of the magnet will be 2 Tm and the resulting deflection of the antiproton beam at the maximum momentum of 15 GeV/c will be 2.2°. For charged particles the acceptance is designed such, that a factor of 10 or 15 in momentum range can be covered with the detectors beam downstream of the magnet. For particles with lower momenta detectors will be placed inside the iron yoke, which itself can be instrumented with detectors for ionizing particles. This option will become important for maximizing the muon detection efficiency. The beam deflection will be compensated by two or three

correcting dipole magnets — all of them placed downstream of the $\overline{\mathsf{P}}$ANDA detection system. This is a very nice solution, but field calculations show that the magnetic field turns out to be strongly inhomogeneous between the solenoid and the dipole. Thus, R&D work is currently under way to understand the advantages and disadvantages of a toroidal design (see [1]). Nevertheless, the dipole remains the default solution for $\overline{\mathsf{P}}$ANDA.

3.3.2.2 Tracking Detectors

The deflection of particle trajectories in the field of the dipole magnet will be measured with a set of multiwire-drift chambers (MDC), 2 placed before and two behind the dipole magnet. Additionally 2 MDCs or STTs will be placed inside the magnet gap. This will allow us to track particles with highest momenta as well as very low momentum particles, which will curl up inside the magnetic field. Their positions and dimensions are shown in red in Figs. 3.4 and 3.12. The chambers will contain quadratic or hexagonal drift cells of 1 cm width, as in the TS-chambers. Each chamber will contain three pairs of detection planes: one pair with vertical wires and two pairs with wires inclined by +45° and -45° (or slightly smaller). This configuration will allow to reconstruct tracks in each chamber separately also in case of multi-track events. The beam-pipe will pass through central holes in the chambers and the most central wires will be either eliminated or mounted on additional insulating rings surrounding the pipe. The expected momentum resolution of the system for 3 GeV/c protons is $\delta p/p = 0.2\,\%$ and is limited mainly by the small angle scattering on the chamber wires and gas.

3.3.2.3 Particle Identification

Time-of-Flight (TOF) Stop Detector It will consist of a wall of tiles made of plastic scintillator and read out on both ends by fast photo multipliers and such counters inside the dipole magnet opening. The TOF will be measured between the start detector placed in the target region and the stop wall placed about 7 m from the target. It will consist of vertical strips varying in width from 5 to 10 cm to account for the differences in count rate. With the expected time resolution of $\sigma = 50$ ps π-K and K-p separation on a $3\,\sigma$ level will be possible up to momenta of 2.8 GeV/c and 4.7 GeV/c, respectively.

Ring Imaging Cherenkov Counter (RICH) In order to extend the momentum range for the π-K and K-p separation beyond that of the TOF system we consider to use a dual-radiator RICH detector like the one developed for the Hermes experiment [22]. Using two radiators – silica aerogel and C_4F_{10} gas – with different indices of refraction equal to 1.0304 and 1.00137, respectively, provides π-K-p separation in a broad momentum range from 2–15 GeV/c. Due to the usage of a lightweight mirror which focuses the Cherenkov light on an array of photo multipliers placed outside the active volume, the total thickness of the detector is reduced to the freon gas radiator (5% X_0) , the aerogel radiator (2.8% X_0) and the aluminum window (3% X_0).

3.3.2.4 Calorimeter and Muon Detection

As a calorimeter for the forward region we consider to use a system composed of two parts. The first part will be a Shashlyk-type calorimeter, which is suited for the detection of photons and electrons with high resolution and efficiency. The detection is based on lead-scintillator sandwiches, which are read out by wave-length shifting fibers passing through this block. Such techniques have already been successfully used in the E865 experiment [23] and it has been adopted or is being considered for various other experiments [24, 25, 26]. An energy resolution of $4\%/\sqrt{E}$ [27] has already been achieved with such modules. To cover the forward acceptance 12 rows and 23 columns will be required, i.e. 276 modules in total, which would is placed in a distance of 7 to 8 m to the target.

The second part is devoted to measure the energies of neutral hadrons, serves as fast trigger and active muon filter. Especially neutrons and anti-neutrons can not be detected in any other part of $\overline{\text{P}}$ANDA. It is located immediately after the Shashlyk calorimeter and only followed by muon counters. It is considered to refurbish the mid-rapidity calorimeter MIRAC [28] from the WA80 experiment for this purpose. It consists of 30 independent stacks with the dimensions of 22 cm horizontally and 120 cm vertically. Each stack consists of a lead-scintillator electromagnetic section $15\,X_0$ long, and a steel-scintillator hadronic section $6\,X_0$ long. The energy resolution for hadronic showers is about $(0.034 \oplus 0.34/\sqrt{E/\text{GeV}})\%$, respectively. At $\overline{\text{P}}$ANDA the MIRAC stacks will be rearranged such that they cover the forward acceptance for neutral particles at least ($\pm 5^\circ$ and $\pm 10^\circ$ for vertical and horizontal angles respectively). The stacks will occupy about 1.4 m between 8 and 10 m from the target.

Finally, behind this calorimeter there will be a wall of counters for muon identification similar to the ones surrounding the solenoid. Additional muon counters will be used inside the dipole iron or mounted to clamping in the gap between the solenoid and dipole to cover also angles between 5° and 22°.

3.3.3 Trigger and Data Acquisition

In many contemporary experiments the trigger and data acquisition (DAC) system is based on a two layer hierarchical approach. A subset of especially instrumented detectors is used to evaluate a first level trigger condition. For the accepted events, the full information of all detectors is then transported to the next higher trigger level or to storage. The time available for the first level decision is usually limited by the buffering capabilities of the front-end electronics. Furthermore, the hard-wired detector connectivity severely constraints both the complexity and the flexibility of the possible trigger schemes.

Data acquisition concept for $\overline{\text{P}}$ANDA much better matched to the high data rates and to the complexity of the next generation of experiments.

In that approach all detector channels are self triggering entities. They autonomously detect signals and pre-process them to extract and transmit only the physically relevant information. The data related to a particle hit, substantially reduced in the pre-processing step, is marked by a precise timestamp and buffered for further processing. The trigger selection finally occurs in so called compute nodes which access the buffers via a high

bandwidth network fabric. The new concept provides a high degree of flexibility in the choice of trigger algorithms. It makes trigger conditions available which definitely are outside the capabilities of the standard approach, an obvious example being displaced vertex triggering.

In addition, all sub-detectors can contribute to the trigger decision on the same footing, and there are no restrictions due to hard-wired connectivity. Different physics can be accessed either in parallel or after software reconfiguration of the system.

Key technologies to be exploited within the DAQ framework are high speed serial (10 Gb/s per link and beyond) and high-density FPGA (field programmable gate arrays) with large numbers of programmable gates and more and more advanced embedded features.

The basic building blocks of the hardware infrastructure, which can be combined in a flexible way to cope with varying demands, are the following:

- Intelligent front-end modules capable of autonomous hit detection and data preprocessing (e.g. clustering, hit time reconstruction, pattern recognition) are needed. A generic sampling ADC module will be developed to be used e.g. for calorimeters and muon chambers.
- A very precise time distribution system is mandatory to provide a clock normal from which all timestamps can be derived. Without this, data from subsystems can not be correlated.
- Buffered data links provide point-to-point communication, typically via optical links, buffering and on-the-fly data manipulation.
- Compute nodes aggregate large amounts of computing power in a specialized architecture rather then through commodity PC hardware. They may employ FPGAs, DSPs (digital signal processor) or other computing units and have to deal with feature extraction, association of data fragments to events and finally event selection.

A major component providing the glue between all others is the network fabric. Here special emphasis lies in cascadable embedded switches which can be reconfigured to reroute traffic for different physics selection topologies.

Finally, the various algorithms for front-ends and selection levels have to be developed and tested. It should be attempted to develop a common high level programming environment for all components so that algorithms can be coded by physicists rather than engineers in more abstract programming languages than HDL and DSP assembler.

References

[1] M. Kotulla et al., *PANDA Technical Progress Report*, GSI, Darmstadt, 2005.

[2] C. Ekstroem et al., Nucl. Instrum. Meth. **A371**, 572 (1996).

[3] C. Ekström et al., Phys. Scripta **T99**, 169 (2002).

[4] J. Zabierowski et al., Phys. Scripta **T99**, 159 (2002), http://www5.tsl.uu.se /wasa.

[5] Technical report, ATLAS Technical Design Report 11, CERN/LHCC 98-13.

[6] Technical report, CMS Technical Design Report 5, CERN/LHCC 98-6.

[7] P. Holl et al., IEEE Trans. Nucl. Sc. **47**, 1421 (2000).

[8] D. Nygren and J. Marx, Phys. Today **31**, 46 (1978).

[9] C. Brand et al., Nucl. Instrum. Methods **A283**, 567 (1989).

[10] P. Marrocchesi et al., Nucl. Instrum. Meth. **A283**, 573 (1989).

[11] F. Sauli, Nucl. Instrum. Methods **A386**, 531 (1997).

[12] P. Achenbach and J. Pochodzalla, private communication.

[13] H. Staengle et al., Nucl. Instrum. Meth. **A397**, 261 (1997).

[14] Nucl. Instrum. Meth. **A479**, 117 (2002), http://beauty.bk.tsukuba.ac.jp/ belle/ nim/ total/.

[15] K. Mengel et al., IEEE Trans. Nucl. Sci. **45**, 681 (1998).

[16] R. Novotny et al., IEEE Trans. Nucl. Sci. **47**, 1499 (2000).

[17] M. Hoek et al., Nucl. Instrum. Meth. **A486**, 136 (2002).

[18] Technical Proposal, CERN/LHC 9.71.

[19] Technical Proposal, 1994, CERN/LHCC 94-38, LHCC/P1.

[20] E.Auffray et al., Moscow, 1999.

[21] http://www-dapnia.cea.fr/ Sphn/ Deformes/ Agata/ index.shtml.

[22] N. Akopov et al., Nucl. Instrum. Meth. **A479**, 511 (2002).

[23] G. S. Atoyan et al., Nucl. Instrum. Meth. **A320**, 144 (1992).

[24] G. David et al., Performance of the PHENIX EM calorimeter, Technical report, PHENIX Tech. Note 236, 1996.

[25] A. Golutvin, (1994), HERA-B Tech. Note 94-073.

[26] LHCb Technical Proposal CERN LHCC 98-4, LHCC/P4, 1998.

[27] I.-H. Chiang et al., (1999), KOPIO Proposal.

[28] T. C. Awes et al., Nucl. Instrum. Meth. **A279**, 479 (1989).

Chapter 4

Tracking Detectors

This chapter describes technical solutions for detector elements fulfilling the inner tracking requirements in $\overline{\mathrm{P}}$ANDA. Both, the MVD and the STT are addressed.

4.1 Micro-Vertex Detector

4.1.1 Introduction

The Micro Vertex Detector (MVD) of the $\overline{\mathrm{P}}$ANDA installation at the HESR storage ring for antiprotons will be of central importance for a number of the physics goals defined in Sec. 2. All experiments that aim at an identification of open charm and strangeness depend on the identification of secondary decays of particles in displaced vertices other than the primary reaction point.

Decays of charged particles are often accompanied by neutral particles in the final state, so that they cannot be reconstructed from the observed charged decay products, but a significant kink may be used to enhance the probability of detection of any of these, such as the Σ^+, Σ^- and other baryons. This will however not work for kinks that come very close to the primary vertex as in case of the charged D meson. Here, exclusive detection of the decay particle tracks will be needed for the reconstruction of displaced vertices. As a minimum requirement, two charged tracks intersecting at a space point displaced from the primary vertex could be used for an identification of delayed decays early in the data acquisition chain.

Strange hadrons have decay lengths on the order of cm while charmed mesons and baryons decay within several ten to a few hundred μm. The vertex detector and the adjoining tracking device will have to be suited for both. While $\overline{\mathrm{P}}$ANDA will focus on charm production, the identification of kaons will greatly enhance the efficiency also for D mesons since they show large branchings into channels accompanied by kaons. Thus, a design that can handle both length scales will greatly improve the efficiency of $\overline{\mathrm{P}}$ANDA.

All experiments currently employing or planning to employ silicon pixel detectors work at rather high particle momenta, so that the charged particles usually are minimum ionizing. $\overline{\mathrm{P}}$ANDA will have to handle much slower particles on average. While this offers the

opportunity to contribute to the particle identification through energy loss measurements, the detector thickness will be a much more crucial parameter for the detector design than in many other applications. Experiments such as BaBar [1, 2] have therefore chosen to construct their vertex detector from silicon strip detectors, which allow smaller mass budgets and therefore smaller multiple scattering for the same angular coverage. This concept does however compromise on the number of hits per unit area and time that can be handled. With the interaction rates foreseen for the $\overline{\text{P}}$ANDA experiment, which shall also be met in experiments using heavy targets, the innermost detector layers will be exposed to rather high particle densities, so that a pixel design is favored at least for the innermost layers surrounded by the strip layers for the longer decay length. $\overline{\text{P}}$ANDA plans for five track points in the vertex detector, which will allow usage of the information in the early trigger stages even if one of the detectors is missing in a track. Fig. 4.1 shows that in the momentum range encountered in $\overline{\text{P}}$ANDA experiments the energy deposit in silicon changes rapidly. Below about 700 MeV/c, this energy loss may be used to discriminate between particle species. Therefore the MVD can extend the momentum diapason of particles available for identification (see. Sec. 3.3.1.4) to the much lower values and significantly increase the efficiency of the particle identification.

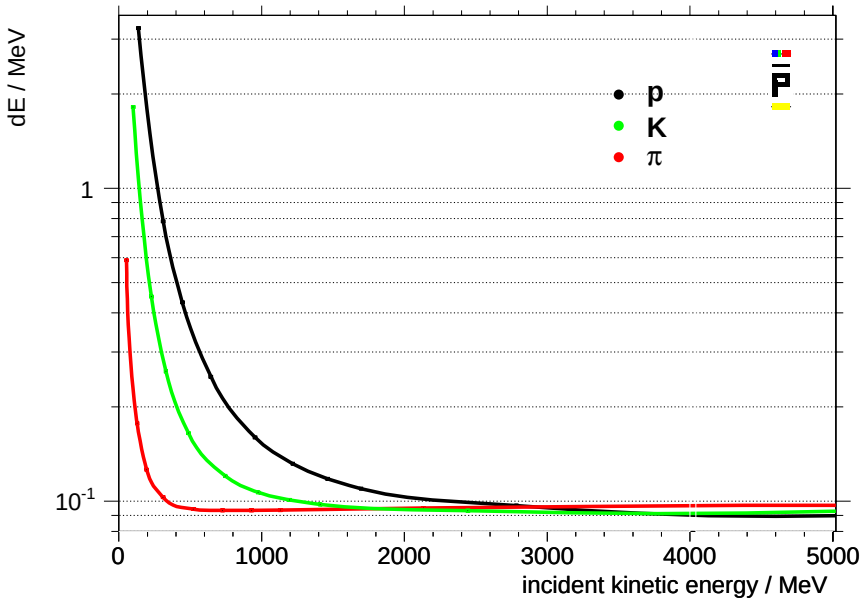

Figure 4.1: Energy loss of the indicated particle species in 400 μm of silicon as a function of momentum.

The high interaction rates stress the issue of radiation hardness of the sensors and readout electronics as it was pointed out in Sec. 3.2.4. The expected neutron flux will be considerable and close to the limits of present-day technology for radiation-hard electronics. Our estimate lies about an order of magnitude below what can be expected as reasonable limit for typical detector lifetimes of the order of ten years. Therefore, while the issue still

reaction channel	detected particle	tracking used for ...
$\overline{\mathrm{p}}\mathrm{p} \rightarrow \phi\phi$	$2K^+\ 2K^-$	momentum measurement (PID)
$\overline{\mathrm{p}}\mathrm{p} \rightarrow \eta_c$	$K^\pm\ \pi^\mp\ K^0_S$	momentum measurement (PID)
$\overline{\mathrm{p}}\mathrm{p} \rightarrow \psi(3770)$	$D\overline{D}$	charm detection online
	$\rightarrow K$'s and π's	momentum measurement (PID)
$\overline{\mathrm{p}}\mathrm{p} \rightarrow \psi(4040)$	$D^{*+}D^{*-}$	charm detection online
	$\rightarrow K$'s and π's	momentum measurement (PID)
		track reconstruction for the slow pions
$\overline{\mathrm{p}}A \rightarrow D\overline{D}\ X$	D	inclusive charm ID online

Table 4.1: Benchmark experiments that require optimum performance of the vertex tracking. The most serious challenge will be D identification due to the very short decay lengths of these mesons.

can not be neglected completely, it does not require special attention in a way that poses a limiting factor for the layout and does not warrant extensive research and development on radiation-hard electronics.

4.1.2 Physics with the MVD

The key experiments are discussed in detail in Sec. 2. Some of them can only be met with a vertex detector of high quality that features resolutions suitable for the task of charm identification. Tracks of charged mesons have to be measured with a spatial resolution no worse than the typical decay lengths of the order of $100\,\mu$m. In particular, this is the case for some of the experiments listed in Table 4.1, which all require use of the vertex detector for quite different reasons. The most stringent requirements are given by those reaction channels where the D decay will be used to select certain event patterns from the data stream during data acquisition, as indicated in the last column of the table.

For charmonium spectroscopy slightly above the $D\overline{D}$ threshold, the momenta of the outgoing particles are quite confined by the center-of-mass motion which is conserved in the D's direction and velocity. As the combined mass of the particles in the D decay is much lower than the D's mass, they acquire additional momentum which is still somewhat correlated with detection angle. This is shown in Figs. 3.2 for the K's and π's from the reactions $\overline{\mathrm{p}}\mathrm{p} \rightarrow \psi(4040) \rightarrow D^{*+}D^{*-} \rightarrow D^0\,\pi^+ D^0\,\pi^- \rightarrow K^-\pi^+\pi^+ + c.c.$ and $\overline{\mathrm{p}}\mathrm{p} \rightarrow \psi(3770) \rightarrow D^+\,D^- \rightarrow K^-\pi^+\pi^+ + c.c.$. The covered momentum range is large. The particles are emitted with appreciable transverse momentum components, but emission into the forward hemisphere in the laboratory system is nevertheless favored due to the high Lorentz boost. From this, it is obvious that the physics requirements call for a very high granularity and optimum resolution for the forward region, while coverage up to 90° may be sufficient for many cases.

The separate problem, however, will be a tracking of slow pions from D^* decays (outlined by ellipse on Figs. 3.2 a), which curling up inside MVD. Due to the small opening angle such pions will be detected only in the forward part of the MVD. It anticipate **a small layer thickness** otherwise the low momenta pions will be significantly distorted due to

the big energy losses (see Fig. 4.1) and the large small-angle scattering (see Fig. 4.2) for such slow particles.

In addition, the experimental program at $\overline{\mathrm{P}}$ANDA puts emphasis on the high-resolution spectroscopy of electrons as well as photons. Photons can be used to reconstruct the neutral part of the hadronic spectrum from the particle decay chains of the reactions under study, in particular the π^0 and η meson momentum vectors. They may also be of interest as electromagnetic probes for certain reactions. Electrons are excellent tags for D meson spectroscopy ($BR(D \rightarrow e^+ + anything) \sim 18\%$). They carry information on the flavor of the decaying charm. e^+e^- can also be used to reconstruct mesonic properties inside the nuclear medium when heavy targets are studied. Therefore, any material, especially when high-Z materials are involved, near the primary target may cause background due to bremsstrahlung and pair production. While vertex reconstruction may help to discern primary e^+e^- from pairs generated in secondary interactions, background in any case restricts the use of electrons in the event recognition during data acquisition. Therefore, any further minimization of the material load close to the interaction region while maintaining the spatial resolution of the detector will be advantageous.

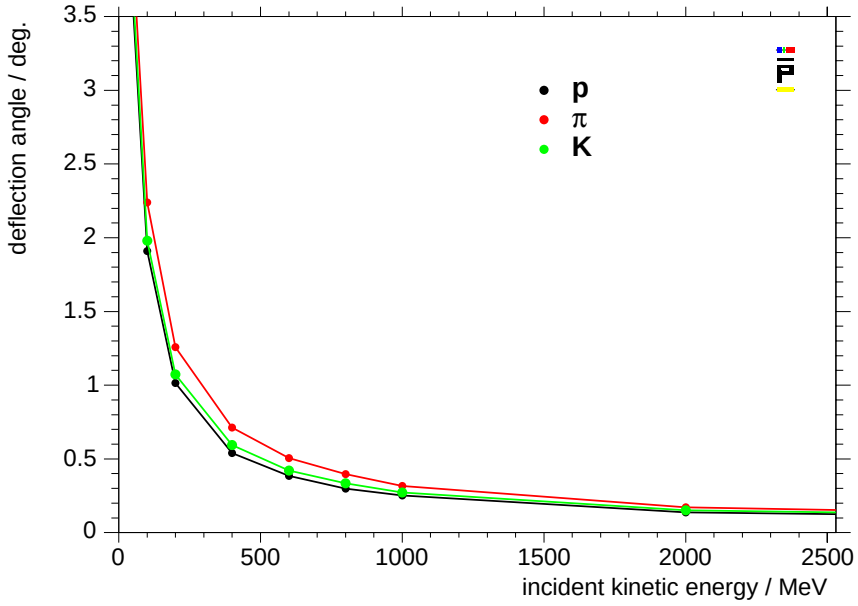

Figure 4.2: Average deflection due to small-angle scattering as a function of incident energy for protons, kaons and pions in 400 μm of Si.

In summary, the main criteria which should be taken into account in design of the $\overline{\mathrm{P}}$ANDA MVD are:

Thickness of the material used for the MVD construction This is of major concern since $\overline{\mathsf{P}}$ANDA will have to cope with low-energy particles, which is in contrast to the high-energy experiments considered as model detectors for the layout. In addition, energy loss measurements would be of advantage as they could be used in the particle identification at low energy.

Layout for a fixed-target experiment While the forward-focusing of all particles reduces the quality requirements for the backward hemisphere of the barrel structure, the fixed-target layout of the experiment requires good coverage of very forward angles with very good spatial resolution. As angles below about 20° cannot be reasonably covered with barrel structures, additional layers have to be added in forward direction with a more disk-like structure oriented more or less perpendicular to the beam.

Applicability to a variety of physics cases and experimental setups of the target region At present, the foreseen options for the $\overline{\mathsf{P}}$ANDA target include hydrogen pellet targets as well as hydrogen gas jets, cf. Sec. 3.3.1.1. In addition, heavy targets will be used as wires or foils. All these cases with quite different interaction geometries will have to be handled equally well with the same vertex detector.

4.1.3 Monte-Carlo Simulations of the MVD construction

In accordance with requirements are listed in previous section the first MVD layout have been created. It was sketched in the Conceptual Design Report [3] and shown in Fig. 4.3. This early version of the detector was used to verify the basic parameters of the detector. It features a barrel section with five layers of pixels, which were taken to be $50 \times 300\,\mu\text{m}^2$ in size and five forward disk structures with pixel sizes of $100 \times 150\,\mu\text{m}^2$. Each of the silicon sensor layers was assumed to be $200\,\mu$m thick (corresponding to 0.25% X_0). The position resolution of the arrangement was approximated by a standard deviation of $\sigma = d/\sqrt{12}$, where d is the pixel size in either direction independently. In reality, charge sharing among a number of neighboring cells will likely result in a somewhat better resolution than purely given by geometry. The beam pipe was assumed to consist of BeAl(7/3) alloy and is only $400\,\mu$m thick including a safety factor 4. The barrel structure thus has about 7.2 million pixels, while the forward wheels add another 2 million. To study the performance of that geometry the $\overline{\mathsf{P}}$ANDA offline software (cf. Sec. **??**), based on GEANT4 and ROOT packages, have been used. As it shown on the Fig. 4.4 the nominal resolution of $\sigma_\phi = 15\,\mu$m and $\sigma_z = 70\,\mu$m for the first three barrel layers, $\sigma_\phi = 70\,\mu$m and $\sigma_z = 15\,\mu$m for the outer two barrel layers (chip readout turned by 90°) and $\sigma_\phi = 25\,\mu$m, $\sigma_z = 40\,\mu$m for the disks is sufficient to allow spatial single-track resolution of $\sigma_D \sim 40\,\mu$m in transverse and $\sigma_z \sim 30\,\mu$m in longitudinal directions. While these values are within the design values requested for the D meson tagging, any additional scattering will contribute to the resolution, so that it is obvious that this issue needs further consideration incorporating more realistic designs, geometries and knowledge about the detector. For example, the $200\,\mu$m sensors have so far not been equipped with readout chips, which is of course mandatory in a scenario where present-

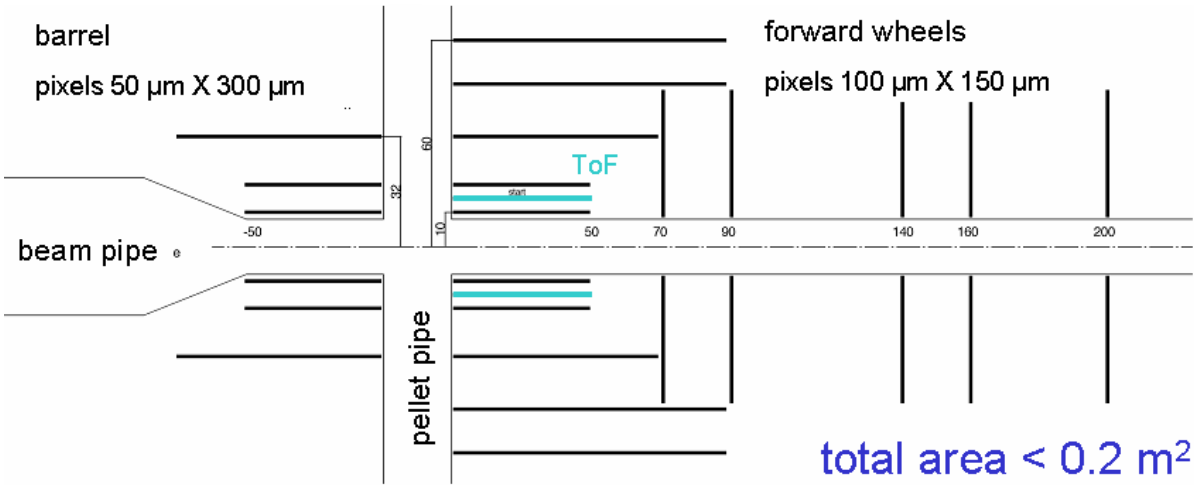

Figure 4.3: Early sketch of the detector layout as used in the conceptual design of $\overline{\text{P}}$ANDA.

day detector layouts are used, where a readout chip of about the same thickness is bump-bonded to each sensor. The detector support structure, cabling and cooling further add to the material budget. All these effects have been successively incorporated into the Monte-Carlo treatment of the detector setup, and their influence has been systematically investigated.

Layout of the MVD have been changed in accordance with results of the Monte-Carlo simulation and with technical requirements as one can see on the Fig. 4.5 Diameter of the beam pipe in the backward direction have been enlarged to increase the pumping speed from the target. As the result the first MVD barrel layer have been shortened in half of his length. In order to compensate the loss of hits in backward hemisphere a length of the forth MVD barrel layer have been extended in the backward direction. Position of the first two forward disks have been shifted in forward direction to free some space for cabling. Diameter of this disks also have been slightly reduced to avoid an overlap with the forth MVD barrel layer.

The structure of the barrel layers and the forward disks have also been changed. Fig. 4.6 shows a schematic drawing of the cross section of a vertex detector stave as incorporated into the next generation of simulations. While the thickness of the sensor has been chosen to match the values of the ALICE detector design and are thus smaller than previously used [4], the Monte-Carlo representation of the detector now contains readout chips and cooling as well as a bus structure as an equivalent for the readout and detector utilities. The total material budget which a traversing particle meets is now quite inhomogeneously distributed and ranges between 0.96% and 3.6% radiation lengths. A cross section through the barrel structure is shown in Fig. 4.7. On the right side of the figure, a disk structure made from similar sensor staves, which are put together into a wedge shape, is shown. On the Fig. 4.8 one can see detector geometry as it written into the $\overline{\text{P}}$ANDA Monte-Carlo simulation. Fig. 3.8 is an artist's rendering of the cross section of the MVD detector.

Results from the analysis of a simulation using the arrangement shown in Fig. 4.5, but without a target pipe, are summarized in Fig. 4.9. The pixel sizes used are $(300 \times 50)\ \mu\text{m}^2$

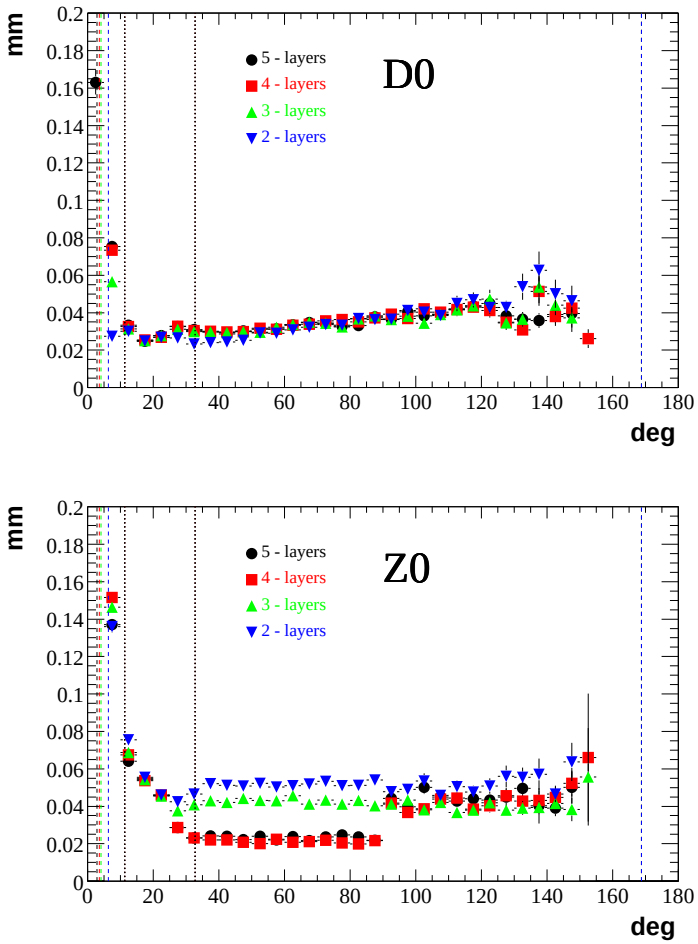

Figure 4.4: Resolution of the transverse (D0) and longitudinal (Z0) coordinates, respectively, as simulated for the reaction $\overline{\mathrm{p}}\mathrm{p} \rightarrow \psi(3770) \rightarrow \mu^+\mu^-$ for the different number of barrel layers. The vertex detector setup used in the simulation is from Fig. 4.3, but without a target pipe. See text for details.

and $(150 \times 100)\,\mu\mathrm{m}^2$ in forward direction, respectively. The pixels in the first barrel layer were oriented along the beam axis while in four other layers the pixel orientation was perpendicular to the beam direction. The data is for muons originating from the decay of a of $\psi(3770)$ resonance produced in $\overline{\mathrm{p}}\mathrm{p}$ annihilation. It is obvious that there is some variation in the resolution as a function of polar angle both for the transverse (D_0) as well as the longitudinal (Z_0) resolution. This is due to the rather large variation in a thickness of the material that has to be penetrated by the particles depending on their emission angle. This is one of the shortcomings of the depicted design independent of version and orientation of the individual pixel layers and will have to be improved in future layouts as described later. The large error bars in the very backward region are due to the lack in statistics for the reaction studied here because the muons carry a large longitudinal momentum component from the center-of-mass motion. For particles penetrating the five detector layers more or less perpendicular to the sensor orientation, resolutions better

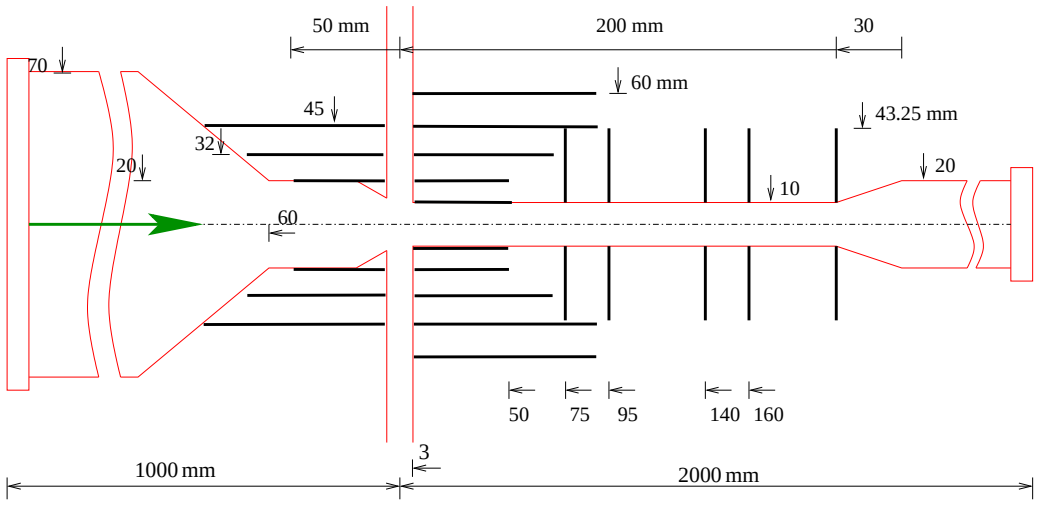

Figure 4.5: The figure shows the longitudinal section of the detector setup as used in a later stage of the overall $\overline{\text{P}}$ANDA simulation. The beam direction is shown by the arrow.

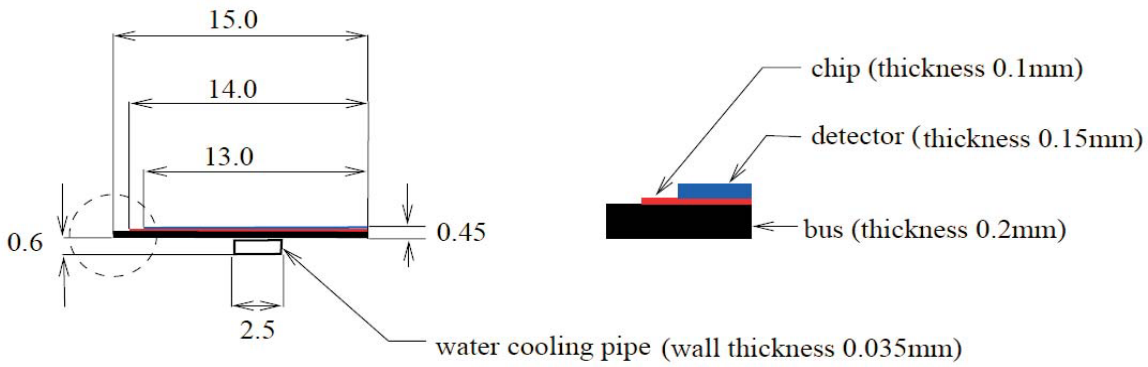

Figure 4.6: Sketch of the detector layout as used in a later stage of the overall $\overline{\text{P}}$ANDA simulation. The figure shows the cross section of one of the detector staves. These are used in the arrangement of the barrel part and the forward disks as shown in the next figure.

than 20 μm can be achieved.

The calculation shown here does not include the pipes for the target in- and outlet, which will add further material at angles around 90° and result in smaller efficiencies for particle tracking in the MVD. To study this problem the decay $D^+ \to K^-\pi^+\pi^+$ has been simulated for the different target pipe diameters. The properties of the particle generator were modified such way that all D-mesons decays at the location (0.1, 0.1, 0.4) mm. The results are shown on the Fig. 4.10. As one can see the vertex resolution remains constant in transversal direction independent of the target pipe diameter while deteriorates in longitudinal direction for the target pipe diameter more than 20 mm. The efficiency plot shows the some aggravation starting from the 30 mm target pipe diameter.

Due to the significant Lorentz boost D-meson decay vertices are shifted to the forward

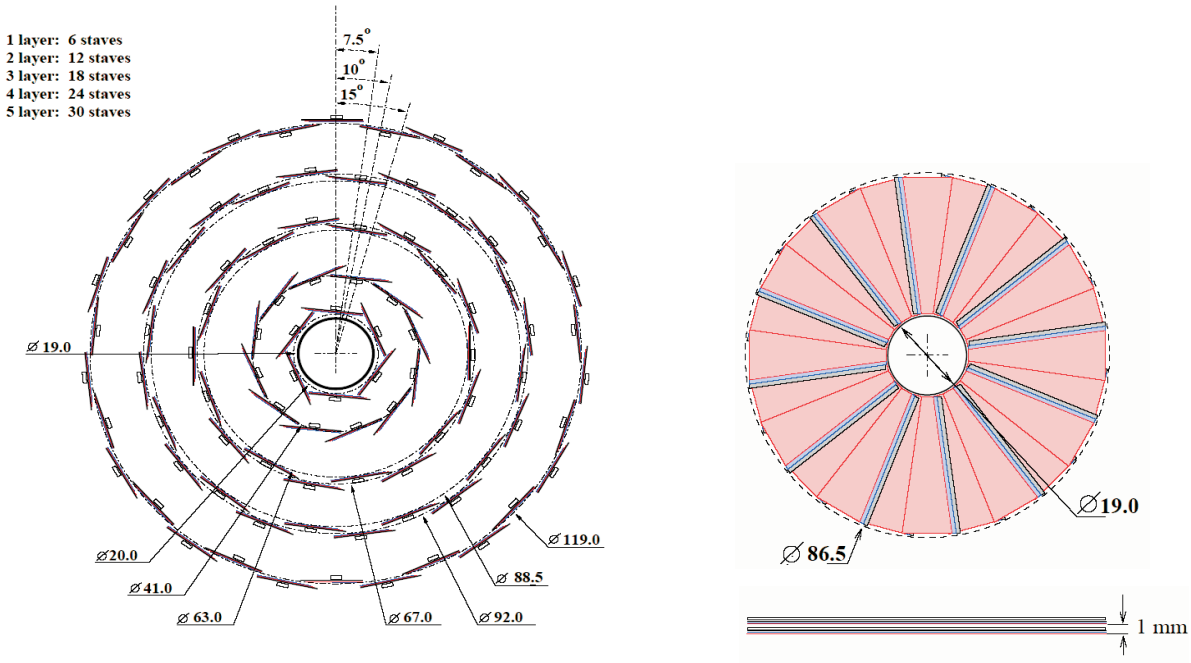

Figure 4.7: Sketch of the detector layout as used in a later stage of the overall $\overline{\text{P}}$ANDA simulation. 90 of the staves as shown before are used in the arrangement of the barrel part. The same staves arranged into wedge-shaped structures were used in the design of the forward disks, as shown on the right side.

Table 4.2: This table represents the survival probability for the D-mesons after the longitudinal or transversal spatial cut for the secondary decay vertex displacement.

	Cut value in μm		
Survival probability in ...	100	120	150
longitudinal direction	83%	80%	76%
transversal direction	5.4%	3.2%	1.5%

direction. It can be seen on Fig. 4.11, where the D-meson decay vertices from the reaction $\overline{\text{p}}\text{p} \to \psi(3770) \to D^+D^- \to K^-\pi^+\pi^+ + c.c.$ are plotted. The spatial cut on the secondary decay vertex can be applied in longitudinal or transversal directions in order to help in a separation of the signal from D-mesons decays from the background. The Table 4.2 represents the survival probability for the D-mesons after such cut applied in the longitudinal or transversal direction. Of course, such selection requires the spatial resolution on the vertex at least two time better than applied cut value. The simulation shows (see Fig. 4.12) the reasonable good reconstruction efficiency of the one or two D-meson signal from $\psi(3770) \to D^\pm \to K^-\pi^+\pi^+ + c.c.$ decay using the longitudinal cut, for the all target pipe diameters. Application of the transversal cut significantly worsens the reconstruction efficiency and hardly can be employed for the D-meson selection in the real experiment. This information makes use of the pellet or wire target (see Sec. 3.3.1.1)

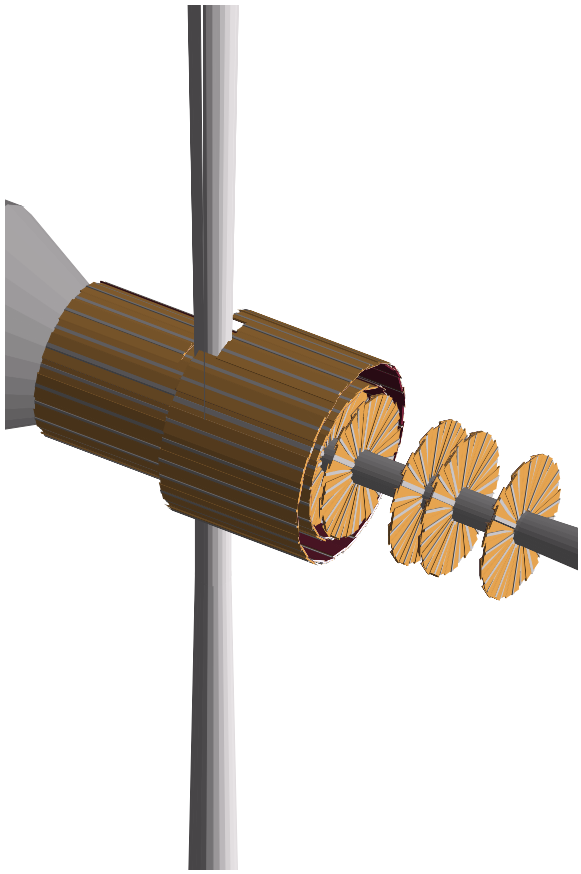

Figure 4.8: View of the detector structure as it described in GEANT4 Monte-Carlo simulation. The beam is coming from the left hand side.

preferential compared to all kind of gas targets.

The material budget of the MVD have been studied by the simulation of the photon conversion probability in MVD constructions. The decay $\overline{\mathrm{p}}\mathrm{p} \rightarrow 3\pi^0 \rightarrow 6\gamma$ have been used as a photon source. The incident antiproton momentum was 6.2GeV/c. The photon conversion probability, which was found $\sim$3%, will represent a significant background for the charmonium decays into e^+e^- pair as well as Dalitz decays of the π^0 ($\pi^0 \rightarrow e^+e^-\gamma$, BR=1.2%). That puts tight constrants on the total MVD material budget.

The results of the simulations should be taken into account during the following MVD design.

4.1.4 Basic Requirements

From the physics goals of $\overline{\mathsf{P}}$ANDA as well as the simulations and the overall layout of the experiment, certain basic requirements for the vertex detector can be deduced that will have to be met in the final design. This includes:

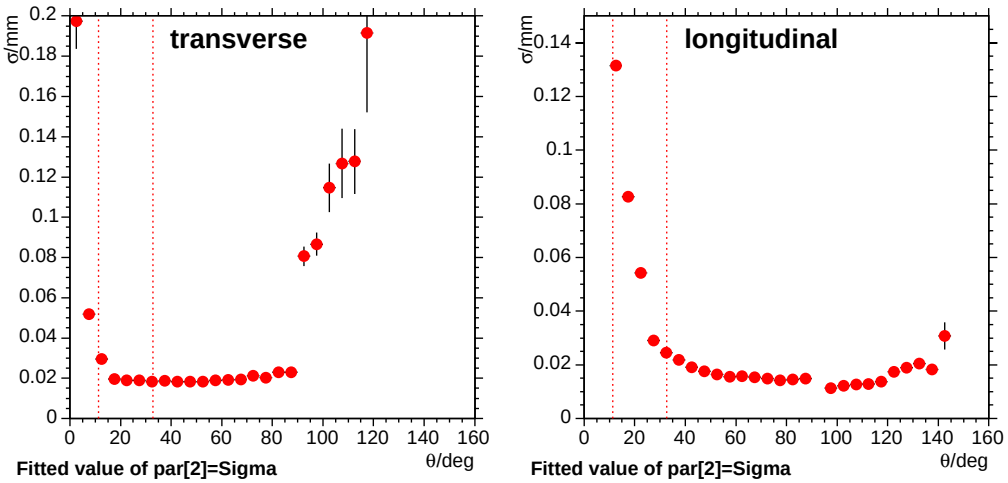

Figure 4.9: Resolution of the transverse and longitudinal coordinates, respectively, as simulated for the reaction $\overline{\mathrm{p}}\mathrm{p} \to \psi(3770) \to \mu^+\mu^-$. The vertex detector setup used in the simulation is from the previous figure, but without a target pipe. See text for details.

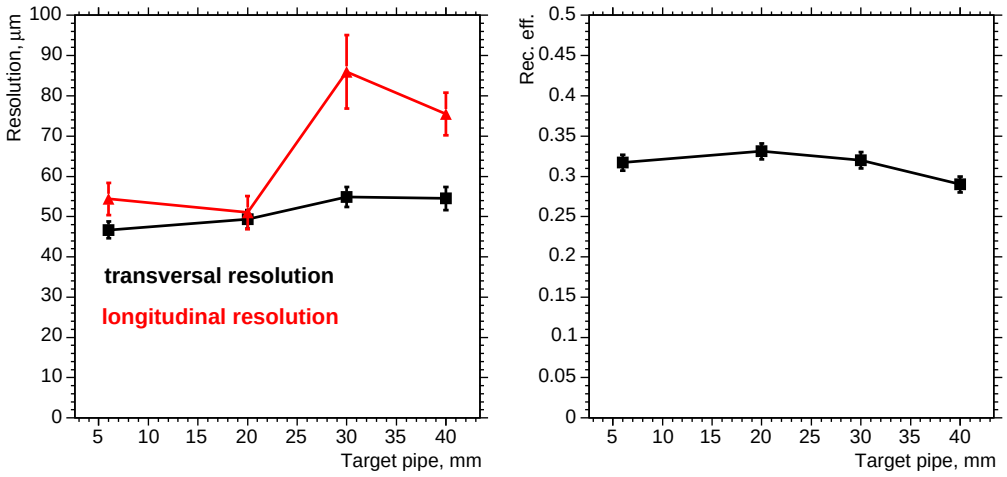

Figure 4.10: On the left figure the vertex resolution for the decay $D^+ \to K^-\pi^+\pi^+$ is shown. The right figure represents the D-meson reconstruction efficiency. All D-mesons were produced at the same location. See text for details.

Spatial Resolution The vertex detector shall have a spatial resolution better than $100\,\mu$m. One of the most demanding tasks is the recognition of $D\overline{D}$ events in stand-alone mode as decay products of $c\overline{c}$ resonances not much heavier than the meson pair. Therefore the best resolution is required along the beam (z-direction). The resolution in r/ϕ direction should not be significantly inferior to the z-direction. It is necessary to note that this task also required a good knowledge of the primary vertex position.

Material Budget A five-layer pixel structure adds too much material, so that the fifth layer does not contribute to the track resolution any more (cf. Fig. 4.4). In addition, a

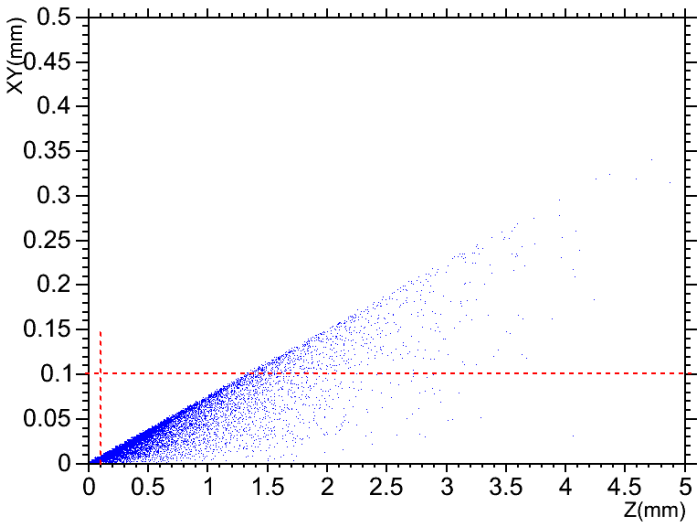

Figure 4.11: Distribution of decay vertices from the decay $\overline{\mathrm{p}}\mathrm{p} \to \psi(3770) \to D^{\pm} \to K^{-}\pi^{+}\pi^{+} + c.c.$ The red dashed lines are the graphical representation of the spatial cut on the secondary decay vertex applied either in the longitudinal (vertical line) or in the transversal (horizontal line) directions at 100 μm distance from the primary vertex.

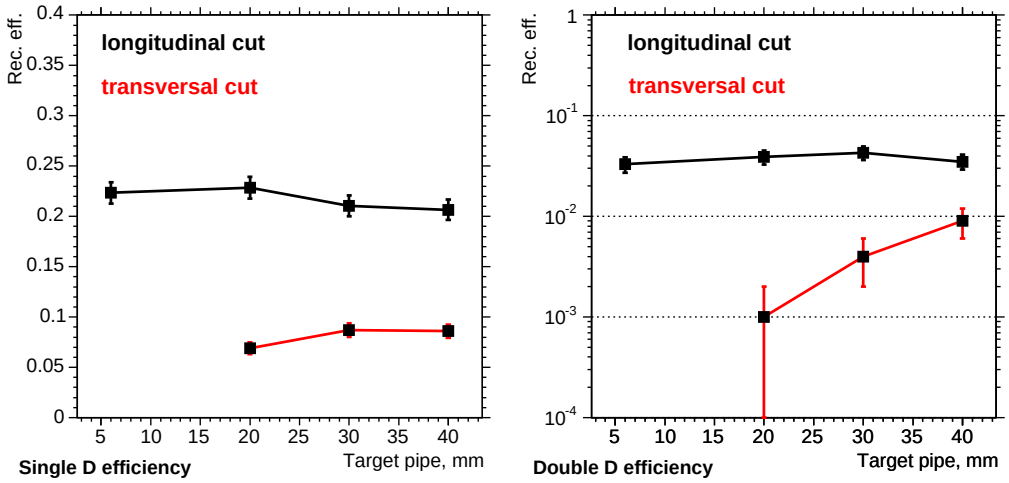

Figure 4.12: Single (left figure) and double D-meson reconstruction efficiency from $\overline{\mathrm{p}}\mathrm{p} \to \psi(3770) \to D^{\pm} \to K^{-}\pi^{+}\pi^{+} + c.c.$ reaction. The black curves correspond the reconstruction efficiencies when the spatial cut on the secondary decay vertex applied in the longitudinal direction while the red lines correspond the case of the transversal direction of the cut.

photon conversion in all layers would generate an excessive amount of electron-positron pairs, which must be considered background for the observation of certain reactions to be measured, such as Dalitz decays, leptonic decays of charmed mesons and $e^{+}e^{-}$ decays of vector mesons, for example in nuclear matter. Therefore, the inner three layers are planned to be constructed from pixel sensors, while the outer two from double-sided strip detectors.

Minimized Photon Conversion While in principle connected to the material budget, the conversion is also influenced by the charge number of the elements used in the construction. High-Z materials such as lead or gold will contribute more to the photon-to-e^+e^- showers than low-Z material such as carbon fiber.

In view of the last two arguments, the contribution of the vertex detector to the total material budget, in units of radiation length, shall be kept below $X/X_0 = 4\%$.

Geometry of the Barrel and the Disks The minimum radius of the innermost layer of the vertex detector is given by the beam pipe for which 1 cm was defined, while the outer radius of 14 cm defines the maximum, limited by the straw detector inner holding structure. The minimal radius of the beam pipe is defined by the sufficient pumping speed from the target to the downstream exit where the pumps can be positioned. Because $\overline{\mathsf{P}}$ANDA is a fixed-target experiment, the beam momentum will cause an excess of particles in the forward hemisphere, so that the region around the beam pipe is important for the complete reconstruction of final states.

Readout Speed The readout has to allow continuous data collection from the detector without triggering. As multiplicities are expected to be rather small (a maximum of 16 charged particles was estimated for the studies envisaged), the more serious aspect of data extraction from the vertex detector is caused by the rather high interaction rates, which will be in excess of 10^7 annihilations per second.

4.1.5 Summary

The results of simulations show the possibility of building of the MVD using combination of pixel and strip detectors. Chosen detector geometry, consisting of the barrel and forward parts, is in the good agreement with requirements for the fixed target experiment.

But still a lot of R&Ds and simulations of possibly promising developments are needed, before a final scrutinizing of the technology for the $\overline{\mathsf{P}}$ANDA vertex detector.

4.2 Straw Tube Tracker

4.2.1 Introduction

The main tracking element of the $\overline{\text{P}}$ANDA **TS** is the Central Tracker (CT). The main goal of this device is providing precise measurements of the track coordinates as well as particle momentum. This information than will be used other subsystems for the determination of particle properties. Another possible task for CT is registration of the secondary vertecies from decays relatively long particles such as K_s^0, $K^{\pm}$ and $\pi^{\pm}$ mesons, Λ, Σ and Ω barions, which mostly will decay outside the MVD.

The following requirements to the CT result from mentioned above goals:

- large solid angle coverage around the interaction area;
- resolving complex pattern of multiple tracks;
- high spatial resolution for secondary vertices, $\sigma_{r\varphi} \sim 150\mu$m, $\sigma_z \sim 1$ mm;
- high momentum resolution of reconstructed trajectories, $\delta p/p \sim 1\%$;
- minimal detector material, $X_0 \sim 1\%$ for low multiple scattering and energy loss of passing tracks and suppression of secondary background production by interactions with the detector material;
- high rate capability of the detector and especially of its components in the forward region reaching values of $3 \cdot 10^4\,\text{cm}^{-2}s^{-1}$, fast electronic readout;
- resistance against ageing effects with the expected accumulated charge density on the level of 0.1-1 C/cm/year;
- operation in non-uniform magnetic field of the $\overline{\text{P}}$ANDA solenoidal magnet varying by up to 5% along the beam axis.

This will be achieved by surrounding the vertex detector with a cylindrical low-mass device.

For the cylindrical device inside the TS, two solutions could be chosen: a Straw Tube (STT) array, which is the subject of this section, or a high-rate Time Projection Chamber (TPC), which described in the great details in [3].

4.2.2 Design considerations

The Straw Tube Tracker (STT), being the set of the cylindrical double layers, will occupy a region inside the superconducting solenoid starting at a radial distance of 15 cm from the beam line, up to 42 cm. Each double layer consist of 150 cm long drift tubes (straws) placed in two adjacent cylindrical layers. Straws in the first layer packed as much tight as possible. Straws in the second layer are shifted by the half of the angular step compare to the tubes in the first layer. This inevitably leads to some space between the tubes in

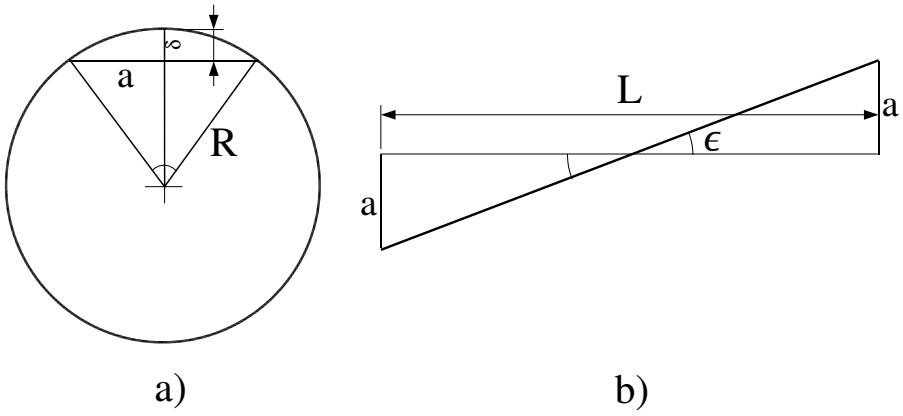

Figure 4.13: Illustration of the parameters of equation 4.1.On figure a): layer as it seen from one side; b): top view.

the second layer and as a consequence to some inefficiency in the track registration. From other hand it helps to resolve ambiguity when two track cross the same tube. In that case only track closest to the anode wire will be registered. The second, more distant track, in own turn will be closest to the anode in the next layer and thus will be also registered.

The first and the last double-layers will be aligned parallel to the beam axis, while the remaining layers will be apparently arranged at skew angles ranging from 2° to 3°, allowing z-coordinate reconstruction. The skew angle is the angle between the straw tube and detector axis. Chosen values of skew angle provide spatial resolution in z-direction between 3 and 5 mm. If it needed the skew angle can be increased up to 4-9° depend on the layer diameter. But one shouldn't forget that as a consequence of the skew angle, the distance between of straw tube from the detector axis varies continuously along z-direction, reaching its minimum at center, which result in the hyperbolic shape of the layer. The radii difference along the layer is called *geometrical sag* and can be calculated as follow:

$$\delta = R\big(1 - \sqrt{1 - \frac{L^2 \tan^2 \epsilon}{4R^2}}\big), \tag{4.1}$$

where L and R are the layer length and radius at the end, ϵ is the skew angle (see Fig. 4.13). The geometrical sag limits the skew angle when it becomes comparable with the distance between neighboring layers (cf. Table 4.3). Another result of the radii difference for layers with skew angle will be some additional space between the straws at the end. For instance the skew angle for the second layer can not be more than 4 degrees, assuming the equal spacing between the layers and number of layers equal 15, otherwise distance between the first and the second layer become zero. In the region closer to the beam pipe the occupancy will be higher, due to curling low-momentum tracks. Therefore, the straw diameters will vary from 4 mm for the innermost tubes, to 6 mm for the central ones, and to 8 mm for the outmost layers. In greater details this question is discussed in Sec. 4.2.2.1.

Table 4.3: This table represents the geometrical sag and a space between the straw ends depending on the skew angle and the tube diameter for the first and last *skewed* layers.

	radius = 17 cm tube diameter = 4 mm					radius = 17 cm tube diameter = 8 mm				
Skew angle, deg	2	3	4	6	9	2	3	4	6	9
Geometrical sag, mm	2	4.6	8.3	19.3	48.4	0.3	0.8	1.5	3.3	7.7
Intertube gap, μm	47	108	195	454	1140	6	16	30	66	154

The main task of CT is providing an information about particle momentum. The relative error for total momentum can be expressed as follows [5]:

$$\left(\frac{\sigma_p}{p}\right)^2 = \left(\sqrt{\frac{720}{n+4}}\frac{\sigma_{xy}p\sin\theta}{0.3BL^2}\right)+\left(\frac{5.23\times10^{-2}}{\beta\sqrt{LL_r\sin\theta}}\right)^2+\left(\cot\Theta\sigma_\theta\right)^2[GeV/c,T,m,radians], \quad (4.2)$$

where p is a total particle momentum, σ_p is the total momentum resolution, n is number of *equally* spaced hits on the track, σ_{xy} is the spatial resolution of the detector in transversal plane, θ is the track polar angle and σ_θ is an polar angle resolution of the tracker, L and L_r are the track path length and the tracker radiation length, correspondingly and B is the magnetic field strength. In contrast to many experiments listed in Table 4.4, when straw tube used as auxiliary tracker, the STT will serve as main tracking element in TS of the $\overline{\mathsf{P}}$ANDA experiment. That fact assume a relatively high thickness of the tracker in terms of an radiation length (see. Table 4.5). In addition, the space available for the STT is very limited. As result, the lever arm of the spectrometer is only $(42-15)/2 = 13.5$ cm, in contrast to other experiment, where the lever arm is about 50-70 cm (cf. [6], [7]). Due

Table 4.4: Recent experiments using straw chambers. Straw dimensions include tube length (L), diameter (D) and tube wall thickness (d).

Experiment	Operation Start	Straw Properties			
		No	$L\times D\times d$ [mm^3]	Material	Resolution [μm]
DELPHI [8]	1995	960	$2000\times(7.9-8.9)\times0.03$	Mylar	$96(\sigma_{x,y})$
FINUDA [9]	1997	2 424	$2500\times15\times0.03$	Mylar	$150(\sigma_{x,y})$ 500 (σ_z)
WASA [10]	1998	1738	$424\times4,6,8\times0.025$	Mylar	$200(\sigma_{x,y})$ 500 (σ_z)
KEDR [11]	1998	312	$670\times10\times0.02$	Mylar	$50(\sigma_{x,y})$
COMPASS [12]	2002		$3000\times6,10\times0.06$	Kapton	$200(\sigma_{x,y})$
COSY-TOF [13]	2005–06	3 100	$1050\times10\times0.03$	Mylar	$150(\sigma_{x,y,z})$
LHCb [14]	2008–09	60 000	$2500\times5\times0.1$	Kapton	
BTeV [15]	2008–09	78 132	$800\times4\times0.05$	Kapton	

to this factors (big radiation length and small lever arm) the momentum resolution of STT itself will be relatively poor, about 1.5%, as it shown on Fig. 4.14 for the versions with 11 and 15 double layers. Following values were used for that calculations: magnetic field strength of 1.5 T, $n = 2 \times$ *number of layers*, path length $L = 0.27$ m, the tracker spatial resolution $\sigma_{xy} = 150\,\mu$m, the tracker angular resolution σ_θ equals 6×10^{-4}, the radiation length $L_r = 35$ m for 11 double layers and 26 m for 15 double layers. Addition

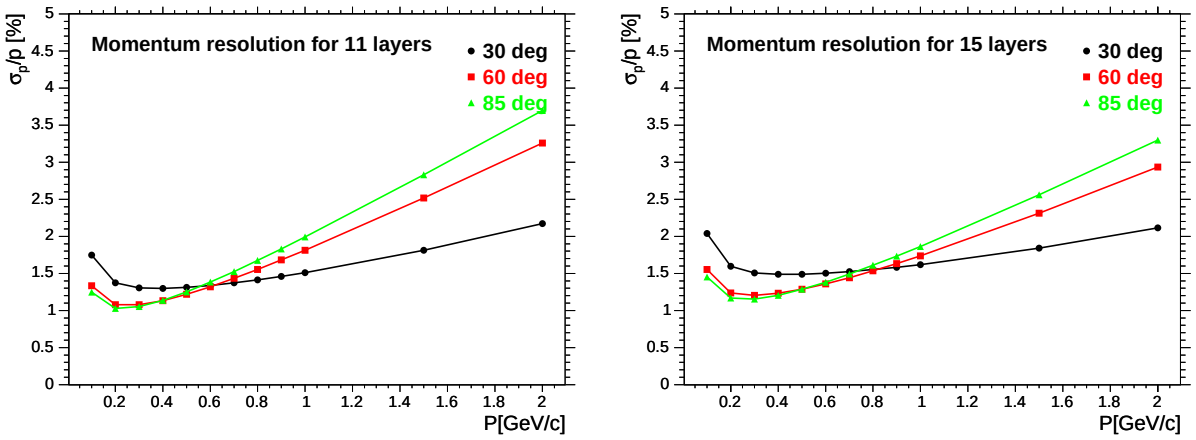

(a) momentum resolution for 11 layers (b) momentum resolution for 15 layers

Figure 4.14: Estimation of the total momentum resolution for the STT a) with 11 double layers and b) 15 double layers for different polar angles.

of the vertex position to the fit duplicates the lever arm, enhances the angular precision in $\sigma^{vertex}_{STT}/\sigma^{vertex}_{MVD} = 400\mu\text{m}/20\mu\text{m} = 20$ times and significantly improves the situation with the total momentum resolution as it shown on Fig. 4.15.

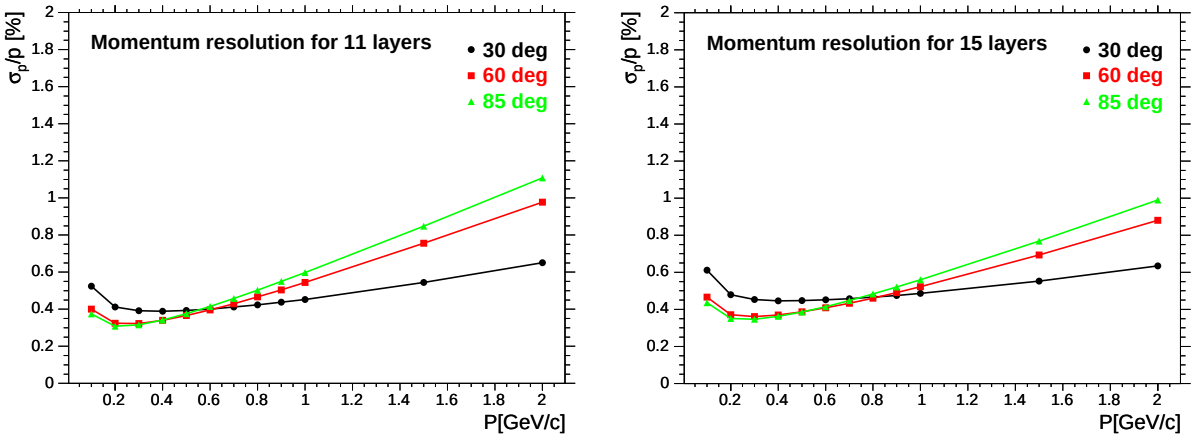

(a) momentum resolution for 11 layers (b) momentum resolution for 15 layers

Figure 4.15: Estimation of the total momentum resolution for the STT together with the MVD for different polar angles. On the figure a) the STT has 11 double layers and 15 double layers on figure b).

The model estimations for the momentum resolution have been confirmed with a good precision by Monte Carlo simulations of $\overline{\text{P}}$ANDA detector (see Fig. 4.16). Fig. 4.17 shows

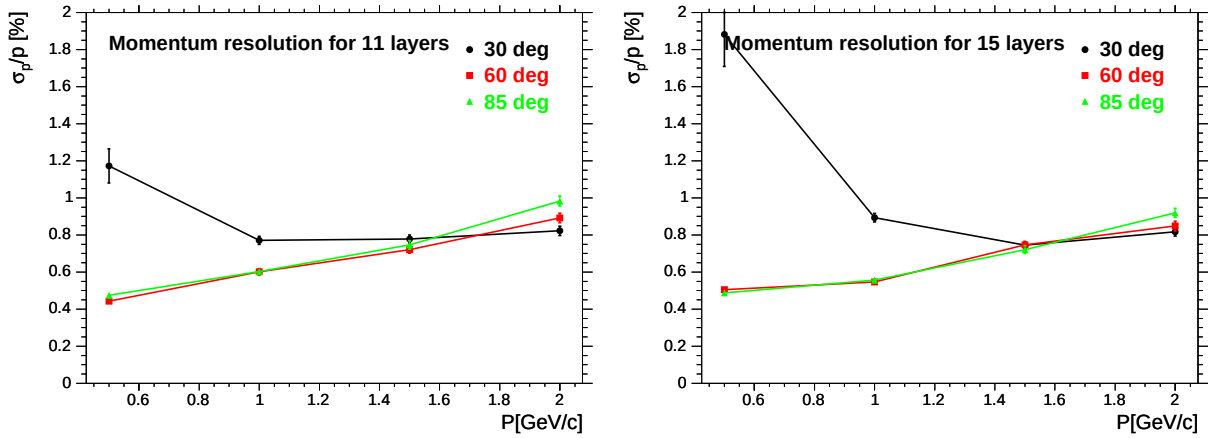

(a) momentum resolution for 11 double layers (b) momentum resolution for 15 double layers

Figure 4.16: The total momentum resolution of the $\overline{\text{P}}$ANDA tracker from Monte-Carlo simulation for different polar angles. On the figure a) the STT has 11 double layers and 15 double layers on figure b). The first point on the resolution plot for 30 degrees has much bigger value due to fitting routine failure[2].

also the rather good angular resolution of the **CT**. All this consideration should be taken into account during the selection process for the STT layout. Also some details of the straw tube construction, which are important for the final choice, are discussing in the next sections.

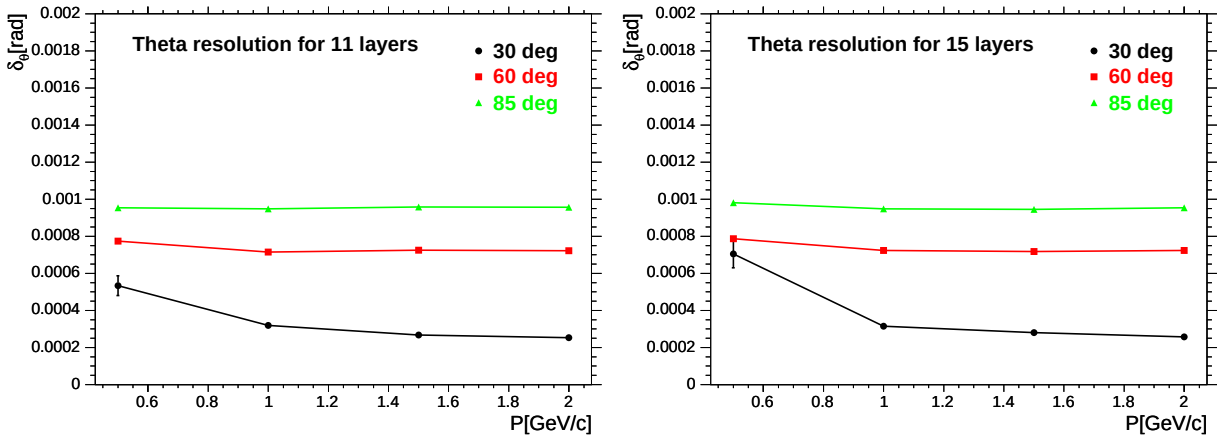

(a) angular resolution for 11 double layers (b) angular resolution for 15 double layers

Figure 4.17: The polar angle resolution of the $\overline{\text{P}}$ANDA tracker from Monte-Carlo simulation for different polar angles. On the figure a) the STT has 11 double layers and 15 double layers on figure b).

4.2.2.1 Straw tubes

Straw tubes are gas-filled cylindrical tubes with a conductive inner layer as cathode containing a stretched sense wire along the cylinder axis. Straw is made of two thin metallized plastic foil strips (e.g. 12 μm thick, 16 mm wide mylar film) are glued together with a half-overlap. Another method of the straw production is ultrasonic welding(see [16],[6]), when the straw is made of one mylar strip, wounded on the smooth steel rod with a small overlap, about 2-3 mm. and welded along overlap using ultrasonic welding tool. Such method allows to make the straw wall thinner. At present time straws are widely used to build up large hodoscopes for particle tracking (Table 4.4).

More about basic principles of the straw tube operation and getting the position information one can find in Chap. 5.

High momentum resolution tracking requires minimal scattering and energy loss of passing tracks. In addition, the high particle rate up to 10^8 per second needs a high suppression of secondary background by interactions with the detector material. Table 4.5 lists the thickness (X) in radiation lengths (X_0) of the different components of a straw tube. The main contribution comes from the film thickness. If thinnest ($d \sim 30\,\mu$m) film tubes are used, a total detector thickness of $X/X_0 \simeq 1\%$ is feasible.

Table 4.5: Mean thickness (in radiation lengths) of the different straw tube components for orthogonal incident tracks. The last number is the sum for 11 double layers which is one of the option discussed for a $\overline{\text{P}}$ANDA straw tracker.

Element	Material/Thickness	X $[mm]$	X_0 $[cm]$	$\frac{X}{X_0}$
Film Tube	Mylar, 30μm	0.1	28.7	$3.5{\cdot}10^{-4}$
Coating	Al, 0.1 μm	$3{\times}10^{-4}$	8.9	$3.5{\cdot}10^{-6}$
Gas	Ar/CO_2 (80/20%, NTP)	7.85	11933	$6.6{\cdot}10^{-5}$
Wire	W/Re, 20μm	$3{\cdot}10^{-5}$	0.35	$8.6{\times}10^{-6}$
			$\sum_{straw}$	$4.3{\cdot}10^{-4}$
		$\sum_{(11 double-layers)}$		0.009

Straw Cathode Material Straw tubes are normally made from thin plastic foils (polyester Mylar [17], polyimide Kapton [18]) coated with conducting layers (aluminum, copper. etc.).

Mylar has better mechanical properties than Kapton (see Table 4.6) and has a lower permeability. On the other hand, Kapton can be loaded with carbon resulting in a slightly conductive material (Kapton XC by DuPont). This is extremely useful for building robust straw tubes avoiding the risk of damaging the conductive coating. When the tubes are operated inside high radiation environments, coating can be dissolved by free radicals. This is not the case with Kapton XC - the conducting property proceeds via the bulk material and cannot be easily damaged. But it should be noted, that it may increase the wall thickness of the straws and, as a consequence, lead to the momentum resolution deterioration (cf. Fig. 4.16 and Fig. 4.18).

Table 4.6: Compilation of Mylar and Kapton properties.

	Mylar	Kapton
Young's modulus [N/mm^2]	4.500	2.400
Tensile strength [N/mm^2]	196	165
Moisture absorption	0.8%	4%

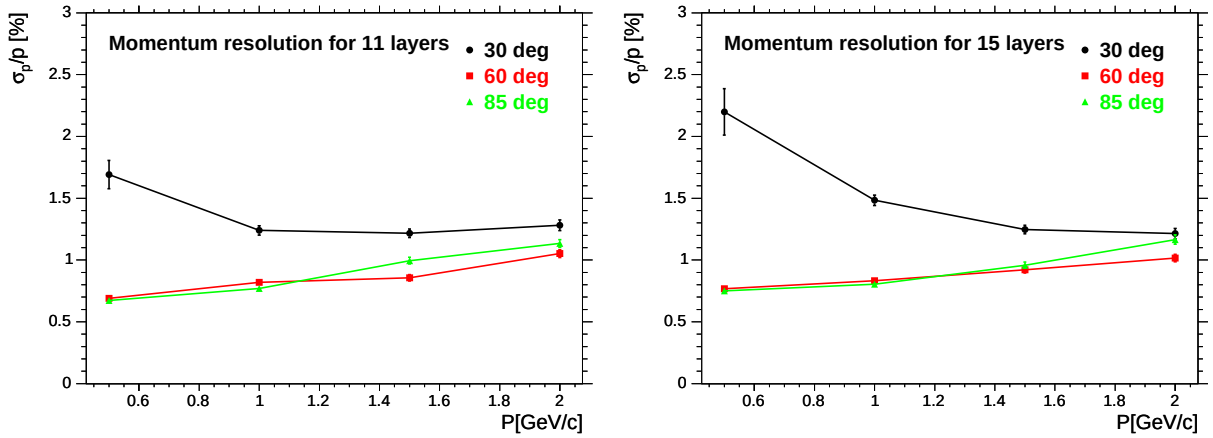

(a) momentum resolution for 11 double layers

(b) momentum resolution for 15 double layers

Figure 4.18: The total momentum resolution of the $\overline{\text{P}}$ANDA tracker from Monte-Carlo simulation for different polar angles. On the figure (a) the STT has 11 double layers and 15 double layers on figure (b). The straw tube wall thickness is 90 mum

Wire Tension Both efficiency and resolution of a straw are best for a perfect cylindrical shape of the film tube and the wire being exactly located along the cylinder axis. However, due to the gravitational and electrostatic forces the wire and straw centers do not coincide. The gravitational sag of the wire, denoted by δ is given by:

$$\delta = \frac{ML}{8T}, \tag{4.3}$$

where M and T are the wire mass and tension[3] in grams, L is the wire length. With a wire tension of about 50 g inside a 1.5 m long, horizontal straw tube the maximum sag due to gravitation in the tube center is $\sim 35\,\mu$m. The critical wire tension, which may lead to the wire breakup, can be determined from Fig. 4.19 (a). It can be seen that for the commonly used type of wires of 20 μm diameters, with 3% percents of Re, the irreversible plastic deformations of the wire begins at the tension $\sim 70\,g$, while for the same diameter wire with 18% of Re the tension up to $\sim 110\,g$ can be applied. The straw tube itself has a gravitational sag, which also can be calculated using the formula 4.3. The typical value of the gravitational sag of the straw is several hundred of microns, depend on straw diameter and tension, which leads to even bigger eccentricity of the anode wire. In own turn, the electric field acting on an eccentric wire will induce an additional bending depending on

[3]Usually given as the mass weight used to stretch the wire.

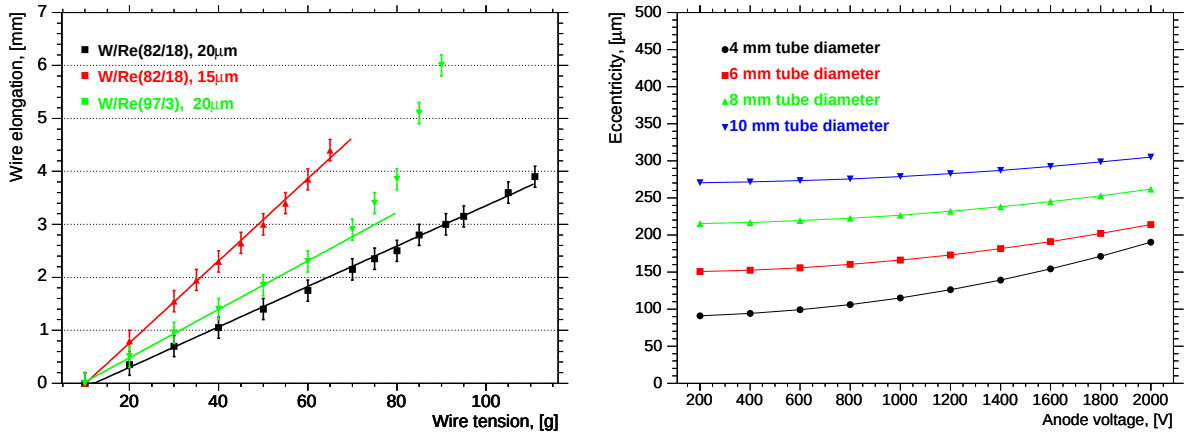

(a) anode wire elongation

(b) anode wire eccentricity

Figure 4.19: On the figure a) the anode wires elongation due to applied tension is shown for different wire materials and diameters. On the figure b) the anode wire eccentricity depending on a straw tube diameter and applied voltage is shown.

the actual voltage applied to the wire:

$$\delta_1 = \frac{\pi\epsilon_0 \Delta L^2 V^2}{4TR^2[\ln(R/r)]^2}, \tag{4.4}$$

where ϵ_0 is permitivity of free space, Δ is a shift of the wire from tube center due to difference in the gravitational sags of the wire and the straw, L is the tube length, V is applied anode voltage, T is the wire tension, R and r are the radii of the tube and the wire. On the Fig. 4.19 (b) the total anode wire eccentricity is shown as a function of applied voltage for different straw tube diameters. As one can notice that the anode wire in straws of 4 mm diameter, as well as 6 mm straws, shows an instability at higher values of the anode voltage. Installation of the special spacers, holding the wire in the central position, is required for compensating this effect. It unavoidable leads to the significant complication of the whole straws design. Because of that, usage of straws of 8 mm and 10 mm diameters is preferable.

4.2.3 Straw Chamber Design

The $\overline{\text{P}}$ANDA STT will consist of up to 8000 straw tubes, each 150 cm long , packed in a set of cylindrically-bent double-layers with increasing radius from 15 cm to 42 cm, around the beam pipe.

For 8000 straws this would add up to a tension equivalent to about 400 kg which must be maintained, as well a tension of the straws itself. Usually, this is done by fixing the straw tubes inside a strong and massive supporting frame. This will inevitably increase the detector thickness given in radiation length by this additional materials.

At the moment two different design options are foreseen. A more common design uses layers, skewed with respect to each other by a small ($\sim 2-4^o$) angle to obtain the track coordinate along the wire by the crossing tube position. Such straw trackers are

installed in the WASA [10] and FINUDA [9] detectors. The advantage of a relatively high z-resolution ($\sigma_z \sim mm$) is accompanied by several disadvantages, including reduced geometrical symmetry and acceptance (open gaps), and smaller mechanical stability due to the hyperbolic layer shape. The latter also requires additional support structures to align the tubes over the full length.

In the second case, more symmetric and mechanically robust tracker layout would consist of close-packed, cylindrical layers of straw tubes, exactly parallel to the beam and magnet axis. Here, the layers can be made highly self-supporting, using a gas over-pressure to straighten the straws and to keep the wire tension. Because of that, tracker, built using such technique, requires only mechanical support structures, to pickup the detector and the electronics weight and align the tubes over their full length. Such a new technique has been developed at FZ Jüelich-IKP to reduce the overall detector weight to an absolute minimum [19]. The straw tracker, based on this technique, will upgrade the COSY-TOF experiment [13] and consists of 15 planar double-layers of close-packed straw tubes bond together at few points. To obtain the track coordinate along the wires, the charge division method can be used (see Sec. 5.3). This method needs dedicated studies and optimization of wire materials (resistivity) and electronic charge amplitude readout. The first 150 cm long straw tubes with different anode wire resistivity have been assembled at FZ Jüelich-IKP (Sec. **??**) to start the prototype studies.

In any case each cylinder-set should be split into 2 halves to provide mounting around the beam pipe. Also, a few cm space for the vertical target pipe must be left, by taking shorter straws in this area. All electronic readout, gas and high-voltage supply will be located at the upstream end of the detector.

4.2.4 Summary

A straw tracker has several advantages compared to conventional drift chambers due to the highly symmetric, cylindrical shape of a drift tube:

- robust electrostatic configuration. The shielding tube around each high voltage wire suppresses signal cross-talk and protects neighboring straws in case of a broken wire;
- robust mechanical stability if the straws are arranged in close-packed multi-layers;
- high spatial resolution, $\sigma_{r\varphi} < 150\,\mu$m, depending on tube diameter and gas characteristics. Simple calibration of space-drift time relation due to the highly symmetric, cylindrical, isochronous shape;
- small radiation length, $X/X_0 \sim 0.05\%$ per tube, if straws with thinnest (30 μm) film tubes are used;
- high rate capability due to small drift path and possibility to use a fast drift gas[4].

[4]The significant increasing of the drift time in the strong magnetic field should be taken into account. For more details see Sec. 5.1.1.

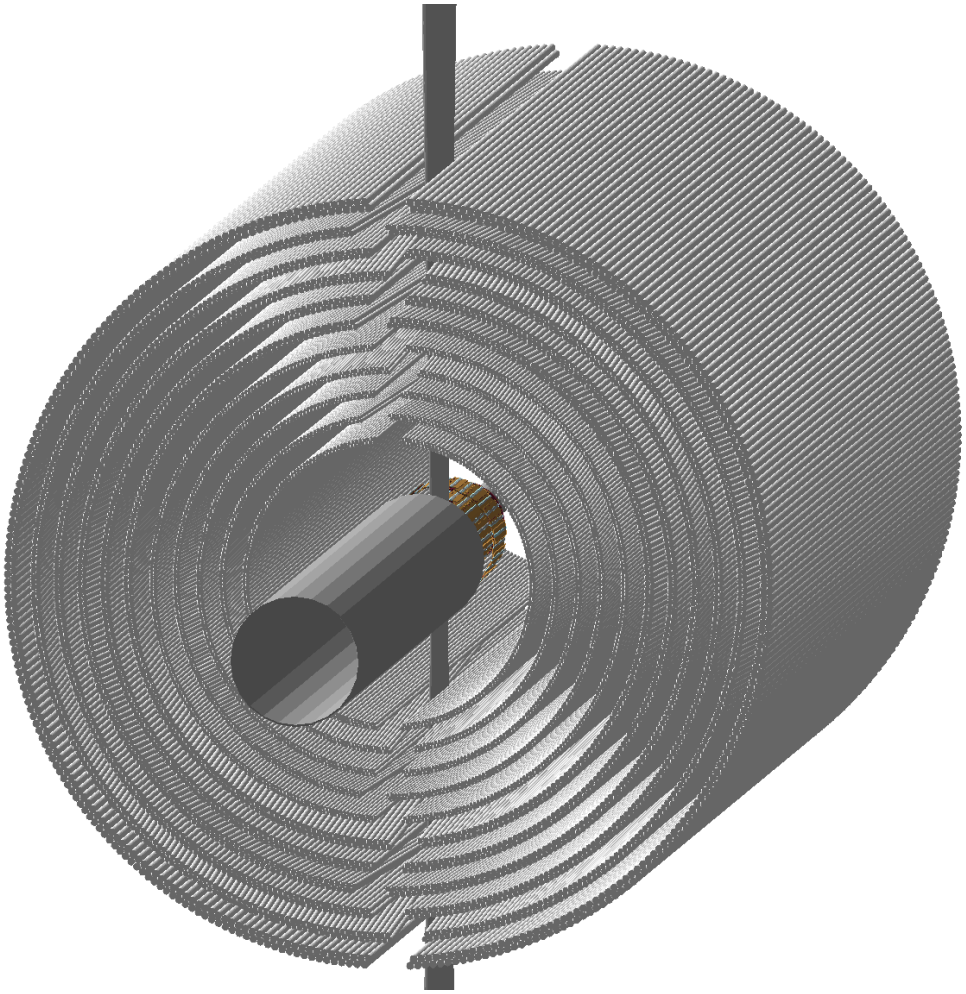

Figure 4.20: View of STT with 11 double layers.

The final choice of the STT geometry is not yet done. Monte Carlo simulations have been performed varying not only the cathode thickness but also the number of layers in order to find the setup that warrants the best momentum resolution at minimal material budget. Based on results of this simulations, the self-supporting construction with 11 double layers looks preferable. If it necessary, five of double layers can be skewed to improve Z-coordinate resolution. Other double layers will be straight using the charge division method to get coordinate along the tube. Such geometry will make the on-line track finding and fitting much easier. The straw tube diameters can be 8 mm for inner and 10 mm for outer layers, although simulations of detector occupancy are needed for the final solution. Layout with 11 double layers is shown on Fig. 3.9 and Fig. 4.20.

References

[1] BaBar Technical Design Report, Technical report, SLAC, 1995.

[2] S. Aubert et al., Nucl. Inst. Meth. **A479**, 1 (2002).

[3] Conceptual Desighn Report, http://www-new.gsi.de/GSI-Future/cdr/, Technical report, FAIR/GSI, 2002.

[4] ALICE Technical Design Report, Technical report, 1999, CERN LHCC 99-12.

[5] R. Gluckstern, NIM **24**, 381 (1963).

[6] V. Anashin et al., NIM A **478**, 420 (2002).

[7] C. Brand et al., NIM A **283**, 567 (1989).

[8] C. Brand et al., NIM A **367**, 129 (1995).

[9] L. Benussi et al., Nucl. Phys. **A419**, 648 (1998).

[10] R. Bilger et al., Nucl. Phys. **A663&664**, 1073c (2000).

[11] V. Aulchenko et al., NIM A **283**, 528 (1989).

[12] V. N. Bychkov et al., Part. and Nucl. Lett. **2**, 111 (2002).

[13] M. Abdel-Bary et al., Phys. Lett **B595**, 127 (2004).

[14] CERN/LHCC-98-004, 1998.

[15] http://www-btev.fnal.gov/DocDB/0000/000032/002/ptdr.html, 1999.

[16] V. Aulchenko et al., Mylar drift tubes for tracking, Technical report, BINP Preprint 84-166, 1984.

[17] Mylar, poliester film, registered trademark of DuPont, www.dupont.com.

[18] Kapton, polyimide film, registered trademark of DuPont, www.dupont.com.

[19] P. Wintz et al., in *AIP conf. Proc.*, volume 698, page 789, 2004.

Chapter 5

Physics of a single straw tube

The straw tube represents a sort of a proportional counter - the gas filled cylindrical tubes with a conductive inner layer as cathode containing a stretched sense wire along the cylinder axis. Electrons of the primary ionization, produced in the gas medium by traversing particles, are drifting towards field lines to the anode. Due to the high electric field tension in vicinity of the thin anode wire, an energy of drifting electrons became high enough to produce secondary ionization. That process is called an avalanche gas amplification. Thanks to the avalanche amplification the charge, collecting on the anode, can be on several order of magnitude higher than the initial primary ionization. Because of that the signal from such avalanche can be easily detected by the relatively simple electronics.

Measurement of a drift time, uniquely connected with the distance to the track, allows to reconstruct of the transversal track coordinate. The longitudinal coordinate can be obtained by the measurement the charge sharing between the straw ends and/or the difference of arrival times of the signals.

The short rewiev of the main physics processes inside the straw and the limiting factors of the straw spatial resolution is given below.

5.1 Basic physics principles of the cylindrical proportional counter.

5.1.1 Formation and drift of the ionization.

Charged relativistic particle loses a part of its energy in interactions with the detector medium. An expression for the average energy loss due to Coulomb interaction has been obtained by the Bethe and Bloch in the framework of the relativistic quantum mechanics. For simpler and clearer explanation of the process it is convenient to use the free electron approximation [1]. Probability P to release of an electron with the energy E is given by:

$$\frac{dP(E)}{dEdx} = \frac{1}{E^2}\frac{2\pi N_A Z \rho e^4}{m_e c^2 A \beta^2}, \tag{5.1}$$

where Z, ρ, A are the average number of electrons in atoms, the density and the atomic number of a medium, correspondingly, m_e, e - the charge and the mass of an electron. Energy dependence emphasizes the low energy transfer dominating and most of ejected electrons fly away only on a small distance, although they are mostly emitted perpendicularly to the particle trajectory. Such electrons, ejected with an energy above few keV, are called δ-electrons. They are promptly stop in the gas medium, and some of them, having enough energy for secondary ionization, produce a charged cluster around themselves. For argon, for example, the number of electrons ejected in 1 cm with the energy more then E_0 is [2]:

$$N(E \geq E_0) = \frac{115eV}{E_0}. \tag{5.2}$$

For energies up to few hundred MeV the δ-electrons range can be approximated, in g/cm^2, by [3]:

$$R_p = 0.71E^{1.72}, \tag{5.3}$$

where E is δ-electron energy in MeV.

Combining 5.2 and 5.3 one can deduce, that in 1 cm of argon, one out of five minimum ionizing particles eject a δ-electron having a range 10μm and only one out of twenty particles can produce a 3 keV electron having a range more than 100μm. Thus, the cluster positions locate the track with the high precision.

Some properties of the most useful gases and gas mixtures are given in the Table 5.1. As

Table 5.1: Properties of different gases and gas mixtures. Z and A are charge and atomic weight, for molecules the total number have to be taken, N_p and N_t are the number of primary and total electron pairs per cm, respectively, E_x and E_i are the excitation and ionization energy, respectively, W_i is the average energy required to produce one electron-ion pair in the gas, $(dE/dX)_{mip}$ is the most probable energy loss by a minimum ionizing particle and X_0 is an radiation length. For gas mixtures, weighted average value for N_p ,N_t, E_x ,E_i, W_i, $(dE/dX)_{mip}$ and X_0 have to be taken.

Gas or gas mixture	Z	A	E_x[eV]	E_i[eV]	W_i[eV]	(dE/dX) [keV/cm]	N_p[1/cm]	N_t[1/cm]	X_0[m]
He	2	4	19.8	24.5	41	0.32	4.2	8	5299
Ar	18	40	11.6	15.7	26	2.44	23	94	110
CO_2	22	44	5.2	13.7	33	3.01	35.5	91	183
i-C_4H_{10}	34	58	6.5	10.6	23	5.93	84	195	169
Ar-10%CO_2	-	-	-	-	26.7	2.5	24.6	93	117
He-10%i-C_4H_{10}	-	-	-	-	39.2	0.88	12.7	26.7	1313
He-20%i-C_4H_{10}	-	-	-	-	37.4	1.44	20.6	45.4	749

it was already mentioned some of δ-electrons can produce clusters of charges. As one can calculates from the Table 5.1, an average number of electrons in cluster - N_t/N_p equals 2-3. However, due to the energy distribution of the primary electrons, only a small fraction

of the clusters have more than 1 electron. For example, in argon about 80% of all clusters consist of 1 electron [4].

In the electric field electron and ions starts to drift along the field lines. Electron drift velocity determines an arrival time to the anode. The electron's movement in the electric field can be represents as superposition of the average drift movement, which has certain velocity, and chaotic movement around average position, which leads to the charge cluster diffusion. Up to date there are a lot of experimental data on the drift velocity and diffusion in different gas mixtures [5] and satisfactory model for numerical calculations has been created [6]. Moreover, the drift velocity can be determined from the self-calibrating procedure, as it described in Sec. **??**.

It's useful to separate two essentially different situations. In the weak electric field or in the gas mixtures, which can effectively quench an electron kinetic energy, latter can't get an additional energy between collision, comparable with the average thermal energy of 0.025 eV. In that case, electrons are in the thermal equilibrium with the surrounding medium and the its drift velocity proportional to the electric field tension. Such gases are usually called "cold" for the given electric field strength.

On the contrary, if the electron average kinetic energy differs from the thermal energy, the drift velocity behavior becomes more complicated. In many gas mixtures the drift velocity became saturated and don't depend on an electric field strength and, therefore, from the distance to the straw anode. That removes the main sources of systematic errors and makes a reconstruction of the track coordinate easier. Also the highly saturated drift velocity reduces the "dead" time of he chamber, allows, for example, include the coordinate information into the trigger logic. From other hand, the high spatial resolution in the "hot" gas mixtures is limited in principle due to the large diffusion and can't be less than $\sim 50\,\mu$m.

For instance, on the Fig. 5.1 Ramsauer cross sections for the CO_2 and Ar [7] are shown. As one can notice the cross section for CO_2 two order of magnitude higher in the thermal

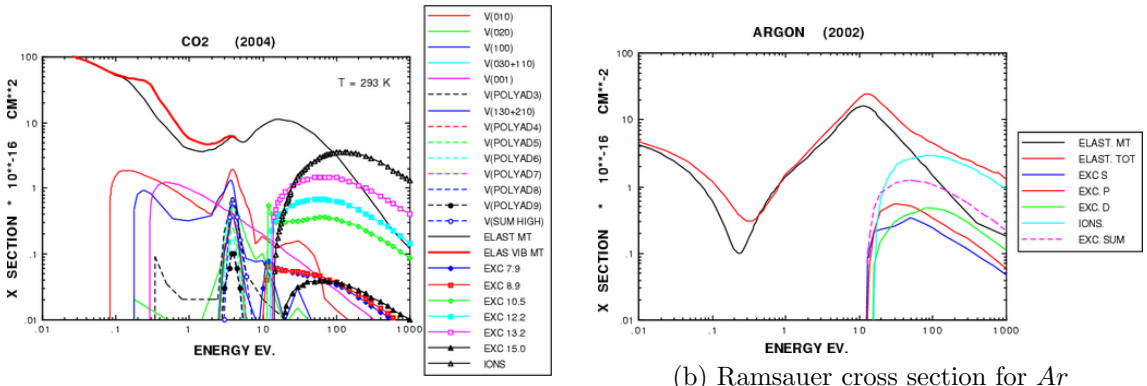

(a) Ramsauer cross section for CO_2

(b) Ramsauer cross section for Ar

Figure 5.1: Ramsauer cross sections for the "cold" CO_2 (a) and the "hot" Ar (b) gases are shown.

energy region and relatively flat compare to the Ar cross section, which has the deep minimum around 0.3 eV. Because of that in the pure CO_2 electrons have a thermal energy

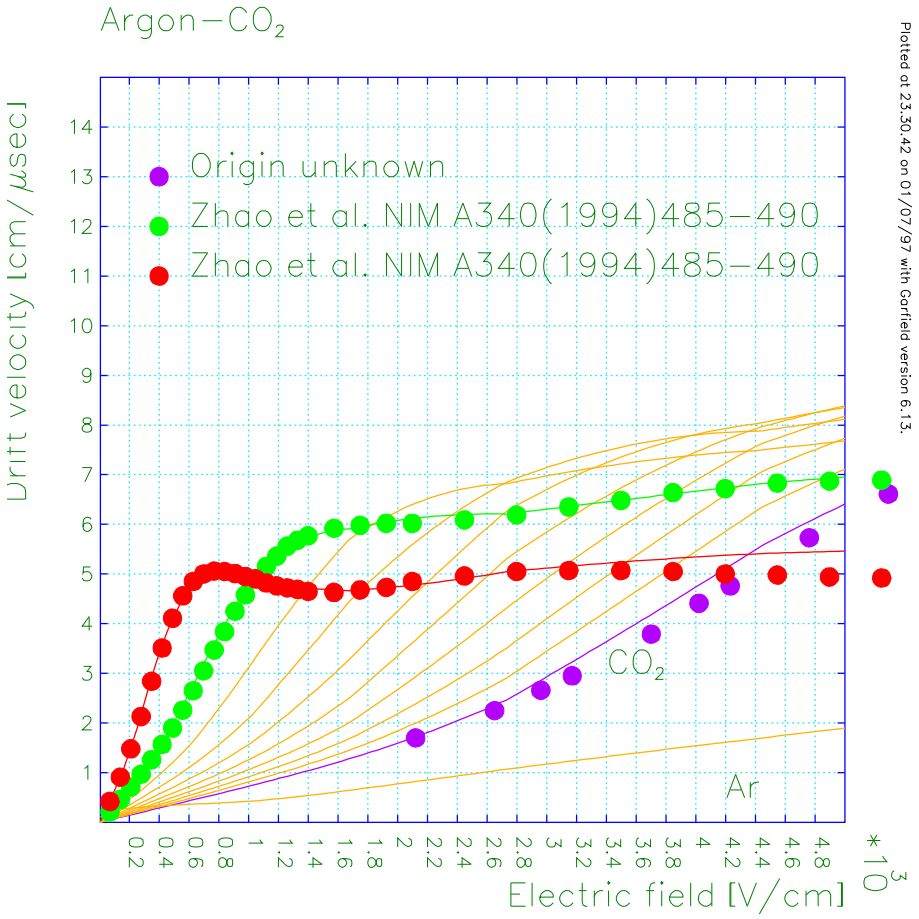

Figure 5.2: Drift velocity of electrons in $Ar - CO_2$ gas mixtures.

and, therefore, small drift velocity, whereas in Ar-based gas mixtures[1] they are speeding up quickly up to the energies about 1 eV [2]. That can be clearly seen on the Fig. 5.2, where the drift velocity in argon with 10% of CO_2 is saturated already at 600 V/cm, while for pure CO_2 the saturation is not achieved even at 5 kV/cm.

In the presence of a magnetic field the drift properties are changing. The Lorentz force applied to each moving charge transforms the small segment of motion between two collisions into circular trajectories. Practically speaking, the changes are coming down to the following - an electron swarm is moving with the average velocity v_m and at an angle α_m to the electric field direction as follows [8]:

$$v_m = \frac{v(E, \tau_m)}{1 + \omega^2 \tau_m^2}, \quad \tan \alpha_m = \omega \tau_m, \quad \tau_m = \tau(E, H), \tag{5.4}$$

where τ is the average time between collisions, $\omega = eB/m$ is the Larmor frequency of the electron. Herewith, the approximation $\tau_m = \tau(E, H = 0)$ appears to be precise enough.

[1] It should be noted that in pure Ar electrons energy stays in the thermal region, probably due to the relative flat cross section behavior at the small energies.

In that case one can take τ from equation:

$$v_{drift} = \frac{eE\tau}{m}. \tag{5.5}$$

It's easy to see, when dependency of $v_{drift}(E)$ from E is linear then τ is a constant, while if $v_{drift}(E)$ saturates then τ is inversely proportional to E.

The full drift time T is:

$$T = \int_a^b \frac{dr}{v_m(r)} = \int_a^b \frac{1+\omega^2\tau^2}{v(r)}dr = T_0 + \omega^2 \cdot \int_a^b \frac{\tau(r)^2}{v(r)}dr. \tag{5.6}$$

Because in "cold" gases τ is constant almost in the whole chamber volume, one can get:

$$T = T_0(1+\omega^2\tau^2), \tag{5.7}$$

In "hot" gases, on the contrary, the drift velocity is constant, because of that integration gives:

$$T = T_0(1+\frac{\omega^2\tau_0^2}{3}), \tag{5.8}$$

where τ_0 is a time between collisions at maximum distance from the anode. At first glance seems, that in "cold" gases the drift time augmentation is larger, but that's not a true. Due to the much lower elastic cross section (cf. Fig. 5.1) the time between collisions τ in the "hot" gases is approximately one order of magnitude higher. Estimations, made from experimental data, shows that, for the magnetic field of 2 T and the drift distance of 5 mm, the drift time for the CO_2+10% $i-C_4H_{10}$ increases only on 15%, while for the Ar+10%CO_2 gas mixture an augmentation will be 50% already. It should be noted that in latter case the Lorentz angle near the cathode will be about 50^o.

5.1.2 Gas amplification.

Electrons of primary ionization, arriving to the anode wire, gets into the very high electric field region. At the wire surface an electric field tension reaches of value several tens or even hundreds of kV/cm. In such strong electric field electrons can receive enough energy between two collisions to produce inelastic phenomena, excitation or ionization. Secondary electrons, in own turn, can also produce ionization etc. As result a typical drop-like avalanche develops with all electrons in the front and ions behind. A typical view of the single electron avalanche is shown on the Fig. 5.3. Ionization probability P is determined by the *Townsend* coefficient (see Fig. 5.4) $\alpha(x)$ for the give gas, an can be written as follows:

$$dP = \alpha(x)dx \tag{5.9}$$

Because of that an average number of the secondary electrons, produced by the one primary electron or the multiplication factor M, is:

$$M = exp\Big(\int_a^x \alpha(x)dx\Big), \tag{5.10}$$

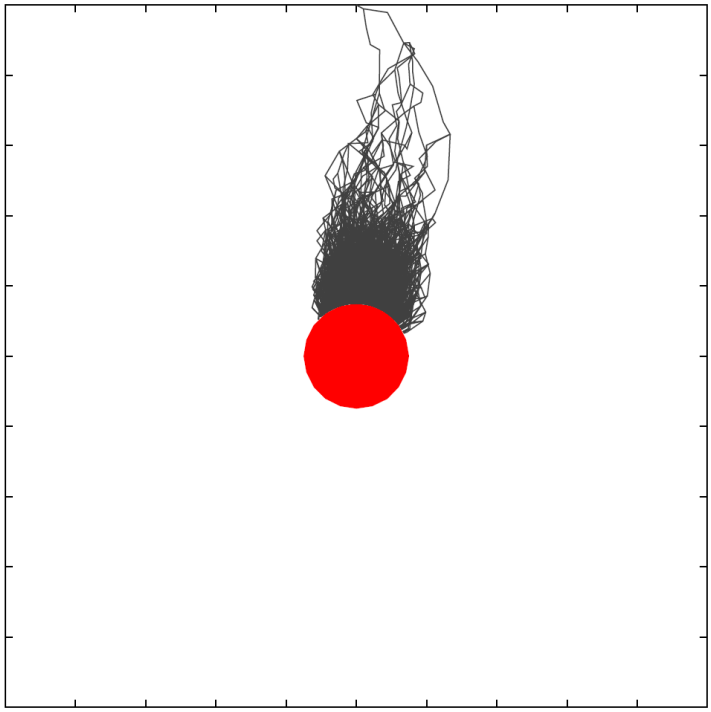

Figure 5.3: Typical view of the single electron avalanche in the straw tube. Gas gain approximately 27 000. The figure is taken from [9].

where a is the anode wire radius and the integral is taken along the whole drift path. Townsend coefficient $\alpha(x)$ has a physics meaning of the inverse free mean path for ionization and correspondent dimension.

Assuming that electric field E inside the straw tube depend on r as:

$$E(r) = \frac{U_0}{\ln(b/a)r}, \tag{5.11}$$

where U_0 is the anode voltage, a and b are radii of the anode and the cathode, correspondingly, one can get the good approximation for M by determination of the certain avalanche development region r_{cr} from the condition:

$$W_i = eE(r_{cr})\lambda(r_{cr}) = \frac{eU_0}{\ln(b/a)}\frac{\lambda(r_{cr})}{r_{cr}} \quad \Longrightarrow r_{cr} = \frac{eU_0\lambda(r_{cr})}{W_i \ln(b/a)}, \tag{5.12}$$

where W_i is the average ionization energy (see Table 5.1). Taking 5.12 into account one can writes M as following:

$$M = exp\Big(\int_a^{r_{cr}} \frac{dr}{\lambda(r)}\Big). \tag{5.13}$$

Typical behavior of the gas gain is shown on the Fig. 5.5. In the proportional region the slope of the gas gain, depend on applied voltage, should be constant (see Fig. 5.5). Indeed the slope depend on only form W_i:

$$\frac{d\ln(M)}{dU} = \frac{e}{W_i \ln(b/a)}, \tag{5.14}$$

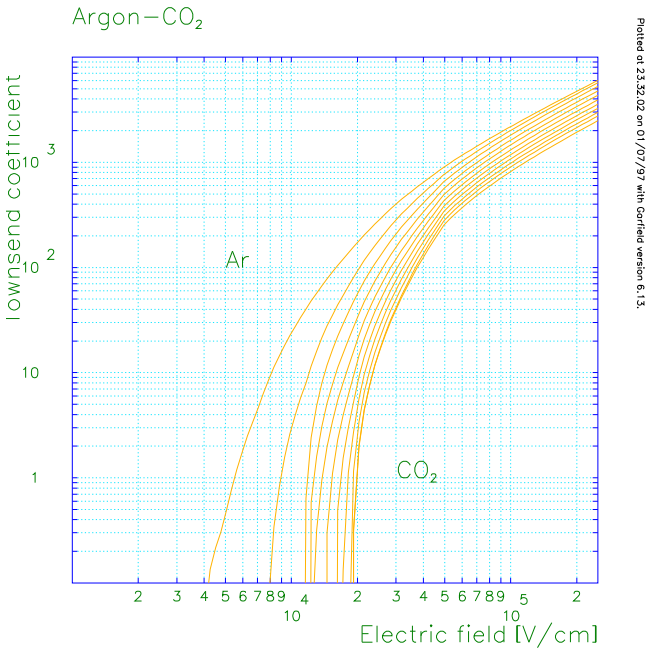

Figure 5.4: Townsend coefficients for different $Ar+CO_2$ gas mixtures.

Value of W_i calculated from the slope on the Fig. 5.5 is $\sim 20\,eV$, which is in the good agreement with the tabular value of $22\,eV$. For the higher gas gain (more than 10^6) the proportionality between the primary ionization and the number of electrons in avalanche is lost, as a consequence of the electric field distortions due to the large space charge produced in the avalanche. Such region of the gain curve is called the region of limited proportionality [2].

The high spatial resolution in the straw tube requires the high amplitude anode signals even for the single electron clusters. It requires the high gas gain. The maximum gas amplification in the straw tubes restricted by the following factors:

- development of the Geiger discharge, especially in the presence of the highly ionizing particles;
- development of the secondary pulses from electrons emitted from cathode;
- high voltage resistance of construction;
- appearance of fake hits, due to cross talks in adjacent electronic channels.

Also the high gas gain significantly reduce the chamber lifetime. For the optimum gas amplification choice all this factor should be taken into account properly.

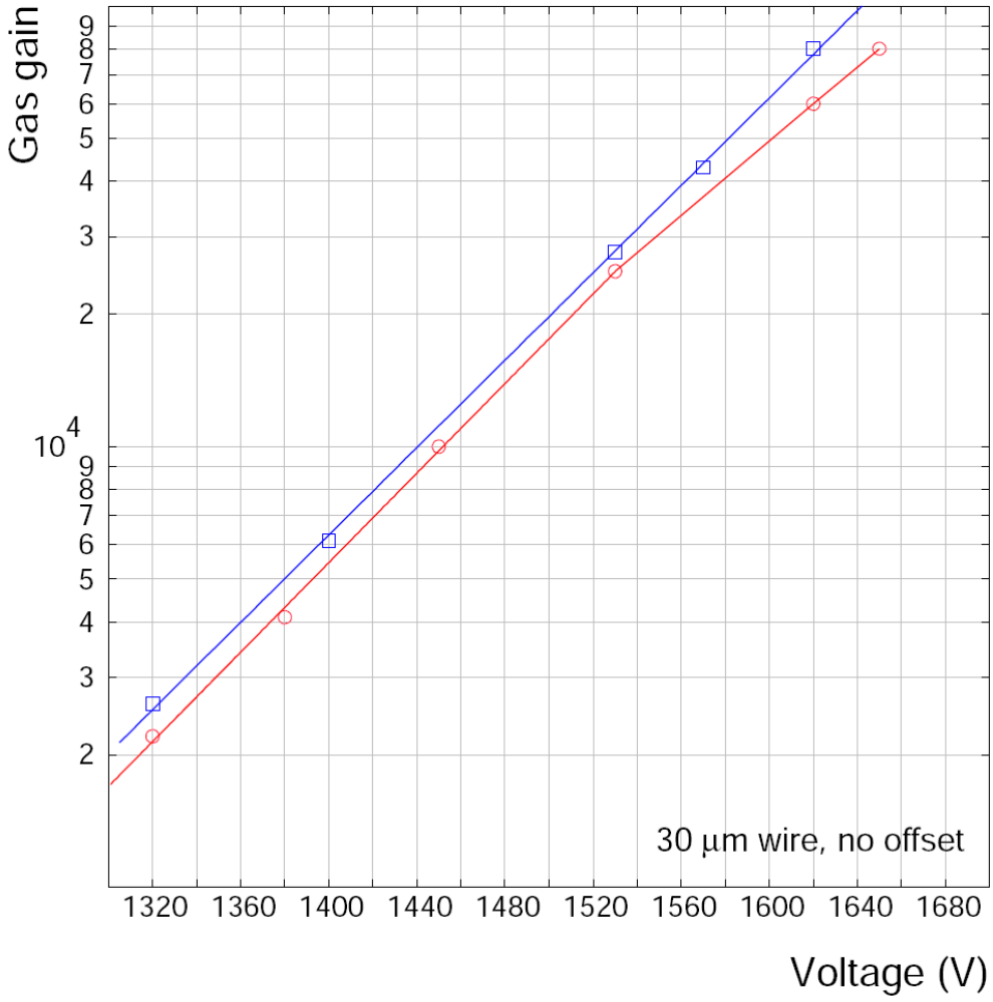

Figure 5.5: The gas amplification in the ATLAS TRT. The gas mixture is $Xe/CF_4/CO_2 70/20/10$. Experimental and Monte-Carlo data are shown. The figure is taken from [9].

The gas gain fluctuations in wire chambers are significant. Distribution of the fluctuations is described by *Polya* law [10]:

$$P(M) = \frac{M^{\theta}(1+\theta)}{\overline{M}^{1+\theta}} \cdot exp(-(1+\theta)M/\overline{M}), \quad RMS = \frac{\overline{M}}{1+\theta}, \tag{5.15}$$

where θ is a small parameter $0 \leq \theta < 0.6$. For the small M $\theta \to 0$ and distribution has an exponential view:

$$P(M) = (M/\overline{M})exp(-M/\overline{M}). \tag{5.16}$$

5.1.3 Factors limiting the spatial resolution.

5.1.3.1 Drift velocity.

The average drift velocity of electrons is uniquely determined in the each spatial point by the gas medium conditions and the electric field strength. For the good spatial resolution it is important to know the drift velocity with the high accuracy. The systematic error can appears by conversion of the time information into coordinates due to weak variations of the temperature, the pressure, the gas mixture composition etc. The best remedy against the global changes of the drift characteristic is a possibility of the self-calibration procedure, which is one of the features of the straw tube Sec. **??**.

Independent from possibility of the self-calibration, the monitoring system for all parameters of the gas mixture have to be foreseen.

5.1.3.2 Diffusion.

Spreading of the drifting swarm of electrons is characterized by the diffusion coefficient D

$$d\sigma^2 = 2Ddt = \frac{2k\epsilon dx}{eE}, \tag{5.17}$$

where ϵ is the average energy of moving electrons, E is the electric field tension. In "cold" gases $\epsilon = T$ and expression

$$\sigma_x = \sqrt{\frac{2kTx}{eE}}, \tag{5.18}$$

is called the thermal limit of diffusion.

Accuracy of localization of the drifting electron cluster depends on the number of electrons in the cluster and the registration electronics threshold. By convention, an optimal strategy of the time measurement for the small cell is the time determination by the leading signal edge with the equivalent threshold lower than one electron [11]. In that case, a contribution of the diffusion into the spatial resolution is [2]

$$\sigma = \frac{0.9}{\sqrt{\ln(N)}}\sigma_x, \tag{5.19}$$

where N is the number of electrons, pretending to start of discriminator. For distant tracks that number is order of 5-10, depend on gas mixture and $\sigma = (0.6 \div 0.7)\sigma_x$.

For the diffusion reduction it's necessary to reduce an electron temperature and/or increase the pressure. In the "cold" gases, diffusion is isotropic. In the "hot" gases, together with the energy increasing, an effect of the longitudinal diffusion reduction appears. However, even take into account that effect, diffusion still is too big (see Fig. 5.6).

Usage of "cold" gas mixtures gives a possibility to move down below 100 μm by the spatial resolution, but the price to pay is necessity of delicate measurement of the drift velocity and precision control of temperature and pressure.

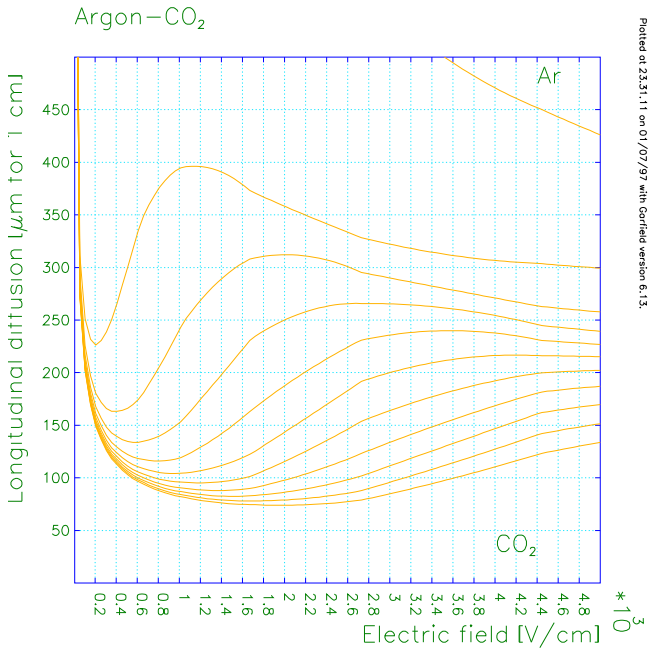

Figure 5.6: Longitudinal diffusion for different $Ar+CO_2$ gas mixtures.

5.1.3.3 Statistic of the primary ionization (cluster-effect).

Discretisation of the charge distribution along the particle trajectory leads to the significant errors in the reconstruction of the distance, specially for particles passed near the anode wire. For particle crossed the anode wire in the straw, filled with $Ar+10\%CO_2$ gas mixture, with the average distance between the clusters of $\sim 330\mu$m, the average measured distance will be $330\,\mu\text{m}/(2\sqrt{12}) \simeq 50\,\mu$m. The resolution drop in the region of the small drift distances is called "cluster-effect".

This effect is worsened by the fact that signal from such tracks starts with pulses from the separate clusters, having the small amplitude and the electronics triggering happens with an additional delay. Therefore an essential requirement to the electronics is the minimization of signal "walking" due to an alteration in the signal amplitude.

5.1.3.4 Time measurement.

As it was already told, the straw tubes initially is intended for the time measurement. The start time can be determined with the relatively high precision, for instance by the Time-Of-Flight detector. The stop time has an uncertainty determined by:

1. time of propagation in the straw;
2. discretisation of the time measurement;
3. spread in the discriminator triggering time.

Let's have a closer look on this factors.

1. The straw tube represents a waveguide, where the electric signal propagates with a velocity close to the speed of light in vacuum. In this case the signal from the far end of the straw tube appears in the preamplifier with $1.5\,m/c \simeq 5\,ns$ later, than signal appeared at the near end.

2. If the time discretisation in the data acquisition is τ, than one gets an additional time uncertainty of $\tau/\sqrt{12}$.

3. Spread in the discriminator triggering time unavoidable appears, because arriving signals have different shapes and amplitudes. Except of the primary ionization statistic, shape and amplitude variations are also resulting from the the gas gain fluctuations.

In total the time uncertainty leads to the coordinate measurement error

$$\delta r = v_{drift}\delta t, \tag{5.20}$$

where v_{drift} is velocity in the point where the track passed trough. Both variables v_{drift} and δt have a tendency to decrease with r increasing. Because of that the δt contribution is particularly noticeable on the small distances, strengthen the "cluster-effect". For $v_{drift} < 50\,\mu\mathrm{m}/ns$, the time uncertainty contribution into the resolution is below $50\,\mu$m for the discriminator time jitter less than $1\,ns$. In the "cold" gases that contribution is even fewer due to the smaller drift velocity.

It should be noticed, that there is an effect of the long-distance focusing. An average amount of charge, arriving in the small time interval dt, don't depend on the distance for the distant tracks (see Fig. 5.7):

$$h = 2\sqrt{(r + v(r)dt)^2 - r^2} = \sqrt{8rvdt} \sim \sqrt{dt}. \tag{5.21}$$

For the distant tracks the number of clusters arriving together in the first 5-7 ns of the signal development is independent from r and equal 5. It should be notice, that in the "cold" gas mixtures this effect is stronger than in the "hot" ones.

5.1.3.5 Mechanics accuracy.

Unavoidable source of the systematic errors in the coordinate measurement is uncertainty in the straw positions. The measurement of the drift time gives the relative coordinate, while the displacement of the straw tube itself leads to the shift in the reconstructed absolute coordinate. In the case of the common parallel shift of the whole tube the measurement error don't depend on the position of track crossing point. In that case the absolute shift can be determined from the calibration and therefore corrected. But there are some mechanical imperfections leading to the errors depending on the track angle, the drift distance, the longitudinal coordinate etc. In that case all correction procedures becomes too complicated and ineffective. Because of that it's necessary to increase the mechanical accuracy as much as possible during the detector construction and production.

Necessity to have a right shape the straw tube imposes even more stringent requirements. Deformations of the tube shape can cause irregular distortions along the tube and loss of the spatial resolution, as it have been discussed in the Sec. 4.2.2.1.

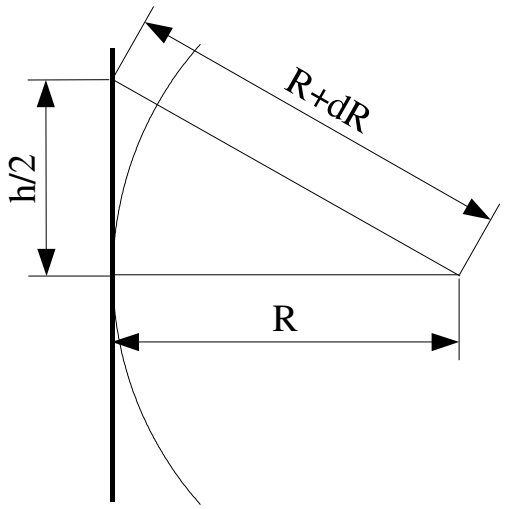

Figure 5.7: Long-distance focusing for the distant tracks.

5.2 Simulation of the straw tube spatial resolution.

Detector parameters in the great degree depend on the composition of the gas mixture. Standard choice for many experiments are "hot" or "warm" gas mixtures (cf. Table 4.4), with a weak dependency of the drift velocity from the applied electric field. In that case electric field inhomogenuity don't play significant role, what makes the calibration simpler. The high pressure can be used for the diffusion reduction. The "cold" gas mixtures has normally only one significant advantage - the high spatial resolution, and many disadvantages, like long drift time, sensitivity to the temperature and pressure variation etc.

The main requirement, which should be taken into account during the choice of the gas mixture, are:

- appropriate spatial resolution;
- rate capability;
- radiation hardness;
- working pressure;
- accessibility on the market and price;
- working voltage;

- chemical inactivity;
- radiation length.

It's very difficult, if possible at all, to satisfy all mentioned above conditions. For the $\overline{\text{P}}$ANDA detector the spatial resolution, rate capability and radiation hardness are questions of the special importance. At the beginning the "cold" gas mixture of $He + 10\% i - C_4H_{10}$ have been chosen as it was written in the Conceptual Design Report [12]. This gas mixture has one undoubted advantage - the large radiation length, but has a long drift time, the disadvantage, which is more or less peculiar for all "cold" gases. Because of that another gas mixture $Ar + 10\% CO_2$ has been suggested.

To compare both mixtures special fast simulation has been developed[2]. Another goal was the development of algorithm for the digitalization of GEANT4 hits (see Sec. **??**). The detailed description of this algorithm and comparison between the two gas mixtures is the subject of this section.

5.2.1 Initial data.

This simulation is based on approximations for the main electron transport processes - the electron drift and diffusion. The ideal straw tube with the cathode diameter of $10\,mm$ and the anode wire diameter of $20\,\mu$m (e.g Fig. **??**) has been used as a model. Only the track with the normal incidence angle from minimum ionizing particles have been simulated (see Fig. 5.8). The leading edge discriminator have been used for the stop signal generation. The time of signal propagation along the straw is not included.

For the correct approximation of the drift time and diffusion, the time-space and diffusion-space curves for the different gas mixtures have been created, using following formulae:

$$t(r) = \int_{r_a}^{r} \frac{dx}{V(E(x))} and \sigma_l(r) = \int_{r_a}^{r} \sigma(E(x))dx, \tag{5.22}$$

where r is the distance to anode wire, r_a is the anode radius, $V(E(x))$ is the drift velocity in depend on the electric field strength in a certain space point, $\sigma_l(r)$ is the longitudinal diffusion for the cluster passing the distance r, $\sigma(E(x))$ is the longitudinal diffusion for the given value of the electric field for the unit length. Thereafter this curves were fitted with polynoms of the 6th degree. Some results, one can see on the Fig. 5.9 and Fig. 5.10. Properties of all tested gas mixtures are listed in Table 5.2. The data for drift velocity and longitudinal diffusion have been taken from [5, 14, 15]. Some other parameter, needed for this simulation can be found in the Table 5.1.

5.2.2 Description of the simulation algorithm

The full simulation process can be divided into two parts: calculation of the minimum time of propagation for the electron clusters from the track at given distance (see Fig. 5.8) and

[2]It should be noted that many Monte-Carlo simulation packages for the detailed simulations of the proportional chambers are exist. One of them is GARFIELD simulation packages [13], developed in CERN.

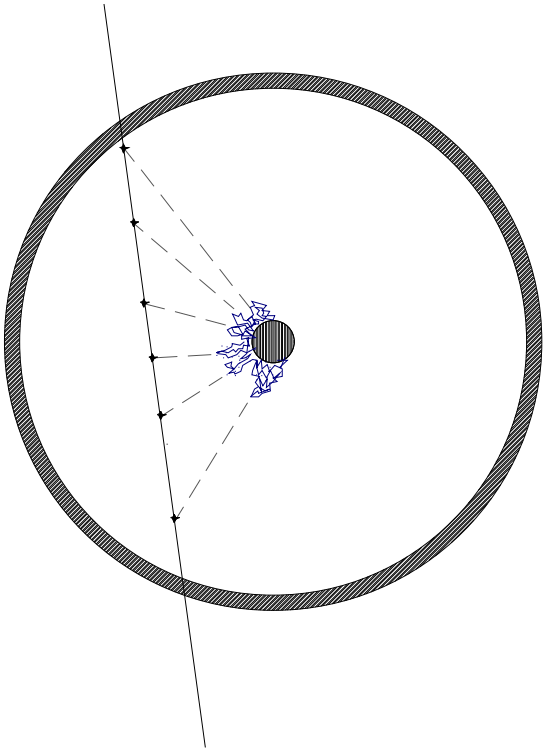

Figure 5.8: Drift of the electron clusters in the straw tube.

Table 5.2: Parameters of the used gas mixtures.

Gas or gas mixture	$\overline{W_i}$[eV]	$\overline{n}_{cl}[cm^{-1}]$	Max. drift time [ns] for 5mm. drift	$\overline{V}_{drift}$[cm/μ]	X_0[m]
$Ar + 10\%CO_2$ (1atm.)	26.7	24.6	100	5.36	117
$Ar + 10\%CO_2$ (2atm.)	26.7	49.2	110	4.84	58.5
$He + 10\%i{-}C_4H_{10}$ (1atm.)	39.2	12.7	215	2.48	1313
$He + 10\%i{-}C_4H_{10}$ (2atm.)	39.2	25.4	280	1.97	656.5
$He + 20\%i{-}C_4H_{10}$ (1atm.)	37.4	20.6	175	2.9	749

then reconstruction of the distance to the incoming track using that time. The standard deviation of the distribution of the difference between given and reconstructed distance is the *spatial resolution* at this point.

It's naturally to separate the distance-to-time calculation into the subroutine, which later can be use as the stand alone procedure for Geant4 hits conversion.

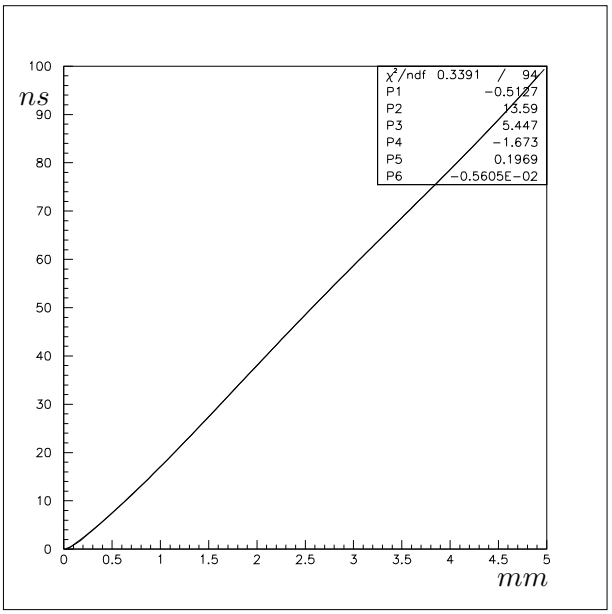

Figure 5.9: The dependency curve for the drift time from the distance in $Ar + 10\%CO_2$ gas mixture at STP.

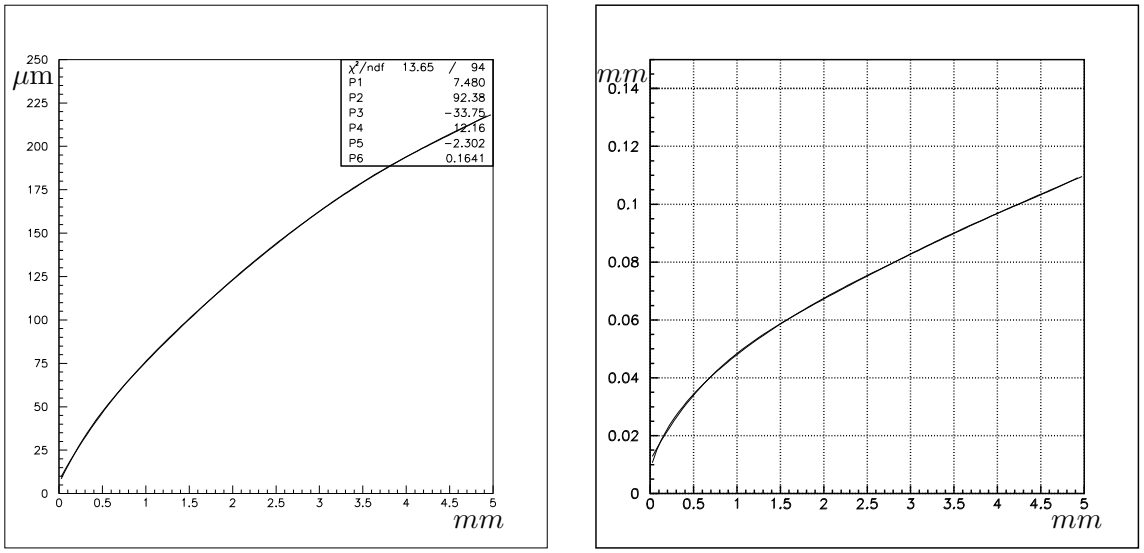

(a) diffusion in the $Ar + 10\%CO_2$ gas mixture (b) diffusion in the $He + 10\%i{-}C_4H_{10}$ gas mixture

Figure 5.10: The dependency curve for the diffusion from the in $Ar + 10\%CO_2$ (a) and $He + 10\%i{-}C_4H_{10}$ (b) gas mixtures at STP.

5.2.2.1 Distance-to-time conversion.

The algorithm of conversion of the given distance into the drift time can be split in the following steps:

- calculation of the length of the track inside the straw tube, assuming a normal angle of incidence;
- seeding clusters of the primary ionization along the track for the given gas mixture and the pressure, in accordance with *Poisson* distribution (e.g. Fig. 5.11). Some useful parameters are listed in the Table 5.2;
- calculation the number of electrons in an each cluster, as it was described in Sec. 5.1.1

  $$N(E \geq E_0) \simeq \frac{W}{E_0},$$

  where

  $$W = \frac{154 Z \rho}{A} [keV/cm]$$

  is the characteristic energy for the given gas mixture, Z, A and ρ are the its average charge, the its average atomic number and its density, correspondingly. Typical distributions for $Ar + 10\% CO_2$ and $He + 10\% i{-}C_4H_{10}$ gas mixtures one can see on see Fig. 5.12;
- calculation the charge of the avalanche for each cluster. The each electron, arriving to the anode, produce the avalanche with amplitude distributed exponentially(see equation 5.16) around the mean value, which is the average gas gain, defined arbitrary. The total charge is a sum of charges of all individual avalanches, as it shown on Fig. 5.13. The histogram on this figure has the two region with different slopes: the one in the region of smaller avalanche sizes corresponds the case of the single electron clusters, those, in the region of the bigger avalanche sizes, corresponds the case of the multi-electrons clusters. The cutoff on the avalanche size have been introduced to imitate of a limitation due to space charge effect(see Sec. 5.1.2).
- the drift distance modification for each cluster due to the longitudinal diffusion (e.g. Fig. 5.10).
- the drift time calculation for each cluster (e.g. Fig. 5.9);
- computation of the stop time, including the "walking" effect (see Sec. 5.1.3.4). The signal from the each cluster is simulated. Typical shape of signal is shown on the Fig. 5.15. Here the avalanche size is assumed to be equal the average value. For the signal with the avalanche size differ from average, the signal amplitude is scaled accordingly. After that the periodic and the random noises are added to the signal, in order to make the signal more realistic. The typical signal shapes with and without noises are shown (cf. Fig. 5.14). The periodic noise is clearly seen on the Fig. 5.15 (a), where the signal for the distant track are shown. Threshold of discriminator is set to $0.6\, a.u.$ on all figures.

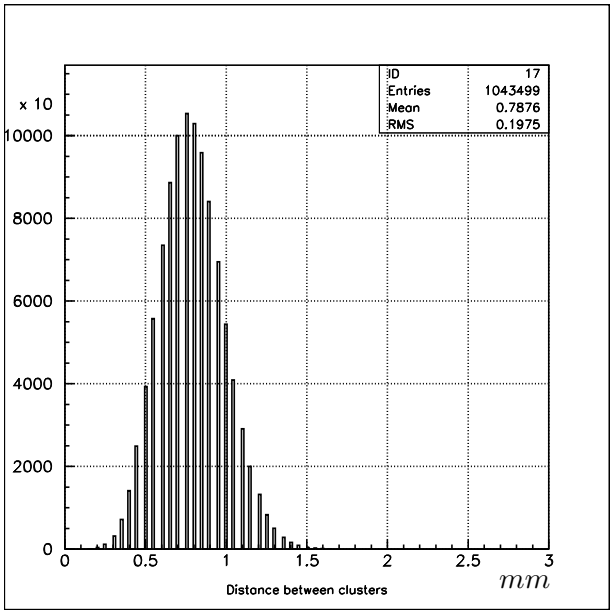

Figure 5.11: Distance between the clusters in $He + 10\%i{-}C_4H_{10}$ gas mixture at STP.

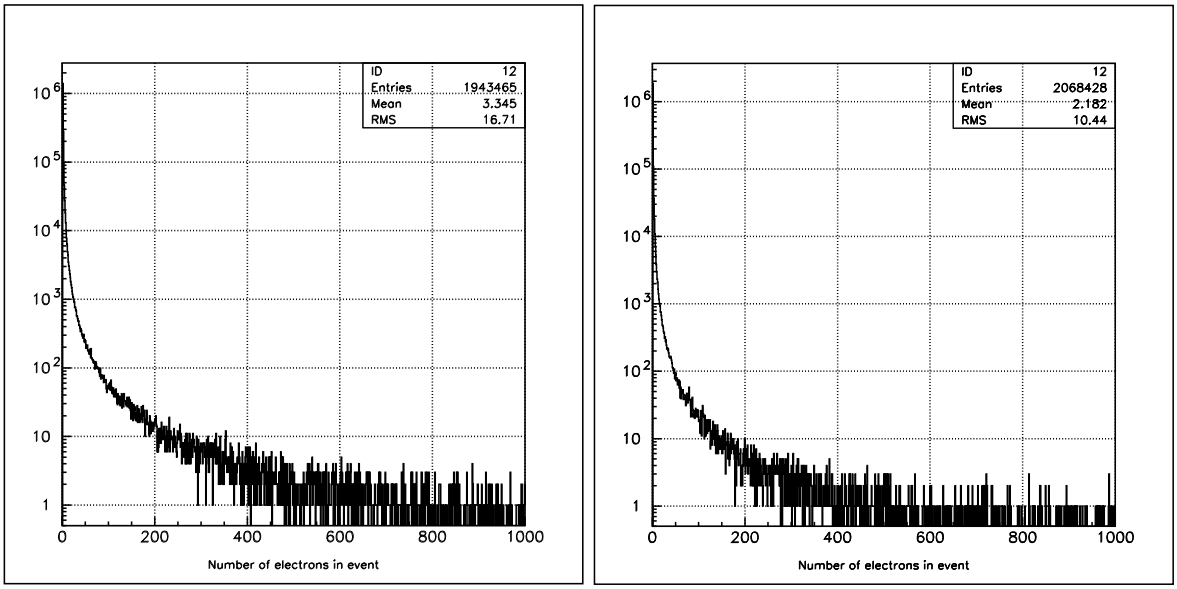

(a) number electrons in cluster in the $Ar{+}10\%CO_2$ gas mixture

(b) number electrons in cluster in the $He + 10\%i{-}C_4H_{10}$ gas mixture

Figure 5.12: The number electrons in cluster in $Ar + 10\%CO_2$ (a) and $He + 10\%i{-}C_4H_{10}$ (b) gas mixtures at STP.

The signal shape has been parametrized by equation

$$V(t) = Ae^{B\ln(t)-Ct}(1 + Dt + Et^2), \tag{5.23}$$

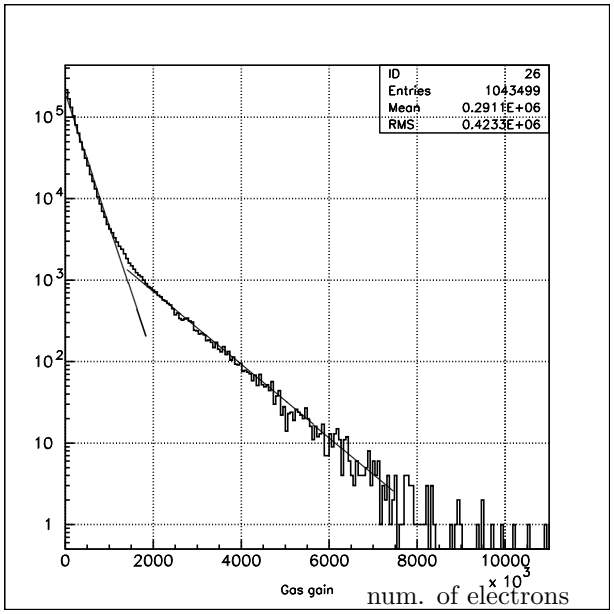

Figure 5.13: Avalanche size (number of electrons) distribution.

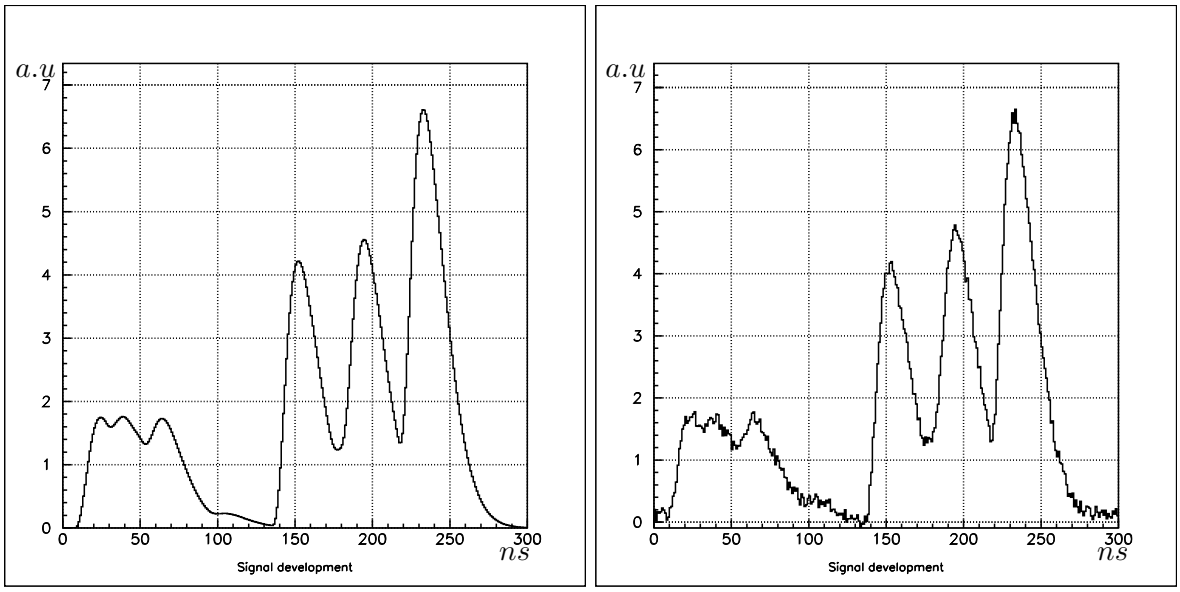

(a) signal development in the $He + 10\%i-C_4H_{10}$ gas mixture

(b) signal development in the $He + 10\%i-C_4H_{10}$ gas mixture

Figure 5.14: The signal development from the track crossed anode wire in the He+10%i–C_4H_{10} gas mixture are shown in two cases with (a) and without (b) noises.

where parameters equal $A = 1.03 \cdot 10^{-3}$, $B = 3.95$, $C = 0.228$, $D = -3.839 \cdot 10^{-2}$ and $E = 1.148 \cdot 10^{-3}$.

The "cluster-effect" can be clearly seen on the Fig. 5.14. Although track crosses the anode wire, the arrival time of the first cluster, which theoretically should be equals to zero, is about of $15\,ns$.

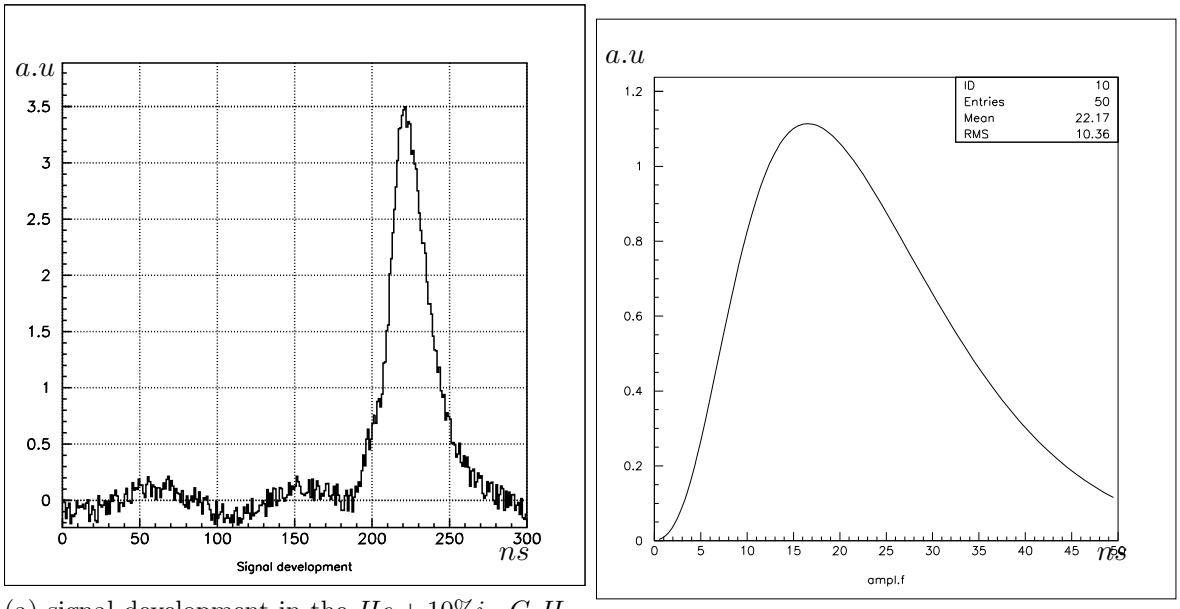

(a) signal development in the $He + 10\%i - C_4H_{10}$ gas mixture

(b) typical signal shape from single electron cluster

Figure 5.15: The signal development for the track of $4\,mm$ away from the anode wire in the $He + 10\%i - C_4H_{10}$ gas mixture is shown on figure (a). Figure (b) shows the typical signal from the signal electron cluster.

5.2.2.2 Distance reconstruction and resolution calculation.

Concept of the *spatial resolution* was defined in the previous section 5.2.2. To calculate it one needs compare the true coordinate of the track with reconstructed one. For such reconstruction one has to know $r(t)$ dependence for the given straw geometry, filled with the specific gas mixture. Usually such dependency can be obtained either from Monte-Carlo simulation or from so-called "self-calibration" procedure. The both methods are described below.

Reconstruction using "computed" or "ideal" drift curve. The same drift curve, as for the distance-to-time conversion, is used in this case (e.g. Fig. 5.9). The drift time is converted into the drift distance according to this curve. Of course the drift distance reconstructed in such way will have big systematic shift, because the scattering processes did not taken into account. That can be seen on the Fig. 5.16 (a), where the black histogram represents uncorrected spatial resolution. In the real experiments, such systematic errors can be corrected using the iterative procedure, when the track roughly reconstructed using the raw uncorrected drift curve. The coarse systematic errors, obtained from deviation of the hits positions from the track, can be used for correction

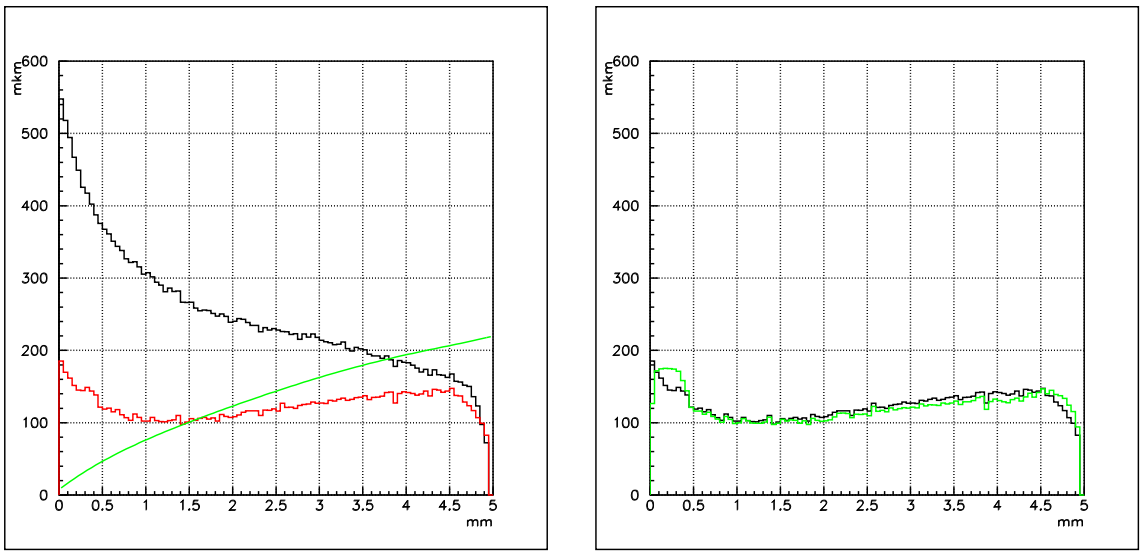

(a) straw resolution before and after systematic errors correction

(b) straw resolution before and after systematic errors correction

Figure 5.16: Comparison of resolutions before and after correction of the systematic shift. The "ideal" drift curve have been used for reconstruction in case (a) and "self-calibrated" in case (b). The green line on the figure (a) represents diffusion limit. See text for more details.

of the drift curve, whereat the whole procedure is repeated again. Such process reiterates unless the needed accuracy will be achieved.

In our case the true track position have been used for the systematic errors minimization. The results after minimization can be seen on the same Fig. 5.16 (a), but denoted by the red color. The resolution, one can get in such a way, will be without doubt better than one can get in the real case. Because of that this results have been used only for comparison between two reconstruction methods.

Reconstruction using "self-calibrated" drift curve. The "self-calibration" method is based on the assumption that the track density is constant over the tube radius. Hence one can writes

$$\frac{dN}{dR} = \frac{N_{tot}}{R_0}, \tag{5.24}$$

where N_{tot} is the total number of tracks, R_0 is the tube radius. Assumed, that efficiency doesn't depend on tube radius, one will obtained

$$\frac{dN}{dt} = \frac{dN}{dR}\frac{dR}{dt} = v_{drift}(t)\frac{N_{tot}}{R_0}. \tag{5.25}$$

After an integration a simple expression is resulting for $r(t)$:

$$r(t) = R_0\frac{N(t_1 < t)}{N_{tot}}, \tag{5.26}$$

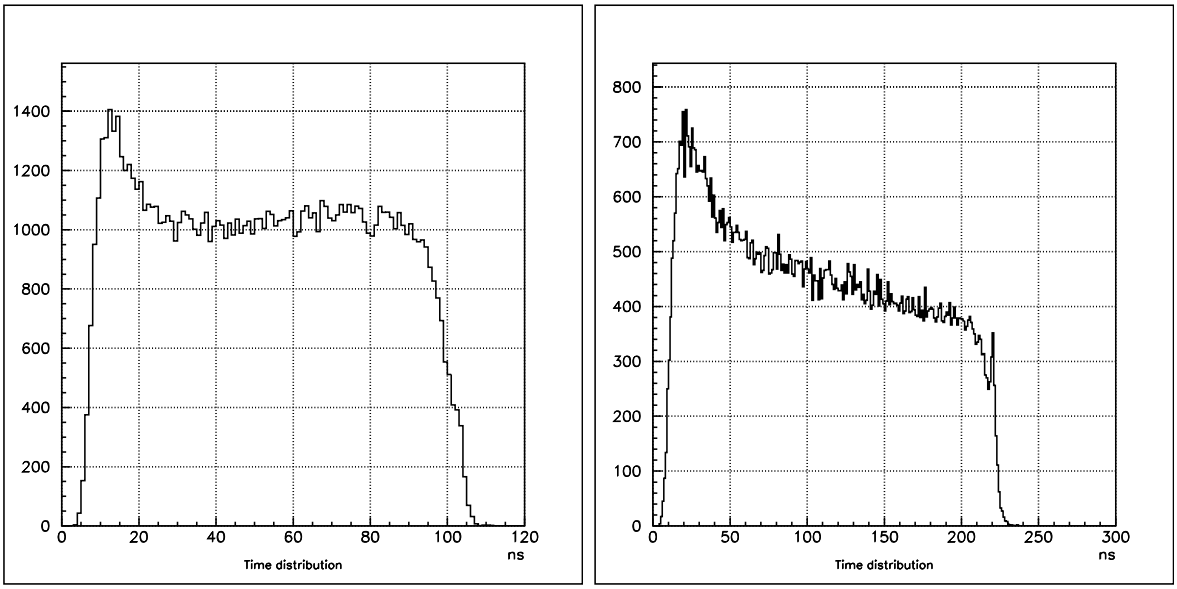

(a) time spectrum for the $Ar + 10\%CO_2$ gas mixture

(b) time spectrum for the $He + 10\%i-C_4H_{10}$ gas mixture

Figure 5.17: Time spectra for the $Ar + 10\%CO_2$ and $He + 10\%i-C_4H_{10}$ gas mixtures at STP.

where $N(t_1 < t)$ is a fraction of all track, arrived to the time moment t. Such drift curve can be easily obtained by an integration of the time spectrum arriving signals. Examples of such spectra are shown on the Fig. 5.17. The spatial resolution of this method is quite good even without the systematic error correction, what is shown on the Fig. 5.16 (b), where the uncorrected curve is shown by the black color and corrected one is shown in red. As one can see there are no improvements in this case.

Examples of the drift curves are shown on Fig. 5.18.

5.2.3 Interpretation of simulation results.

On Fig. 5.19 and Fig. 5.20 the spatial resolutions for the $Ar + 10\%CO_2$ and $He + 10\%i-C_4H_{10}$ are shown for the 1 and 2 atm gas pressures. The good coincidence of the simulation data with the results from KLOE drift chamber prototype, as shown on the Fig. 5.20, can be interpreted as the proof of an applicability of this algorithm for the simulation of the straw tube parameters.

The spatial resolution of the $Ar + 10\%CO_2$ mixture is satisfactory even at $1\,atm$ pressure, while the spatial resolution in the $He + 10\%i - C_4H_{10}$ is worser than required $150\,\mu$m (see Sec. 4.2.1) and only the pressure growth can improve this situation (cf. (a) and (b) on the Fig. 5.20).

The total drift time is also an important parameter. From the $r(t)$ dependency curves for this gas mixtures, shown on Fig. 5.18, it can be seen that $Ar + 10\%CO_2$ is typical "hot" gas mixtures, while in $He + 10\%i-C_4H_{10}$ drift velocity is not saturated and this mixture can be classified as "cool". The $Ar + 10\%CO_2$ has the drift time of $80\,ns$ for

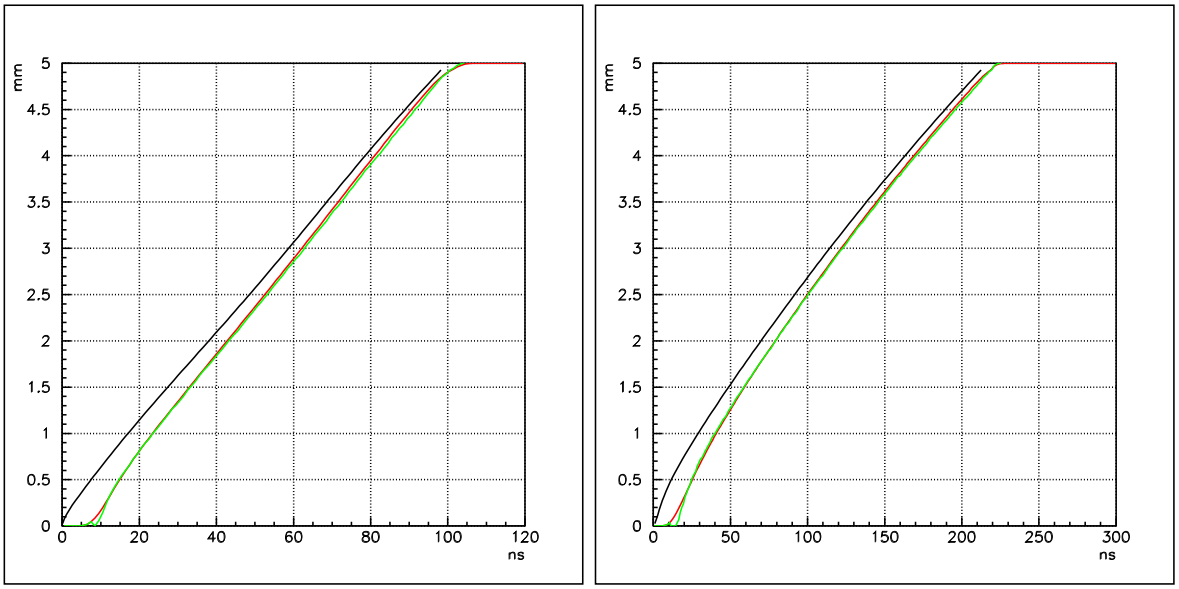

(a) the drift curve for the $Ar + 10\%CO_2$ gas mixture

(b) the drift curve for the $He + 10\%i{-}C_4H_{10}$ gas mixture

Figure 5.18: The drift curves for the $Ar + 10\%CO_2$ and $He + 10\%i{-}C_4H_{10}$ gas mixtures at STP. The black one corresponds the "ideal" drift curve, the "red" and "green" ones correspond the "self-calibrated" drift curve before and after systematic errors correction correction.

the $4\,mm$ drift path. The $He + 10\%i{-}C_4H_{10}$ has the drift time in two times larger. The average time between two events in $\overline{\text{P}}$ANDA will be $\sim 100\,ns$. It means that by usage of the $He + 10\%i{-}C_4H_{10}$ gas mixture, the information about two consequential event will be contained in the STT in any time moment. In own turn the event mixing in tracker means significant complication in the trigger logic and the pattern recognition algorithm. With the pressure increasing in two times the drift time for the $He + 10\%i{-}C_4H_{10}$ grows on $50\,ns$, while for the $Ar + 10\%CO_2$ only on $10\,ns$. That makes the situation with the event mixing even more difficult.

The behavior of the spatial resolution by the electronics threshold rise has also been studied. The average gas gain have been reduced in two times at the same electronic threshold. The Fig. 5.22 shows only the small deterioration of the $Ar{+}10\%CO_2$ resolution and strong worsening in the case of the $He{+}10\%i{-}C_4H_{10}$ gas mixture, which is one more argument in the favor of the $Ar + 10\%CO_2$ usage.

All this considerations shows the strong advantage of the $Ar + 10\%CO_2$ gas mixture as a gas filling for the $\overline{\text{P}}$ANDA STT compared with $He{+}10\%i{-}C_4H_{10}$ gas composite. Parameters of the $Ar{+}CO_2$ gas mixture can be modified in the future, by changing pressure, CO_2 percentage or admixture other gases, in accordance with the STT occupancy simulation results.

The behavior of the spatial resolution by the electronics threshold rise has also been studied. The average gas gain have been reduced in two times at the same electronic threshold. The Fig. 5.22 shows only the small deterioration of the $Ar{+}10\%CO_2$ resolution and strong worsening in the case of the $He{+}10\%i{-}C_4H_{10}$ gas mixture, which is one more

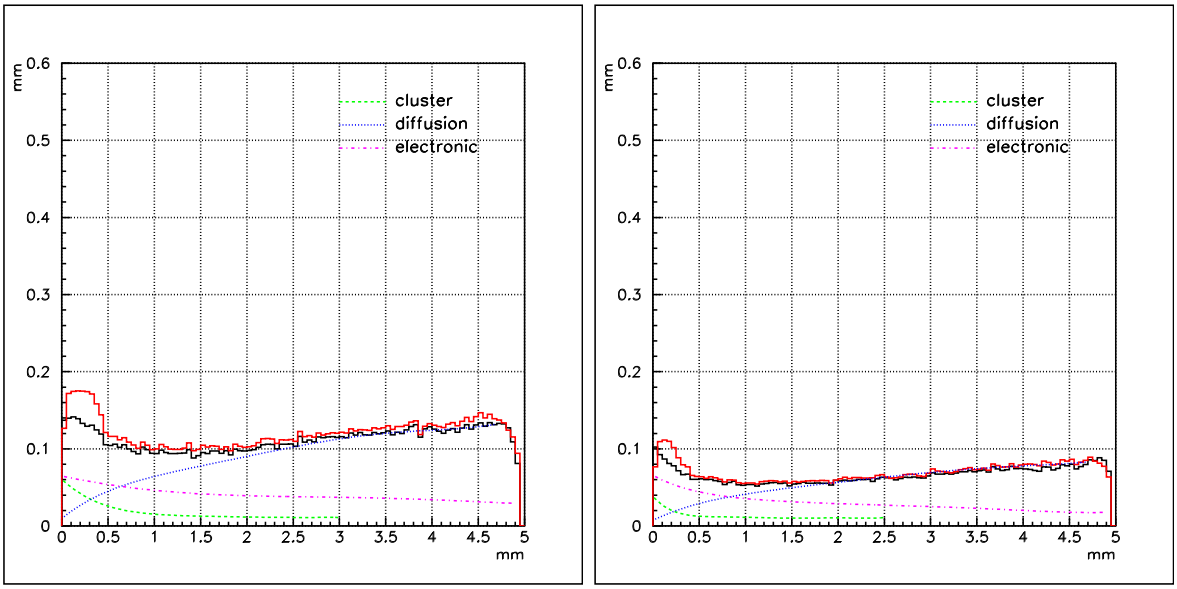

(a) Spatial resolution for the $Ar + 10\%CO_2$ gas mixture for 1 atm

(b) Spatial resolution for the $Ar + 10\%CO_2$ gas mixture for 2 atm

Figure 5.19: The spatial resolution for the $Ar+10\%CO_2$ gas mixture for 1 and 2 atm pressures. The red line corresponds the case, when "ideal" drift curve have been used, the black one corresponds the "self-calibration" procedure. Contributions from the main limiting process are shown dashed lines of different colors.

argument in the favor of the $Ar + 10\%CO_2$ usage.

All this considerations shows the strong advantage of the $Ar + 10\%CO_2$ gas mixture as a gas filling for the $\overline{\text{P}}$ANDA STT compared with $He + 10\%i{-}C_4H_{10}$ gas composite. Parameters of the $Ar + CO_2$ gas mixture can be modified in the future, by changing pressure, CO_2 percentage or admixture other gases, in accordance with the STT occupancy simulation results. Usage of tubes with increased diameter follows from the spatial resolution behavior depend on the drift distance, it makes use of tubes with diameters of $8\,mm$ or even $10\,mm$ favorable.

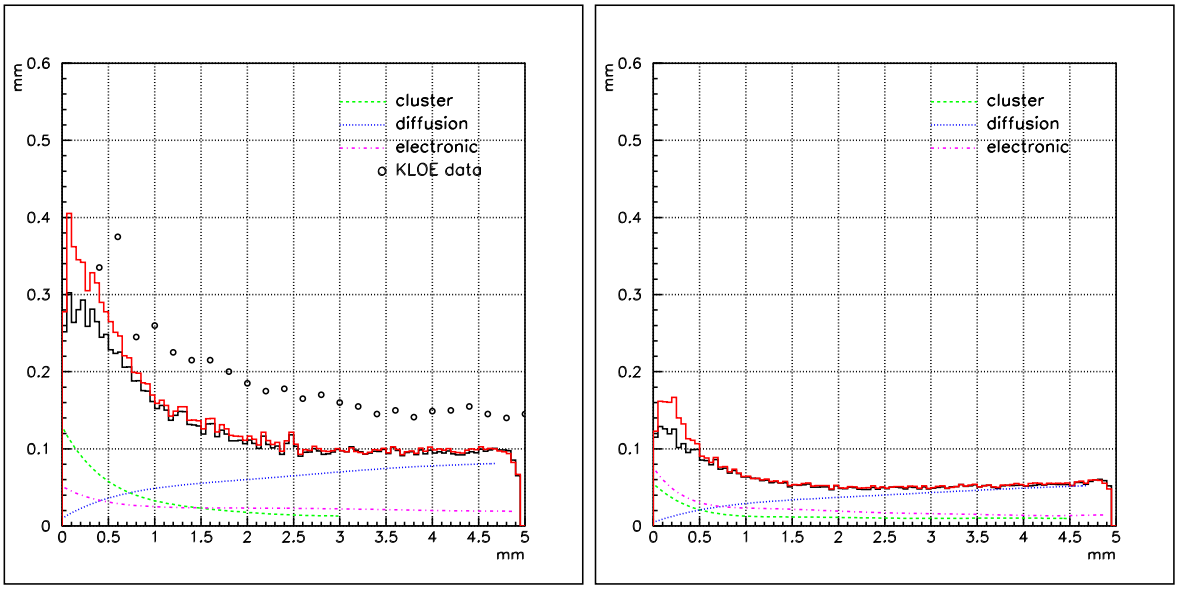

(a) Spatial resolution for the $He + 10\%i - C_4H_{10}$ gas mixture for 1 atm

(b) Spatial resolution for the $He + 10\%i - C_4H_{10}$ gas mixture for 2 atm

Figure 5.20: The spatial resolution for the $He + 10\%i - C_4H_{10}$ gas mixture for 1 and 2 atm pressures. The red line corresponds the case, when "ideal" drift curve have been used, the black one corresponds the "self-calibration" procedure. Contributions from the main limiting process are shown dashed lines of different colors. The spatial resolution of the KLOE drift chamber, denoted by the black circles, is given for comparison.

5.3 Charge division and time difference technique.

Although the straw tube is designed for the drift time measurement for the minimum particle track distance reconstruction, it's possible also to get the track coordinate along the wire. There are different methods to reconstruct the track coordinate (z) along the wire. One option to obtain the z-coordinate is use of the charge division technique [16]. This method uses two-point charge splitting to identify the position of an ionizing event along the tube (see Fig. 5.23).

Another possibility of z-coordinate measurement is the time-difference technique. The time difference between the pulses arriving at the opposite ends of the tube is measured to determine the track position along the tube.

5.3.1 Charge division.

In this case, two amplifiers at the two ends of a straw, are needed. Each preamplifier receives a fraction of the total charge. The relative position x of the event along the straw can be calculated as:

$$x = l\frac{Q_r}{Q_r + Q_l}$$

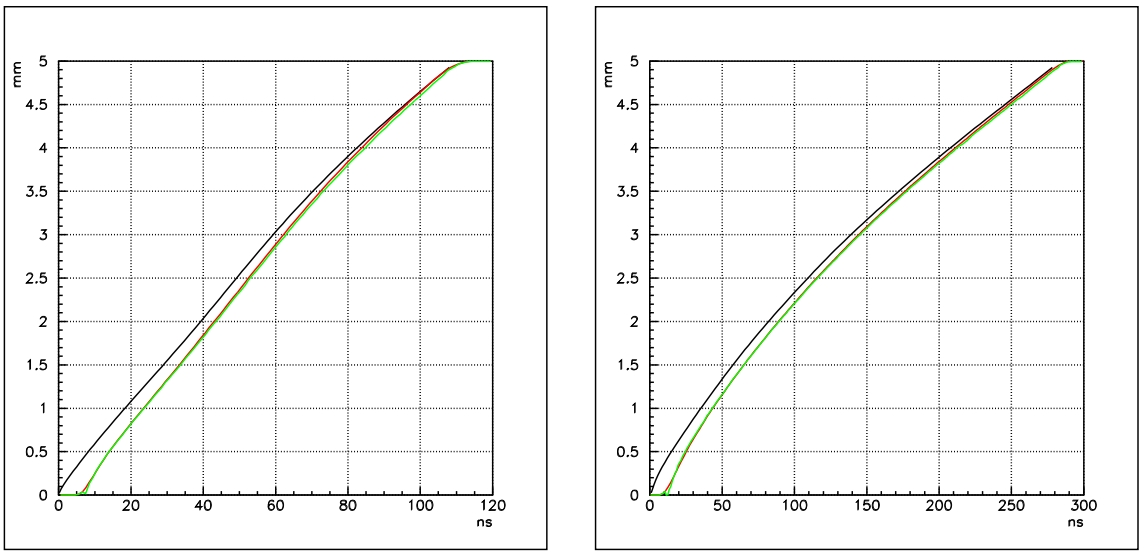

(a) the drift curve for the $Ar + 10\%CO_2$ gas mixture

(b) the drift curve for the $He + 10\%i-C_4H_{10}$ gas mixture

Figure 5.21: The drift curves for the $Ar + 10\%CO_2$ and $He + 10\%i-C_4H_{10}$ gas mixtures at $2\,atm$. The black one corresponds the "ideal" drift curve, the "red" and "green" ones correspond the "self-calibrated" drift curve before and after systematic errors correction correction.

where l is the total length of the straw, Q_r is the charge collected at the right end and Q_l is the charge collected at the left end of the straw. The spatial resolution of the proportional chamber achievable with this method is typically 0.5-1% of the sensitive wire length [17]. For the $\overline{\text{P}}$ANDA STT one can expect a spatial resolution of 7–15 mm at the tube center. The spatial resolution at the ends deteriorates up to two times, due to a loss of linearity [18]. This is about 3–4 times worser than can be achieved using the geometry with skewed tubes(see Sec. 4.2.3). Another disadvantages of this scheme is it requires twice the number of electronics channels which need to register the amplitude of the signal.

Nevertheless, the charge division method has advantages. First of all, it can provide the fast information about the track position which is very important for the online triggering. Secondly, the simpler detector geometry makes it possible to avoid a heavy mechanical frame. Finally, the number of electronics channels can be reduced by connecting the straws in pairs and by reading them only at one end albeit that this will worsen the spatial resolution by a factor of two.

A final decision on the method to be used will be taken after further R&D. Studies of the applicability of the charge division method are under way at Jülich FZ Chap. **??**.

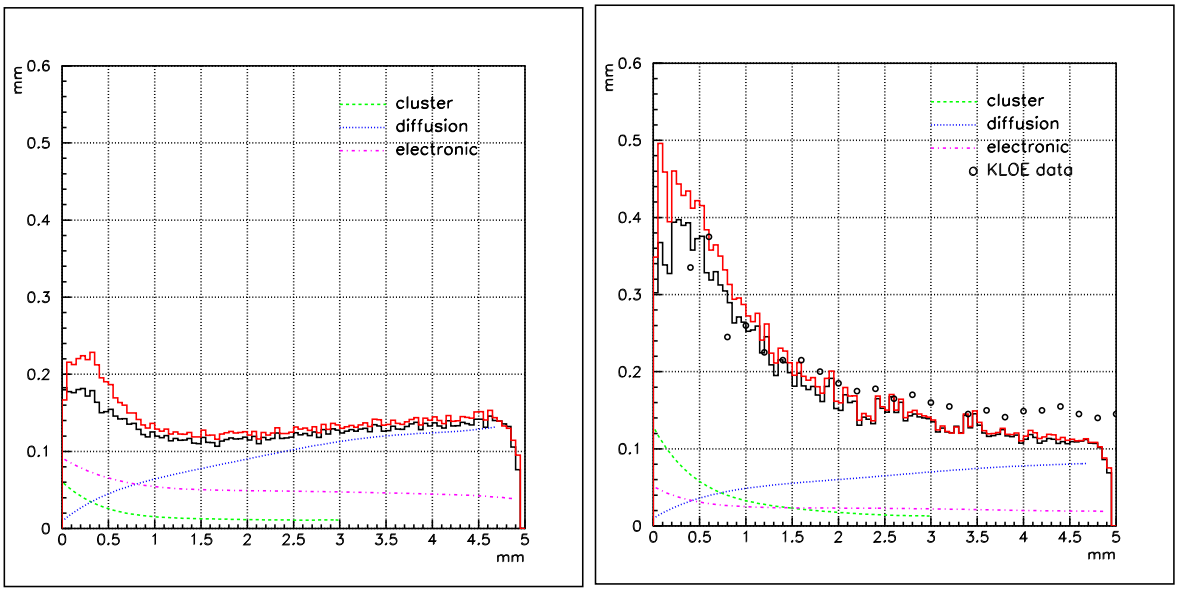

(a) Spatial resolution for the $Ar + 10\%CO_2$ gas mixture for 1 atm

(b) Spatial resolution for the $He + 10\%i-C_4H_{10}$ gas mixture for 1 atm

Figure 5.22: The spatial resolution for the $Ar + 10\%CO_2$ and $He + 10\%i-C_4H_{10}$ gas mixture for 1 atm pressures. The gas gain have been reduced in two times compared with Fig. 5.19. The red line corresponds the case, when "ideal" drift curve have been used, the black one corresponds the "self-calibration" procedure. Contributions from the main limiting process are shown dashed lines of different colors. The spatial resolution of the KLOE drift chamber, denoted by the black circles, is given for comparison.

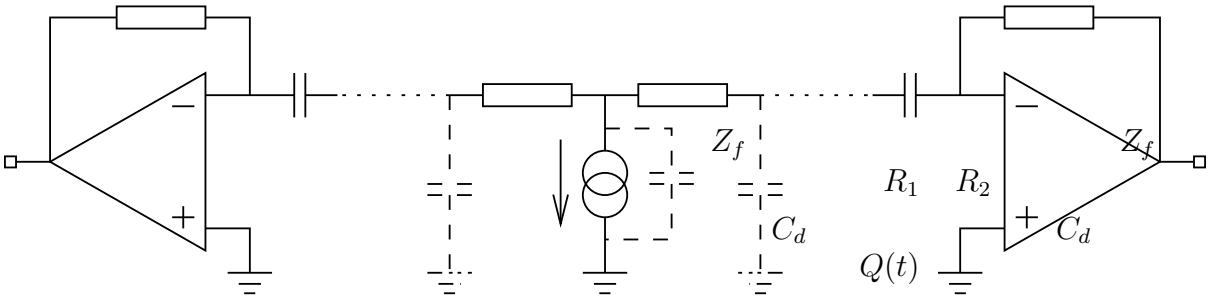

Figure 5.23: A scheme of a straw tube with charge amplifiers at both ends. The resistances R_1 and R_2 are proportional to the distances to both ends of the anode wire. C_d are decoupling capacitances. The current signal delivered by the detector is $Q(t)$. Impedances Z_f terminate the straw tube at both ends relative to the virtual ground through decoupling capacitors.

5.3.2 Time difference.

The z-coordinate is proportional to the obtained time difference with coefficient $v/2$, where v is the pulse propagation velocity in a tube. Since v is approximately equal to the speed of light in vacuum, the conversion coefficient t/z is equal to $6.7\,ps/mm$. It means that the time resolution of $\sim 70\,ps$ is needed to be competitive with the charge division technique. However compared to the charge division, timing has following advantages:

- only one digital converter required instead of two;
- an anode wire can have a smaller resistance, therefore higher rate capability can be achieved;
- the utmost attainable resolution for the time-difference technique is considerably better than for the charge division [18], but it should be noticed that such high resolution have been achieved for the streamer mode operation.

An additional investigations are needed to decide if that method can be used in the $\overline{\text{P}}$ANDA STT.

Also the time information can be used to increase the charge asymmetry for charge division technique as it shown in the Chap. **??**.

References

[1] C. Damerell, RAL **077** (1986).

[2] F. Sauli, Principles of operation of multiwire proportional and drift chambers, CERN 77-09, 1977.

[3] E. Kobetich and R. Katz, Phys. Rev. **170/2**, 391 (1968).

[4] F. Lapique and F. Piuz, NIM **175**, 297 (1980).

[5] F. Sauli and A. Peisert, CERN 84-08, 1984.

[6] V. Palladino and B. Sadoulet, NIM **128**, 323 (1975).

[7] S. Biagi, http://rjd.home.cern.ch/rjd/cgi-bin/cross.

[8] G. S. A. Breskin et al., NIM **124**, 189 (1975).

[9] A. R. P. Cwetanski and V.Sosnovtsev, Studies of wire offset effect on gas gain in the ATLAS TRT straw chamber, ATLAS Internal Note ATL-INDET-, 2000, 016.

[10] G. Alkhazov, NIM **89**, 155 (1970).

[11] J. Va'vra, SLAC-PUB-3727.

[12] Conceptual Desighn Report, http://www-new.gsi.de/GSI-Future/cdr/, Technical report, FAIR/GSI, 2002.

[13] R. Veenhof, GARFIELD, Simulation of gaseous detectors, Version 8.01, CERN Program Library Writeup W5050, CERN, Geneva, Switzerland, 2005.

[14] G. Sharma and F. Sauli, NIM **350**, 470 (1994).

[15] P. Colas et al., NIM **478**, 215 (2002).

[16] A. Pullia et al., IEEE Trans. Nucl. Sci. **49**, 3269 (2002).

[17] D. Chernyak et al., Nucl. Instrum. Meth. **A419**, 370 (1998).

[18] S. Biagi and P. Booth, Nucl. Instrum. Meth. **A252**, 586 (1986).